UNIVERSITÀ DEGLI STUDI DI PADOVA

UNIVERSITA' DEGLI STUDI DI PADOVA

INSTITUTO SUPERIOR TECNICO-UNIVERSIDADE TECNICA DE LISBOA

Centro Interdipartimentale *"Centro Ricerche Fusione"* Università di Padova

JOINT RESEARCH DOCTORATE IN FUSION SCIENCE AND ENGINEERING

IMPROVED FEEDBACK CONTROL OF MHD INSTABILITIES AND ERROR FIELDS IN REVERSED-FIELD PINCH AND TOKAMAK

Coordinator: Chiar.mo Prof. Piero Martin

Supervisor: Chiar.mo Prof. Piero Martin

Tutors: Dr. Lionello Marrelli

Dr. Paolo Piovesan

Doctoral Student: Lidia Piron

Padova, 31 Gennaio 2011

All's Well That Ends Well

By William Shakespeare

Abstract

This Thesis presents a series of results on the development of advanced magnetic feedback schemes for the active control of magnetohydrodynamic (MHD) instabilities and error fields obtained in two magnetically confined toroidal experiments: the RFX-mod reversed-field pinch (RFP) in Padova, Italy, and the DIII-D tokamak at General Atomics, San Diego, CA, USA.

In the last years, these two devices have explored different types of high-performance regimes, also thanks to their sophisticated active control systems. In RFX-mod, high-plasma current experiments, up to $2MA$, were performed for the first time in a RFP. These experiments allowed for the discovery of a new self-organized helical equilibrium with good confinement properties [40]. Instead, in DIII-D, steady-state, high-performance tokamak operations are being explored. The scientific programs of these experiments, in particular on error field and MHD mode control, can give precious contributions to the International Thermonuclear Experimental Reactor (ITER) and to magnetic fusion research in general.

The RFP and the tokamak are toroidal devices for the magnetic confinement of thermonuclear plasmas. An introduction to thermonuclear fusion, the main requests to exploit fusion as a future energy source, the magnetic confinement of the plasma, and the MHD model which describes the plasma behavior in many cases of interest will be given in *Chapter 1*. The role of magnetic feedback control for the development of advanced operational regimes in RFX-mod and in DIII-D will be also discussed in this Chapter.

Chapter 2 describes the two experiments above mentioned and their magnetic feedback control systems. They are in fact equipped with very flexible systems devoted to the control of MHD instabilities and error fields. In particular the feedback control strategies that are crucial for the work discussed in this Thesis will be presented.

The first important result of this Thesis is reported in *Chapter 3* and regards the optimization of multi-mode control of tearing instabilities in RFX-mod. Tearing modes, which sustain the reversed-field configuration typical of RFP experiments through a dynamo mechanism, can not be completely suppressed by magnetic feedback control. Nonetheless, it is important to reduce their edge radial magnetic field amplitude to the lowest possible value, since it produces a deformation of the last closed flux surface, enhancing the plasma-wall interaction. In this

work, the control of tearing modes has been optimized by using a non-linear model of the tearing mode dynamics in presence of the multiple-shell layout of RFX-mod and of the magnetic feedback system. This model of tearing modes has been implemented in a code named RFXlocking and previously described in [84]. Given the good match between the model predictions and the experimental mode behavior, the RFXlocking code has been used as a tool to identify a new set of mode control parameters (i.e. feedback gains), which allow to reduce the radial magnetic field of multiple tearing modes at the plasma edge, maintaing at the same time the modes into rotation and avoiding coil current saturations. The optimization approach consisted in simulating the mode dynamics varying the feedback gains and identifying the gain set, which fulfills the requirements above described. Once the "model-based" gain set was identified, an extensive experimental campaign was performed on RFX-mod, obtaining satisfactory results in terms of edge radial magnetic field reduction and also confirming the code predictions.

The magnetic feedback optimization performed during this Thesis work concerned not only tearing modes, but also the main magnetic field errors present in RFX-mod. The presence of poloidal gaps in the RFX-mod wall modifies the pattern of eddy-currents induced in it by the vertical magnetic field during the plasma current ramp-up, thus forming toroidally-localized error fields to which tearing modes are phase-locked. Two advanced feedback control strategies have been applied to correct these error fields: a multi-mode control scheme and a dynamic decoupling scheme.

Regarding the first feedback control strategy, a Simulink model of the RFX-mod magnetic feedback system has been used to identify the feedback gains, which allow a significant reduction of the error field amplitude, avoiding coil current saturations. A dynamic decoupler has also been used to compute offline the feedback currents needed to cancel the error fields. As will be described in *Chapter 4*, these two techniques have been tested during a dedicated experimental campaign. The best result in terms of error field reduction has been obtained when both multi-mode control and the decoupler are used. With error field correction during the plasma current ramp-up, the phase-locking among tearing modes is no more localized near the poloidal gaps of the wall, thus reducing the plasma-wall interaction at these positions.

As mentioned above, the high-current RFX-mod experiments have disclosed a promising physics regime, where the RFP spontaneously evolves towards an Ohmic helical equilibrium. This new magnetic equilibrium is characterized by a single helical magnetic axis and helical magnetic surfaces in the plasma core. This leads to a significant decrease in the stochastic transport and to the formation of core electron temperature barriers. During the last experimental campaign, it has been demonstrated that a $(1, -7)$ helical equilibrium can be sustained and controlled by applying helical boundary conditions at the plasma edge through magnetic feedback.

In this Thesis work, *Chapter 5* and *Chapter 6* deal with the optimization of the helical boundary conditions used to control the helical equilibrium. The optimization procedure uses control strategies analogous to those described above and adopted to improve the control of tearing modes and error fields. The RFXlocking code has been modified by adding the possibility to apply a helical boundary conditions. In this way, the mode dynamics has been simulated with this new helical boundary, by varying the feedback gains and the amplitude and phase of the helical magnetic field perturbations imposed at the plasma edge. A model-based optimization approach similar to the one described in *Chapter 3* has been adopted here to identify the feedback gains that allow to produce the requested radial field pattern at the edge with the lowest possible coil current. A partial gain scan has been performed in the experiment and the results confirm the model predictions. The main outcomes of the model-based optimization and an analysis of the effects on the plasma performance of the applied helical boundary conditions are described in *Chapter 5*.

Vacuum field analyses described in *Chapter 6* reveal that, when rotating magnetic field perturbations are applied through magnetic feedback, as in the case of the helical equilibria above described, error fields are induced by the frequency response of the wall to external magnetic fields varying in time. These error fields, that are mainly introduced by the presence of the toroidal and poloidal gaps in the wall structure, may somehow affect the good confinement properties of the helical equilibrium. For this reason, a dynamic decoupler similar to the one used to correct the error fields in the current ramp-up phase of the plasma discharges has been applied. Encouraging results in terms of error field reduction are obtained.

The frequency-response of the wall to any external time-varying magnetic field has been investigated also in the DIII-D tokamak, in the framework of a collaboration between the RFX-mod and DIII-D teams. In the DIII-D control algorithm, the magnetic feedback measurements are usually real-time compensated for spurious magnetic fields, due for instance to the feedback and axi-symmentric coils. These contributions are calculated from the zero-frequency coupling coefficients between each actuator and sensor. In this way the effects of eddy-currents induced in the wall are neglected. The relevance of these frequency-dependent, or AC effects, on RWM and error field control has been evaluated by analyzing past experiments. The analyses suggested that, if the wall frequency response is not taken into account in the feedback compensation scheme, error fields can be introduced when doing magnetic feedback. These can be important especially at high-β, where uncorrected error fields can be strongly amplified by the plasma. An AC compensation algorithm has been implemented and tested in real-time in dry-shots and Ohmic plasmas. More tests of this algorithm at high-β have been proposed for the next experimental campaign to assess its relevance on plasma performance in scenarios where the plasma is less resilient to error fields. The main outcomes of this Thesis work is reported in *Chapter 7*.

Chapter 8 summarizes the main conclusions of this work and describes a series of experiments that could be made both in RFX-mod and DIII-D in the near future, to further develop the studies started with this Thesis.

Prefazione

Questa Tesi presenta una serie di risultati sullo sviluppo di avanzati schemi di feedback per il controllo di instabilità magnetoidrodinamiche (MHD) e di campi errori ottenuti in due esperimenti toroidali a confinamento magnetico: il reversed-field pinch (RFP) RFX-mod, a Padova, Italia, e il tokamak DIII-D, presso la General Atomics, San Diego, CA, USA.

Negli ultimi anni, questi due esperimenti hanno esplorato differenti tipi di regimi ad alte prestazioni, anche grazie ai loro sofisticati sistemi di controllo attivo. Ad RFX-mod, esperimenti ad alta corrente di plasma, sino a $2MA$, sono stati realizzati per la prima volta in un RFP. Questi esperimenti hanno permesso la scoperta di un nuovo equilibrio elicoidale, auto-organizzato e con buone proprietà di confinamento [40]. Invece, a DIII-D scenari stazionari ed operazioni ad alte prestazioni vengono investigati. I programmi scientifici di questi esperimenti, in particolar modo il controllo di campi errori e di instabilità MHD, possono dare preziosi contributi all'International Thermonuclear Experimental Reactor (ITER) e, più in generale, alla ricerca nel campo della fusione.

Il RFP e il tokamak sono esperimenti toroidali per il confinamento magnetico di plasmi termonucleari. Un'introduzione alla fusione termonucleare, i principali requisiti per sfruttare la fusione come una sorgente di energia per il futuro, il confinamento magnetico del plasma, e il modello MHD che descrive il comportamento del plasma in molti casi di interesse, verranno descritti nel *Capitolo 1*. Il ruolo del controllo dei campi magnetici in feedback per lo sviluppo di regimi operazionali avanzati in RFX-mod e a DIII-D verrà anche discusso in questo *Capitolo*.

Il *Capitolo 2* descrive gli esperimenti sopra citati e i relativi sistemi di controllo dei campi magnetici in feedback. Questi infatti sono muniti di sistemi molto flessibili per il controllo di instabilità MHD e di campi errori. In particolar modo, verranno presentate le strategie di controllo in feedback che sono cruciali per il lavoro discusso in questa Tesi.

Il primo risultato importante di questa Tesi è riportato nel *Capitolo 3* e riguarda l'ottimizzazione del controllore a multi-modo delle instabilità tearing di RFX-mod. I modi tearing, che sostengono la configurazione a campo rovesciato tipica degli esperimenti RFP attraverso un meccanismo di dinamo, non possono essere completamente soppressi dal controllo dei campi magnetici in feeedback. Ciò nonostante, è importante ridurre la loro ampiezza di campo magnetico radiale al bordo del

plasma al più piccolo valore possibile, dal momento che questa produce una deformazione dell'ultima superficie chiusa di flusso, aumentando l'interazione plasma-parete. In questo lavoro, il controllo dei modi tearing è stato ottimizzato utilizzando un modello non lineare che simula la dinamica dei modi tearing in presenza del layout a multipla shell di RFX-mod e del sistema per il controllo di campi magnetici in feedback. Questo modello dei modi tearing è stato sviluppato in un codice chiamato RFXlocking che è stato descritto in [84]. Dato il buon accordo tra le predizioni del modello e il comportamento dei modi nell'esperimento, il codice RFXlocking è stato usato per identificare un nuovo set di parametri di controllo (i.e. i guadagni del feedback), che permetta di ridurre l'ampiezza radiale dei modi tearing al bordo del plasma, mantenendo allo stesso tempo i modi in rotazione ed evitando saturazioni di corrente nelle bobine di controllo. L'approccio per l'ottimizzazione prevede di simulare la dinamica dei modi tearing al variare dei guadagni del feedback, e di identificare un set di guadagni che soddisfa le richieste sopra descritte. Una volta trovato il set di guadagni ispirato dal modello, una lunga campagna sperimentale è stata fatta ottenendo soddisfacenti risultati in termine di riduzione di campo magnetico radiale al bordo del plasma e confermando così le previsioni del codice.

L'ottimizzazione del controllo dei campi magnetici in feedback svolta in questo lavoro di Tesi non ha solo riguardato i modi tearing ma anche i principali campi errori in RFX-mod. La presenza di tagli in direzione poloidale nella struttura conduttiva di RFX-mod modifica il pattern delle correnti immagine indotte dal campo magnetico verticale durante la fase di salita di corrente di plasma, inducendo campi errori localizzati dove i modi tearing hanno un'inteferenza costruttiva. Due tecniche di controllo in feedback sono state utilizzate per sopprimere questi campi errori: uno schema di controllo a multi modo e il disaccoppiatore dinamico.

Per quanto riguarda la prima strategia di controllo, un modello di Simulink del sistema magnetico di feedback di RFX-mod è stato usato per identificare i guadagni del feedback, che permettono di ridurre significativamente l'ampiezza del campo errore, evitando saturazioni di corrente nelle bobine di controllo. Un disaccopiatore dinamico è stato usato per calcolare le correnti nelle bobine di controllo necessarie a cancellare i campi errore. Come verrà descritto nel *Capitolo 4*, durante una campagna sperimentale dedicata, queste due tecniche sono state testate. Il miglior risultato in termini di riduzione dei campi errore è stato ottenuto quando il controllore a multi-modo e il disaccopiatore sono stati usati contemporaneamente. Quando la correzione del campi errori è applicata durante la fase di salita di corrente di plasma, l'interferenza costruttiva tra i modi tearing non è più localizzata vicino ai tagli in direzione poloidale della struttura conduttrice, in questo modo viene ridotta l'interazione plasma-parete in queste zone.

Come accennato precedentemente, gli esperimenti ad alta corrente in RFX-mod hanno rivelato un nuovo regime promettente, in cui l'RFP evolve spontaneamente in uno stato elicoidale Ohmico. Questo nuovo equilibrio magnetico è caratteriz-

zato da un singolo asse magnetico elicoidale e da superfici magnetiche elicoidali all'interno del plasma. Questo produce una diminuzione del trasporto stocastico e la formazione di profili di temperatura elettronica molto ripidi. Nell'ultima campagnia sperimentale è stato dimostrato che un equilibrio elicoidale con elicità (1,-7) può essere indotto e controllato applicando condizioni elicoidali al bordo del plasma per mezzo del sistema magnetico di feedback.

In questo lavoro di Tesi, il *Capitolo 5* e il *Capitolo 6* descrivono l'ottimizzazione delle perturbazioni magnetiche elicoidali usate per controllare l'equilibrio elicoidale. La procedura di ottimizzazione usa le stesse strategie di controllo che sono state adottate per migliorare il controllo dei modi tearing e dei campi errori. Il codice RFXlocking è stato modificato permettendo di applicare condizioni elicoidali al bordo del plasma. In questo modo, la dinamica dei modi può essere simulata con questo nuovo boundary elicoidale, al variare dei guadagni di feedback, dell'ampiezza e della fase delle perturbazioni elicoidali imposte al bordo del plasma. Un approccio di ottimizzazione ispirato dal modello, simile a quello descritto nel *Capitolo 3*, è stata adottato in questo caso per identificare i guadagni di feedback che permettono di produrre il richiesto pattern di campo radiale al bordo del plasma con la minor richiesta di corrente nelle bobine di controllo. Uno scan parziale dei guadagni è stato svolto nell'esperimento e i risultati confermano le predizioni del modello. I risultati salienti dell'ottimizzazione ispirata dal modello e le prestazioni del plasma negli stati elicoidali sostenuti imponendo condizioni elicoidali al bordo plasma sono descritti nel *Capitolo 5*.

Analisi di esperimenti a vuoto, descritte nel *Capitolo 6*, rivelano che, quando una perturbazione rotante di campo magnetico viene applicata dal sistema di feedback, come nel caso degli stati elicoidali descritti sopra, campi errori vengono indotti dalla risposta in frequenza della struttura conduttrice ai campi magnetici esterni che variano nel tempo. Questi campi errori, che sono indotti principalmente dalla presenza di tagli in direzione toroidale e poloidale nella struttura conduttrice, possono in qualche modo influenzare le proprietà di buon confinamento degli stati elicoidali. Per questo motivo un disaccoppiatore dinamico, simile a quello usato per correggere i campi errori durante la fase di salita delle corrente, è stato utilizzato. Esperimenti a vuoto mostrano risultati incoraggianti in termini di riduzione dell'ampiezza del campo errore.

La risposta in frequenza della struttura conduttiva ad un campo magnetico variabile nel tempo è stata esaminata anche nell'esperimento DIII-D, durante una collaborazione tra i gruppi di ricerca di RFX-mod e di DIII-D. Nell'algoritmo di controllo di DIII-D, le misure di campo magnetico sono compensate in tempo reale dai campi magnetici spuri, che possono essere indotti dalle bobine di controllo o dalle bobine assialsimmetriche. Questi contributi esterni sono calcolati dai coefficienti di accoppiamento tra ciascun attuatore e sensore, a frequenza nulla. In questo approccio, gli effetti delle correnti immagine indotte nella struttura conduttiva vengono trascurati. L'importanza di questi effetti che dipendono dalla

frequenza, o effetti AC, per il controllo di RWM e di campi errori è stata valutata analizzando esperimenti precedenti. Le analisi suggeriscono che campi errori possono essere indotti quando viene applicato il controllo in feedback se la risposta in frequenza delle strutture conduttive non è inclusa nell'algoritmo di feedback di compensazione. Questi possono risultare importanti specialmente ad alto β, regime in cui i campi errori residui possono essere amplificati dal plasma. Un algoritmo di compensazione AC è stato implementato e testato in tempo reale in spari a vuoto e in spari Ohmici. Un maggior numero di test di questo algoritmo ad alto β è stato proposto per la prossima campagna sperimentale per testare la sua rilevanza nella performance del plasma quando questo è più soggetto ai campi errori. I risultati più salienti di questo lavoro di Tesi sono discussi nel *Capitolo 7*.

Il *Capitolo 8* riassume le conclusioni principali di questo lavoro e presenta degli esperimenti che posso essere eseguiti ad RFX-mod e a DIII-D nel futuro prossimo che possono indagare ulteriormente gli studi iniziati in questo lavoro di Tesi.

Contents

CHAPTER 1

Magnetically confined fusion plasmas and their active control

In this Chapter, an introduction to controlled thermonuclear fusion and to the magnetic confinement of hot plasmas is first given, to describe several concepts used throughout the Thesis. The main results of this Thesis work regard the development of advanced schemes for the magnetic feedback control of plasma instabilities in reversed-field pinch and tokamak experiments. For this reason, the second part of this Chapter will summarize the main results obtained in this field in recent years. In particular, the discussion will be focused on two devices, which are equipped with advanced magnetic feedback systems for the active control of plasma instabilities and magnetic field errors: the RFX-mod reversed-field pinch and the DIII-D tokamak. These are also the devices where most of this Thesis work has been done.

1.1 Principles of thermonuclear fusion

The well-known problem of limited energy resources and several environmental concerns about the existing energy production techniques urgently ask for the development of renewable and clean energy production methods. In particular, the possible exploitation of thermonuclear fusion, as a commercial source of energy, has motivated researchers for several decades [1]. In fact, thermonuclear fusion has the potential to offer a practically inexhaustible and inherently safe source of energy. Moreover, it has the advantage of not producing either greenhouse gases or long-lived radioactive waste.

Thermonuclear fusion is referred to as the nuclear reaction among two light nuclei that fuse into a heavier one, releasing other reaction products like neutrons. This is a widespread phenomenon in nature. It is well known, for example, that nuclear fusion is the basic process through which the sun and the stars produce power to sustain their high temperatures. By a series of reactions, namely:

$$ {}^{1}_{1}H + {}^{1}_{1}H \longrightarrow {}^{2}_{1}D + e^{+} + \nu_e, \tag{1.1} $$

$$ {}^{2}_{1}D + {}^{1}_{1}H \longrightarrow {}^{3}_{2}He + \gamma, \tag{1.2} $$

$$ {}^{3}_{2}He + {}^{3}_{2}He \longrightarrow {}^{4}_{2}He + 2{}^{1}_{1}H, \tag{1.3} $$

Hydrogen fuses to form Helium. The nuclear rearrangement results in a reduction of the total mass and consequently in a release of energy. However, β^{+}-decay (Equation (1.1)) involves the weak interaction and therefore has a very small cross-section. For energy production on earth, the weak interaction has to be avoided. Alternative reactions involve the heavier Hydrogen isotopes, Deuterium (D) and Tritium (T) [1]:

$$ {}^{2}_{1}D + {}^{2}_{1}D \longrightarrow {}^{3}_{1}T(1.01MeV) + {}^{1}_{1}H(3.02MeV), \tag{1.4} $$

$$ {}^{2}_{1}D + {}^{2}_{1}D \longrightarrow {}^{3}_{2}He(0.82MeV) + {}^{1}_{0}n(2.45MeV), \tag{1.5} $$

$$ {}^{2}_{1}D + {}^{3}_{1}T \longrightarrow {}^{4}_{2}He(3.56MeV) + {}^{1}_{0}n(14.03MeV), \tag{1.6} $$

$$ {}^{2}_{1}D + {}^{3}_{2}He \longrightarrow {}^{4}_{2}He(3.71MeV) + {}^{1}_{1}H(14.64MeV). \tag{1.7} $$

Of all these reactions, the D-T reaction in Equation (1.6) has the highest cross-section at the lowest Deuterium energy, as shown in Figure 1.1, and is therefore the most promising.

Deuterium resources on earth are practically endless. In every liter of seawater, for example, there are $33mg$ of Deuterium. However, unlike Deuterium, Tritium is virtually not existent in nature due to its radioactive half-time of 12.3 years. Nonetheless, it can be produced from Lithium using the neutron-induced fission reactions:

$$ {}^{6}_{3}Li + {}^{1}_{0}n \longrightarrow {}^{4}_{2}He + {}^{3}_{1}T + 4.8MeV, \tag{1.8} $$

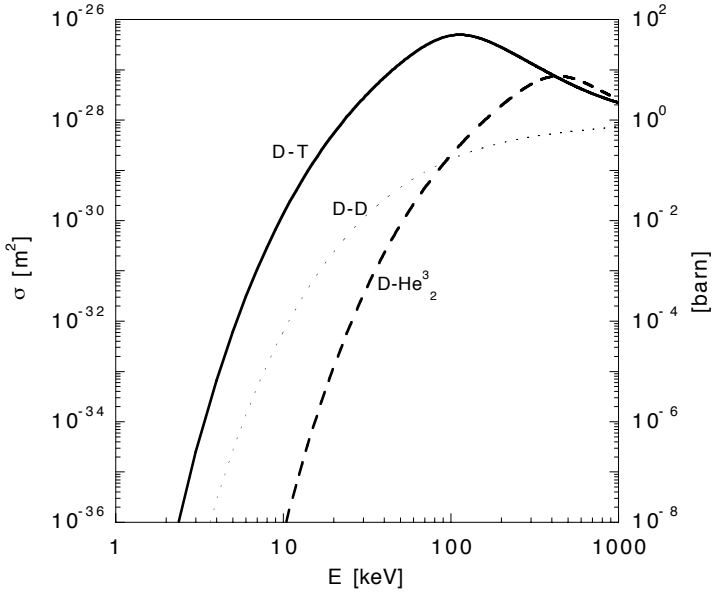

Figure 1.1: Cross-sections of the $D-T$, $D-D$, and $D-{}^3_2He$ fusion reactions as a function of the relative kinetic energy of the reactants.

$$ {}^7_3Li + {}^1_0 n \longrightarrow {}^4_2 He + {}^3_1 T + {}^1_0 n - 2.5MeV. \tag{1.9} $$

A Lithium blanket on the vacuum vessel of fusion reactors is estimated to provide the necessary Tritium source for an unlimited period of time, based on the present Lithium resources. Thus, nuclear fusion promises a practically inexhaustible source of energy.

A main obstacle for a fusion reaction is the Coulomb repulsion of the positively charged nuclei. To overcome the Coulomb barrier, the nuclei require high kinetic energies. The cross-section for the D-T reaction reaches a maximum at a Deuterium energy of about $100keV$, as shown in Figure 1.1. Nevertheless, even at this high energy, the probability of Coulomb scattering is much higher than that of a fusion reaction. Nuclei with sufficient energy have to be confined for many elastic collisions before they undergo a fusion reaction. The most promising solution is to heat a D-T mixture until the thermal velocities are sufficiently high for fusion reactions to become likely.

At the temperatures required for fusion reactions, the Hydrogen isotopes are fully ionized. The electrostatic charge of the ions is neutralized by the presence of an equal number of electrons, resulting in a quasi-neutral gas called *plasma* [2]. In order to maintain a high-plasma temperature, the contact between the plasma and the material walls has to be minimized.

Two methods seem up to now to be promising to realize fusion conditions in the laboratory: the so-called magnetic confinement and inertial confinement approaches.

- *Magnetic confinement* fusion [3], which will be the main focus of this Thesis, uses strong magnetic fields to confine matter in the plasma state. Owing to the Lorentz force, a charged particle in a strong magnetic field makes a spiraling motion around the magnetic field lines. In absence of collisions, and by using magnetic fields with closed geometry, it is thus possible to confine plasmas for relatively long times.

- In *inertial confinement* fusion experiments [4], on the other hand, small volumes of solid matter are brought to sufficiently high temperatures and densities by firing high power lasers from many different directions. This compresses and heats the matter, bringing it to the critical conditions necessary for fusion to occur.

For the energy balance of a fusion reactor to be positive, the energy produced by fusion reactions has to exceed that required to create and sustain the plasma itself. One form of energy loss for a D-T plasma, with electron density n ($n_{D,T} = n/2$) and temperature T, is Bremsstrahlung radiation [2]. The power lost per unit volume due to Bremsstrahlung emission is $P_b = bn^2T^{1/2}$, where b is a function of the effective charge $Z_{eff} = n^{-1}\sum_i n_i Z_i^2$ in a multi-species plasma.

In addition, power losses due to confinement degradation, such as through collisional and turbulent transport phenomena, have to be considered in the power balance. A simple estimate of the energy losses due to mechanisms different from Bremsstrahlung can be made as $P_t = 3nT/\tau_E$, by introducing the characteristic *energy confinement time* τ_E.

The power generated by fusion reactions can be written as $P_n = W_{DT}n^2\langle\sigma v\rangle_T/4$, where $W_{DT} = 17.59MeV$ is the energy released after a single D-T fusion reaction, and $\langle\sigma v\rangle_T$ is the product of the reaction cross-section and the relative velocity of the reactants averaged over a Maxwellian velocity distribution. Note that this last term is a function of temperature. Let us assume that the reaction power P_n balances the energy losses with an efficiency η. The self-sustainment condition is thus:

$$P_b + P_t \leq \eta(P_b + P_t + P_n), \tag{1.10}$$

which can be rewritten as:

$$n\tau_E \geq 3T\left(\frac{\eta}{1-\eta}\frac{W_{DT}}{4}\langle\sigma v\rangle_T - bT^2\right)^{-1}. \tag{1.11}$$

This last expression is also known as *Lawson's criterion* [5]. The right-hand side of Equation (1.11) depends only on temperature, hence the product $n\tau_E$, where the equality is satisfied, can be plotted as a function of T. In Figure 1.2, the curve with efficiency $\eta = 30\%$ is reported, which has a minimum at $T \simeq 20keV$. Equation (1.11) evaluated at this temperature becomes:

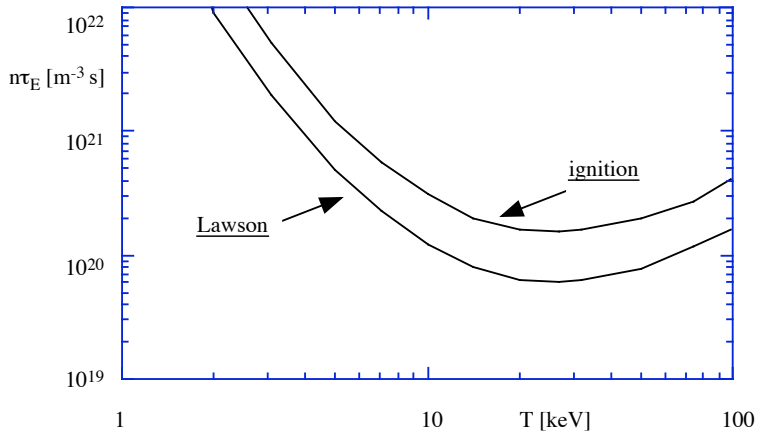

Figure 1.2: The minimum $n\tau_E$ curves for which the Lawson's and ignition criteria are satisfied. The Lawson's curve refers to an efficiency $\eta = 30\%$.

$$n\tau_E \geq 0.6 \cdot 10^{20} m^{-3} s. \tag{1.12}$$

The most probable reactor scenario is the one in which the α particles (${}^4_2He$ nuclei) produced by fusion reactions are confined by the magnetic field and replace all the energy losses by transferring their energy to the plasma, whereas neutrons escape the plasma volume and their energy is converted to electric energy. In this case, the Lawson's criterion must be modified, it is called *ignition criterion* [6], and is written as:

$$P_b + P_t \leq P_\alpha, \tag{1.13}$$

which can be expressed as:

$$n\tau_E \geq 3T \left(\frac{W_\alpha}{4} \langle \sigma v \rangle_T - bT^2 \right)^{-1}, \tag{1.14}$$

where $W_\alpha = W_{DT}/5$ is the energy of a single α particle after a fusion reaction. The $n\tau_E$ curve that corresponds to the equality is shown in Figure 1.2. As the Lawson's criterion curve, the ignition curve has a minimum at $T \simeq 20keV$, and the requirement for ignition at this temperature is:

$$n\tau_E \geq 1.5 \cdot 10^{20} m^{-3} s. \tag{1.15}$$

This last result can also be written through the so-called *fusion triple product*:

$$n\tau_E T \geq 3 \cdot 10^{21} m^{-3} skeV. \tag{1.16}$$

For temperatures $T \sim 20keV$ and electron densities $n \sim 10^{20} m^{-3}$, which in laboratory experiments are fixed by physical and technological constraints, the energy confinement time τ_E must be grater than $1s$.

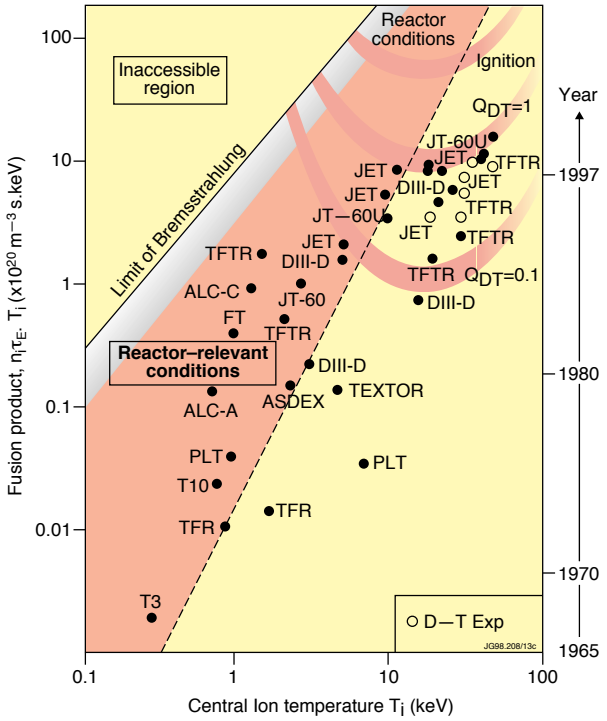

Figure 1.3: Values of the fusion triple product $n\tau_E T_i$ obtained in $D-T$ tokamak experiments as a function of the central ion temperature T_i.

Figure 1.3 shows the values of the fusion triple product reached in fusion devices since the beginning of experiments in magnetic fusion. The plot shows the improvement in confinement achieved up to now and the goal that the scientific community must reach to provide a working fusion power plant. Conditions approaching ignition have been achieved in recent years in different tokamak experiments. Examples of D-T discharges from the European tokamak experiment JET and the American experiment TFTR, where record high fusion power was produced for the first time, respectively $16MW$ and $10MW$, are shown in Figure 1.16 [7].

Equation (1.16) has shown that high-plasma density and temperature are essential to meet the conditions for a fusion power plant to work. Increasing the plasma pressure $p = nT$ thus means advancing towards economical power plant conditions. Commonly the parameter β, which is the ratio of the plasma pressure and the magnetic pressure:

$$\beta = \frac{< p >}{B^2/2\mu_0}, \tag{1.17}$$

with <> denoting a volume average, is used as a figure of merit for the efficiency with which the magnetic field confines the plasma. The toroidal or the poloidal

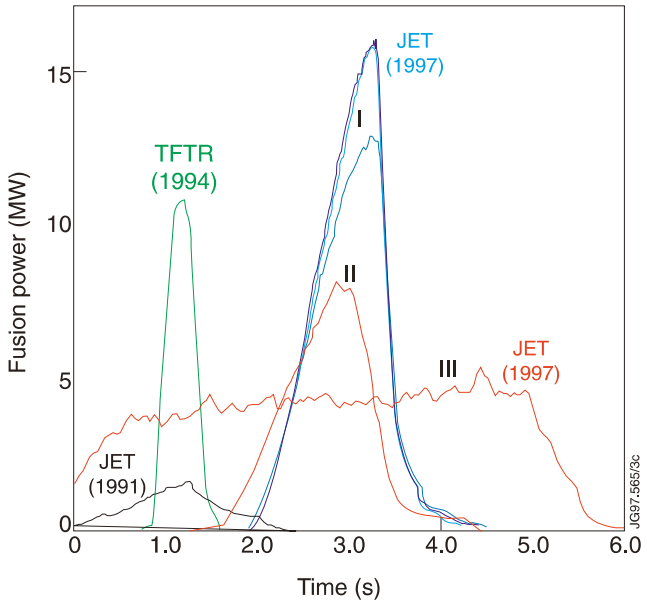

Figure 1.4: Waveforms of the fusion power produced in $D-T$ discharges in the JET and TFTR tokamak experiments (this Figure is taken from [7]).

magnetic field separately can be used in the above definition, and in this case the β parameter is called poloidal or toroidal beta, β_θ and β_ϕ, respectively. The toroidal beta, in particular, is a meaningful measure of the plasma confinement efficiency, since the cost paid to confine a plasma is mainly related to the toroidal field strength.

High-β values are desirable for an economic power balance in a fusion reactor. Nonetheless, they are difficult to achieve experimentally because of the onset of plasma instabilities, which will be described more in detail in §1.2.2. It will be also shown in the following that controlling such instabilities with active means may be required even in a reactor-relevant experiment.

1.1.1. ITER: International Thermonuclear Experimental Reactor

The large experimental database obtained in the last 30 years in several magnetic confinement experiments and the increasing capability of numerical simulations have provided the international community the physics basis for the design of a burning plasma experiment based on the tokamak concept, which is called International Thermonuclear Experimental Reactor (ITER) [8, 9]. A schematic view of ITER is displayed in Figure 1.5. The main physics goals of ITER are:

- to achieve extended burn in inductively-driven plasmas with $Q = Q_{fus}/Q_{aux}$, the ratio of fusion power to auxiliary heating power, of at least 10 for a range

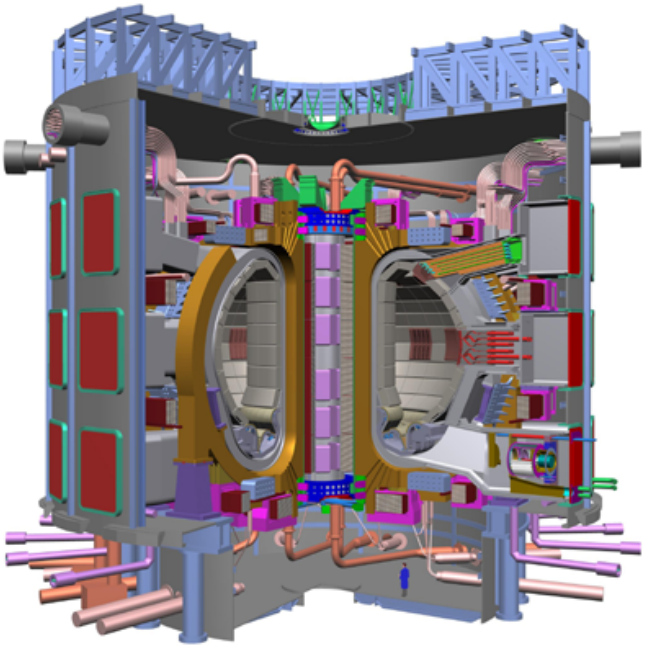

Figure 1.5: Scheme of the International Thermonuclear Experimental Reactor (ITER) design.

of operating scenarios and with a duration sufficient to achieve stationary conditions;

- to demonstrate steady-state operation with $Q \geq 5$ using a large fraction of non-inductive plasma current and, in particular, of the so-called *bootstrap current* [10], which can be driven by strong pressure gradients.

The ITER nominal fusion power output is expected to be about $500MW$. To achieve this goal, the chosen machine parameters are the following: major radius $R_0 = 6.2m$, minor radius $a = 2m$, maximum magnetic field $B = 5.3T$, and plasma current $I_p = 15MA$. The discharge duration is designed to be about $300 - 500s$, which can be regarded as a stationary condition on the time scales characteristic of the plasma processes. All of these parameters have been predicted for plasmas with density $n_e \approx 10^{20}m^{-3}$ and core electron and ion temperatures $T_e \approx 8.8keV$ and $T_i \approx 8keV$, respectively.

ITER will offer the possibility of studying several reactor relevant scientific and technological issues, which are beyond the present experimental capabilities. In particular, regimes in which the α particles contribute significantly to the plasma pressure are very interesting. In these conditions, a class of plasma instabilities is predicted to be driven by the α particles, which can only in part be studied in the present tokamaks. The study of plasma instabilities and of their control is thus an important aspect of the research in burning scenarios. A variety of

technological issues could also be studied in ITER, like for example the test of advanced materials facing very large heat and particle fluxes, the test of concepts for a tritium breeding module, and many others.

The auxiliary systems needed to achieve the conditions expected in ITER are an external heating and current drive capability of about $73MW$ and several advanced diagnostics for both analysis and plasma control. All of these requirements are expected to solve many of the scientific and engineering issues concerning a burning plasma, and could allow the scientific community to make a significant next step towards the demonstration of a tokamak power-plant.

1.2 Magnetic plasma confinement

In fusion research, several magnetic field geometries have been investigated, such as magnetic mirrors, linear, and toroidal configurations [3], to seek the best conditions for plasma confinement. Among them the toroidal geometry has given the best confinement performances. This section will be dedicated to a brief introduction to the principles of magnetic plasma confinement in toroidal devices and, in particular, in the so-called tokamak and reversed-field pinch (RFP) configurations.

We define in Figure 1.6 the toroidal coordinates (r, θ, ϕ), which will be used in the rest of the Thesis: r is called radial coordinate, θ and ϕ are the poloidal and toroidal angles, respectively. With R_0 and a we indicate the major and minor radius of the torus, respectively.

Magnetic field lines in toroidal experiments have both a poloidal component, B_θ, which is mainly generated by an externally driven toroidal plasma current

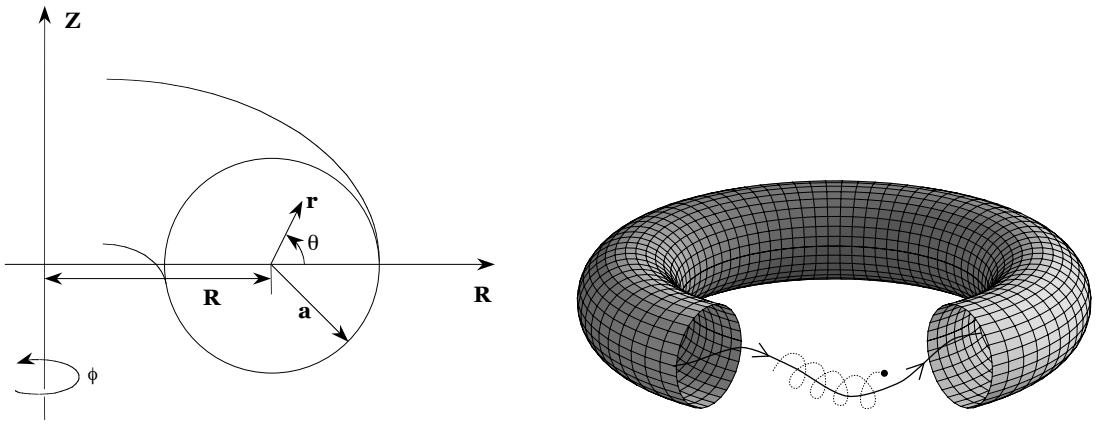

Figure 1.6: The system of toroidal (r, θ, ϕ) and cylindrical coordinates (R, ϕ, Z) (on the left). A scheme showing the principle of toroidal confinement (on the right): a charged particle gyrates around a helical magnetic field line and is thus confined within a toroidal vacuum vessel.

density, j_ϕ, and a toroidal component, B_ϕ, which in some configurations is only in part produced by currents flowing in external conductors. The plasma itself can produce a large fraction of current through dynamo effects, which will be discussed more deeply in §1.2.4. Magnetic field lines are thus helixes, which wound around the torus lying over toroidal surfaces called *magnetic surfaces*. Helical magnetic field lines are described by the so-called *safety factor*, q, which is defined as a function of radius as follows:

$$q(r) = \frac{rB_\phi(r)}{R_0 B_\theta(r)}. \tag{1.18}$$

The inverse of this quantity represents the number of poloidal turns done by a helical field line per one toroidal turn. The name safety factor comes from the fact that this quantity is crucial to determine several features of the plasma instabilities, as it will be shown more in detail in §1.2.2.

1.2.1. The magnetohydrodynamic description of plasmas

A fluid model called *resistive magnetohydrodynamics (MHD)* is commonly used to describe a large variety of plasma properties, like for instance the magnetic equilibria used to confine thermonuclear plasmas and several instabilities associated with them. A general introduction to the resistive MHD model can be found for example in [2, 3, 11].

Let us consider here for simplicity a Hydrogen plasma, but it would be possible to extend the present description also to multiple species plasmas. In the so-called two-fluid MHD, where the two fluids are that of ions and of electrons, the mass and momentum continuity equations can be written as follows:

$$\frac{\partial \rho_\alpha}{\partial t} + \nabla \cdot (\rho_\alpha \mathbf{u}_\alpha) = 0, \tag{1.19}$$

$$\rho_\alpha \left(\frac{\partial \mathbf{u}_\alpha}{\partial t} + \mathbf{u}_\alpha \cdot \nabla \mathbf{u}_\alpha \right) = \sigma_\alpha \mathbf{E} + \mathbf{j} \times \mathbf{B} - \nabla p_\alpha + \mathbf{R}_{\alpha\beta}, \tag{1.20}$$

where $\alpha, \beta = i, e$ (i.e. ions or electrons), $\rho_\alpha = m_\alpha n_\alpha$ is the mass density, and $\sigma_\alpha = \pm e n_\alpha$ is the charge density of the single species. No particle or momentum sources are considered here for simplicity. The electromagnetic quantities $\mathbf{E}$, $\mathbf{B}$, and $\mathbf{j}$ have the usual meaning. The first two terms in the right-hand side of Equation (1.20) represent the electromagnetic forces, $-\nabla p_\alpha$ is the kinetic pressure force, which is in general a tensor quantity, and $\mathbf{R}_{\alpha\beta}$ is the rate at which momentum is gained or lost by species α due to collisions with species β. Note in particular that the following relation holds: $\mathbf{R}_{\alpha\beta} = -\mathbf{R}_{\beta\alpha}$.

A plasma can be described as a single fluid by introducing the following variables: the mass density $\rho = \rho_i + \rho_e$, the kinetic pressure $p = p_i + p_e$, the mass fluid

velocity $\mathbf{u} = (\rho_i \mathbf{u}_i + \rho_e \mathbf{u}_e)/\rho$, and the charge density $\sigma = e(n_i - n_e)$. By combining the two-fluid Equations (1.19) and (1.20) and by using the above relations, it is simple to derive the following fluid equations (the derivation reported in [2] has been adopted):

$$\frac{\partial \rho}{\partial t} + \nabla \cdot (\rho \mathbf{u}) = 0, \tag{1.21}$$

$$\rho \left(\frac{\partial \mathbf{u}}{\partial t} + \mathbf{u} \cdot \nabla \mathbf{u} \right) = \sigma \mathbf{E} + \mathbf{j} \times \mathbf{B} - \nabla p, \tag{1.22}$$

$$\mathbf{E} + \mathbf{u} \times \mathbf{B} = \eta \mathbf{j} + \frac{\mathbf{j} \times \mathbf{B} - \nabla p_e}{ne}. \tag{1.23}$$

Equation (1.21) is the mass continuity equation, Equation (1.22) is the momentum continuity equation, also called single-fluid equation of motion, and Equation (1.23) is the generalized Ohm's law, which is not strictly a single-fluid equation due to the presence of the ∇p_e term.

The generalized Ohm's law is derived from the electron equation of motion under the often verified assumption of negligible electron inertia, and by writing the e-i collision term as follows: $\mathbf{R}_{ei} = m_e n_e \langle \nu_{ei} \rangle (\mathbf{u}_i - \mathbf{u}_e) = \eta n e \mathbf{j}$. Here the simple expression $\langle \nu_{ei} \rangle = \eta n_e e^2 / m_e$ for the e-i collision frequency averaged over a Maxwellian distribution is used, η being the plasma resistivity. In a plasma, the fluid motion across a magnetic field induces the electric field $\mathbf{u} \times \mathbf{B}$. The last two terms in the right-hand side of Equation (1.23) arise due to the Hall and the diamagnetic effects, respectively.

What it is usually referred to as *resistive MHD model* can be derived by the fluid Equations (1.21), (1.22) and (1.23) under the following two approximations: (i) charge quasi-neutrality, $n_i \simeq n_e$, which permits one to drop the term $\sigma \mathbf{E}$ in Equation (1.22); and (ii) small ion Larmor radius compared with the scale-length of the fluid motion, which causes the Hall and diamagnetic terms in Ohm's law to be negligible with respect to the other terms.

The Maxwell equations must be added to this system of equations. The displacement current $\epsilon_0 \mu_0 \partial \mathbf{E}/\partial t$ can be neglected in most cases of interest. A closure for the heat flux tensor is required. To this purpose, an equation of state for pressure is often used of the form $p \propto n^\gamma$. The exponent γ can be chosen depending on the phenomena to be modelled. For example, $\gamma = 1$ represents isothermal compression and $\gamma = 5/3$ adiabatic compression. The resistive MHD model is thus constituted by a set of single-fluid equations, which can be summarized as follows:

$$\begin{aligned} &\frac{\partial \rho}{\partial t} + \nabla \cdot (\rho \mathbf{u}) = 0 && \nabla \times \mathbf{B} = \mu_0 \mathbf{j} \\ &\rho \left(\frac{\partial \mathbf{u}}{\partial t} + \mathbf{u} \cdot \nabla \mathbf{u} \right) = \mathbf{j} \times \mathbf{B} - \nabla p && \nabla \cdot \mathbf{B} = 0 \\ &\mathbf{E} + \mathbf{u} \times \mathbf{B} = \eta \mathbf{j} && \nabla \times \mathbf{E} = -\tfrac{\partial \mathbf{B}}{\partial t} \quad . \end{aligned} \tag{1.24}$$

By combining Faraday's law with Ohm's law, it is simple to derive the following equation, which describes the coupled dynamics of the magnetic and fluid velocity fields in the resistive MHD framework:

$$\frac{\partial \mathbf{B}}{\partial t} = \nabla \times (\mathbf{u} \times \mathbf{B}) + \frac{\eta}{\mu_0} \nabla^2 \mathbf{B}. \tag{1.25}$$

The first term on the right-hand side in Equation (1.25) describes convection of the magnetic field with the plasma and its amplification or reduction due to compressive motion perpendicular to the magnetic field. Starting from this equation, it is possible to show that, in the *ideal* MHD limit, i.e. in the case where the resistivity η is negligible, the magnetic field lines move like if it were *frozen* to the plasma. The second term describes instead resistive diffusion of the field across the plasma.

In stationary ($\partial/\partial t = 0$) and static ($\mathbf{u} = 0$) conditions, the following equilibrium equation follows from the single-fluid MHD equation of motion:

$$\mathbf{j} \times \mathbf{B} = \nabla p. \tag{1.26}$$

This equation is often used to describe the balance among the confining magnetic force and the thermal expansion force in a plasma. Two important examples of equilibria used to confined a toroidal plasma will be described in §1.2.3.

1.2.2. MHD instabilities of toroidal plasmas

The MHD equations introduced in §1.2.1 predict that under certain conditions a small perturbation in a fluid quantity, like for example the density, the fluid velocity, or the magnetic field, can grow unstable in time. These phenomena are called MHD instabilities and are very important in determining the dynamics of many natural and laboratory plasmas [12]. They can be present also in toroidal fusion devices, where they influence in many ways the global plasma properties and can deteriorate the plasma confinement performances.

A perturbation $\tilde{\mathbf{A}}$ of a quantity $\mathbf{A}$ in a toroidal plasma can be Fourier analyzed as follows:

$$\tilde{\mathbf{A}}(\mathbf{r}) = \sum_{\mathbf{k}} \tilde{\mathbf{A}}_{\mathbf{k}}(r) e^{i(\mathbf{k}\cdot\mathbf{r} - \omega t)} = \sum_{\mathbf{k}} \tilde{\mathbf{A}}_{\mathbf{k}}(r) e^{i(m\theta + n\phi - \omega t)}, \tag{1.27}$$

where $\mathbf{k} = (k_r, k_\theta, k_\phi) = (k_r, m/r, n/R_0)$ is the wavevector in toroidal coordinates and m and n are the *poloidal* and *toroidal mode numbers*, respectively. Each couple (m, n) represents a helical perturbation, or mode. The angular frequency ω is in general a complex quantity, $\omega = \omega_R + i\omega_I$, of which the real part describes the propagation velocity, while the imaginary part represents an exponential growth, if $\omega_I > 0$, or damping of the perturbation amplitude, if $\omega_I < 0$.

A helical magnetic perturbation with wavevector $\mathbf{k}$ can become unstable if it fulfills the resonance condition $\mathbf{k} \cdot \mathbf{B} = 0$, where $\mathbf{B} = (0, B_\theta, B_\phi)$ is the equilibrium magnetic field. In fact, a perturbation with $\mathbf{k} \cdot \mathbf{B} \neq 0$ would bend the mean magnetic field and it would be thus energetically unfavored. The above resonance condition can be rewritten as follows:

$$\mathbf{k} \cdot \mathbf{B} = \frac{m}{r} B_\theta + \frac{n}{R_0} B_\phi = 0 \qquad \longrightarrow \qquad q(r) = \frac{r}{R_0} \frac{B_\phi(r)}{B_\theta(r)} = -\frac{m}{n}. \tag{1.28}$$

This shows that helical instabilities can grow only at radial positions where the safety factor assumes rational values. For this reason, these positions are called *rational* or *resonant radii* and will be described later on for the tokamak and the RFP toroidal configurations.

Similarly to what happens in neutral fluids, a plasma instability can be driven, for instance, by current or pressure gradients. Under certain conditions, these can provide the necessary free-energy for a whatever small perturbation to grow unstable. In the following, two examples of MHD instabilities that will be encountered in this Thesis will be described.

The kink mode. The potentially strongest ideal MHD instability is the kink mode. It is so named because it leads to a kinking of the magnetic surfaces, as shown schematically in Figure 1.7. The kink mode has a relatively high growth rate of the order of τ_A^{-1}, where τ_A is the Alfvén time expressed as $\tau_A = a\sqrt{\mu_0 \rho}/B$, being a the plasma radius. Usually τ_A amounts to about $1\mu s$ in typical laboratory fusion plasmas.

It can be demonstrated that a kink mode can in principle be stabilized by a perfectly conducting wall [1]. As the plasma moves during the kink mode evolution, eddy-currents are induced in the wall. In general, these currents tend to oppose the plasma motion and thus provide stabilization. Nonetheless, if the wall resistivity is considered, eddy-currents will decay on a resistive diffusion time scale and reduce the fast growth rate of the kink mode to the time for the resistive diffusion of the magnetic flux through the wall, $\tau_w = \mu_0 \sigma a \delta$, being σ, a, and δ the conductivity of the resistive wall, the minor radius, and its thickness, respectively. τ_w is of the order of several ms in present day machines. The kink mode is thus reverted to a slowly growing mode called *resistive-wall mode* (RWM).

The kink mode, and in particular the so-called *external kink mode*, has often been considered as a major obstacle to achieving high-β, values since pressure

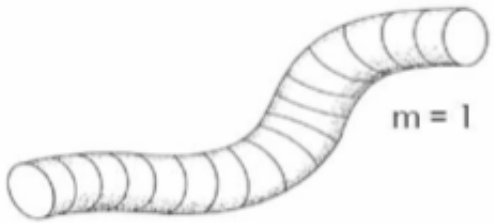

Figure 1.7: Plasma column deformed by a kink instability.

is the main drive of the mode in these operational regimes, as explained in [13]. The interest for high-β plasma operation is clear when the triple fusion product is rewritten in terms of β_ϕ, $nT\tau_E = \beta_\phi B_\phi^2 \tau_E$. In the so-called advanced tokamak (AT) scenarios, the aim is to develop steady-state tokamak operations with high fusion gain and very low or no inductive current drive. This implies operations at high toroidal beta with the largest possible fraction of self-generated bootstrap current [14].

The bootstrap current is a toroidal current produced in the presence of a pressure gradient, associated with the existence of trapped particles. These trapped particles must be able to complete their orbits, the so-called banana orbits, so a requirement for the existence of the bootstrap current is that the collision frequency is less than the banana bounce frequency. The difference in particle density on banana orbits crossing a given radial position then leads to a net toroidal current, the bootstrap current.

Typically the fraction of plasma current driven by the bootstrap mechanism scales as $f_{BS} = I_{boot}/I_p \propto \beta_\theta$ [15]. Hence, optimizing simultaneously both the fusion power density and the bootstrap current fraction requires to operate at large $\beta_\phi \beta_\theta \propto \beta_N^2$ values.

Both experiment and theory show that high-β_N values can be achieved by proper plasma shaping, characterized by a strong elongation and triangularity, and by broad pressure profiles [16]. As it will be described more in detail in §1.3.2, experiments at high-β_N were made possible in DIII-D by a combination of active stabilization of RWMs and strong plasma rotation produced by neutral beam injection [17, 18].

The tearing mode Another kind of perturbation discussed in this work is the so-called *tearing mode* [19]. This is a dominant instability in RFP plasmas. Tearing modes are driven unstable by a gradient in the current density parallel to the magnetic field in presence of a finite plasma resistivity. The name of this instability comes from the fact that the magnetic field lines tear and reconnect during its evolution. This is represented in Figure 1.8, where a sheared magnetic field is shown, which has also a strong magnetic field perpendicular to the x-y plane.

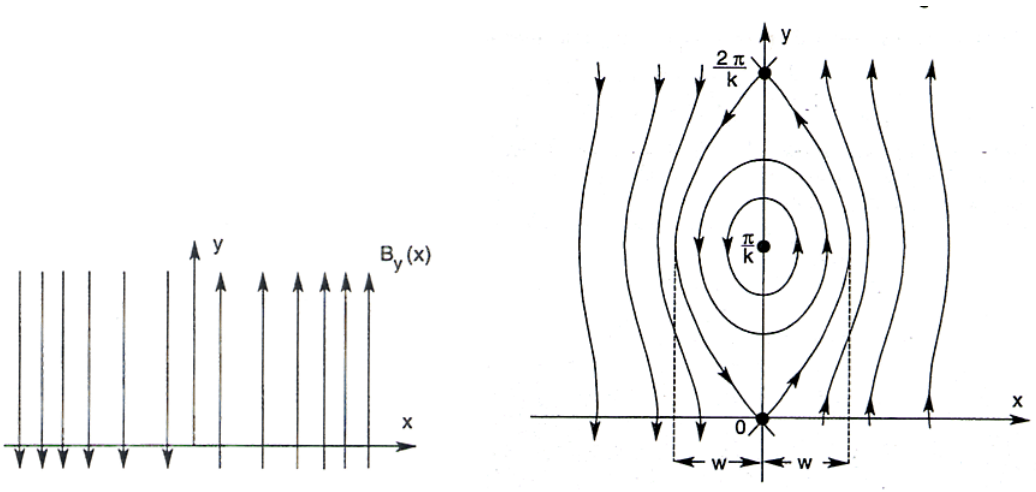

Figure 1.8: A sheared magnetic field in the x-y plane, plus a strong perpendicular z-component (left); the resultant magnetic field lines, after bending and reconnection due to the tearing instability (right). A magnetic island forms in this magnetic configuration, whose separatrix divides two regions with different field line topology.

Such a magnetic configuration is produced by a current profile with a gradient localized where the B_y component changes its sign. It is possible to show that, when this gradient is sufficiently high, a tearing instability is triggered, which causes the magnetic field lines to bend and reconnect, as represented in the figure. The resultant magnetic configuration is characterized by the formation of a so-called *magnetic island*. In toroidal plasmas, such islands have a helical structure, as it will be better described at the end of this Chapter. The interested reader can find more information in [2, 12, 19] and references therein. In the following section, it will be shown that tearing modes play an important role in sustaining the magnetic field configuration in RFP devices.

1.2.3. The tokamak and the RFP equilibria

In this Thesis work, two toroidal magnetic field configurations will be considered: the tokamak [6] and the RFP [20, 21]. These are similar under many respects. In particular, they both belong to the class of *toroidal pinch* devices, in which a toroidal current is inductively driven by an external circuit and generates a poloidal magnetic field that confines and compresses the plasma [11]. In both cases, the toroidal magnetic field is in part generated by external coils. But these two configurations present also some important differences, both in the basic physics processes underlying their dynamics and in more technical aspects. A description of them is presented in the following.

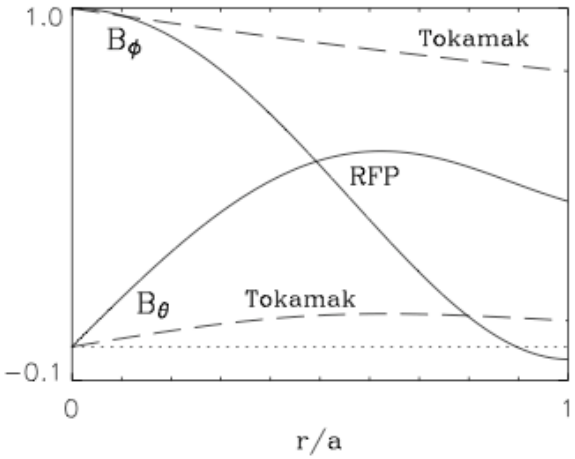

Figure 1.9: Typical radial profiles of the toroidal B_ϕ and poloidal B_θ components of the equilibrium magnetic field in a tokamak (dashed lines) and a RFP (continuous lines). The profiles are normalized to the value of B_ϕ in the plasma center at $r/a = 0$.

Tokamak. This configuration is characterized by a relatively strong toroidal magnetic field B_ϕ and a much weaker poloidal magnetic field $B_\theta \sim 10^{-1} B_\phi$, as shown by their radial profiles in Figure 1.9. The toroidal magnetic field can reach values up to $8T$ in high-field machines, like for example FTU in Rome (Italy). Superconducting coils are often needed to produce such strong magnetic fields for long tokamak operation, which may represent a severe technological issue for future tokamak reactors.

Given these magnetic field profiles, the tokamak safety factor usually increases monotonically with the radial coordinate r, with typical values greater or close to unity in the core, as represented in Figure 1.10. For stability requirements tokamak operation is preferable at $q > 1$, which is called *Kruskal-Shafranov limit*. When a rational surface $q = 1$ is present in the plasma, a strong $(m = 1, n = 1)$ kink instability can grow unstable. This has usually a sawtooth-like dynamics and causes confinement losses. In some cases, it can even lead to current disruptions, which can severely damage the vessel components. Other types of safety factor profiles have been studied for advanced tokamak operation, like for example non-monotonic profiles, which use magnetic and flow shear to stabilize plasma micro-turbolence and achieve enhanced confinement conditions [6].

The Kruskal-Shafranov limit imposes a limitation on the maximum achievable plasma current and related Ohmic heating in tokamaks, so that additional heating methods, like for example neutral beam or radio-frequency heating, are needed to reach thermonuclear conditions.

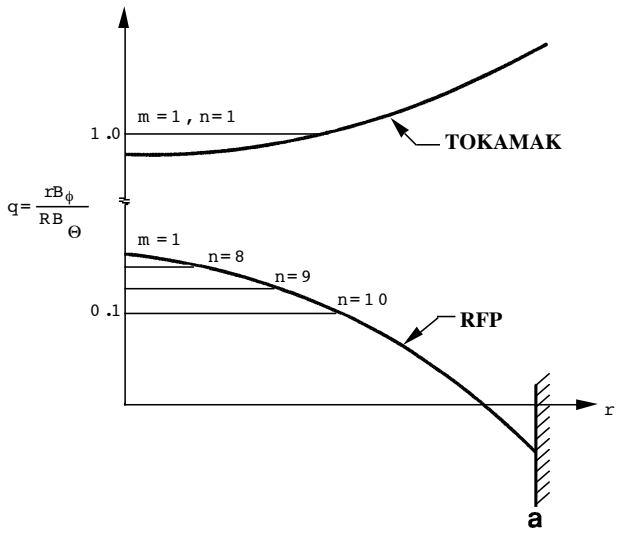

Figure 1.10: Safety factor profiles for a tokamak and a RFP. Horizontal lines indicate the $(m = 1, n)$ rational radii.

Reversed-field pinch. The RFP magnetic configuration is a near-minimum energy state to which the plasma spontaneously relaxes [22]. The force-free part of the magnetic field distribution is described by $\nabla \times \mathbf{B} = \mu \mathbf{j}$, where μ describes the parallel component of the current density, $\mathbf{j}$, as $\mu = \mu_0 \mathbf{j} \cdot \mathbf{B}/B^2$. In the fully relaxed minimum energy state described by Taylor μ is uniform across the plasma, the plasma kinetic pressure is zero and the magnetic field profiles are given, by the zero- and first-order Bessel functions, $B_\theta = B_0 J_1(\mu r)$, and $B_\phi = B_0 J_0(\mu r)$.

Differently from the tokamak, the strength of the toroidal and poloidal components of the magnetic field in the RFP is comparable and relatively weak, $B_\phi \sim B_\theta$, as shown in Figure 1.9. These relatively weak magnetic fields impose less demanding technological issues in this device.

The name RFP comes from the fact that the toroidal magnetic field reverses its sign near the plasma edge. As a consequence, the safety factor profile also changes its sign at the same radius, as shown in Figure 1.10. The RFP is thus an intrinsically low-safety factor device. For this reason, a broad spectrum of $(m = 1, n \gtrsim 2R_0/a)$ modes is resonant throughout the plasma radius, and $(m = 0, n \geqslant 1)$ modes are resonant at the reversal radius. This has many consequences on the dynamics of this configuration and on its transport properties, as it will be described in the next Paragraph.

Different from what happens in tokamaks, low safety factor operation in the RFP does not bring to dangerous disruptive behavior. This is due to the combined action of a high level of magnetic shear, which characterizes this configuration and has a strong stabilizing function on the modes, and to the presence of a conducting

shell, which passively reacts against fast growing magnetic perturbations, which will be explained with more details in Chapter 2.

For all the above reasons, the plasma current in the RFP is not limited by the Kruskal-Shafranov limit, as it happens in tokamaks. As an effect, the RFP can in principle operate at higher β values than in tokamak of comparable plasma current.

Related to the equilibrium magnetic field, two parameters are often used to describe RFP equilibria: the *pinch parameter*, Θ, and the *reversal parameter*, F, which are defined as follows:

$$\Theta = \frac{B_\theta(a)}{\langle B_\phi \rangle} \qquad F = \frac{B_\phi(a)}{\langle B_\phi \rangle}, \tag{1.29}$$

where $\langle \dots \rangle$ indicates an average over a poloidal cross-section. In terms of these quantities, the tokamak is typically a low-Θ device with $F > 0$, while the RFP is a relatively high-Θ configuration, with $F < 0$.

Even though in the last years tokamaks have reached much better confinement performances than RFPs, recent results on enhanced confinement operation in these devices seem to open a promising future for them. In particular, at the end of this Chapter, high-performance plasma operation in the RFX-mod RFP experiment [23], obtained recently with the exploration of high-plasma currents up to $2MA$ [24], will be described.

1.2.4. Need of a dynamo mechanism in the RFP

If a RFP equilibrium was governed only by resistive diffusion, the characteristic reversal of the toroidal magnetic field would be lost very soon and the discharge duration would be limited in time. A static cylindrical conductor with minor radius a subject to resistive diffusion is described by the following equation:

$$\frac{\partial \mathbf{B}}{\partial t} = \frac{\eta}{\mu_0} \nabla^2 \mathbf{B}, \tag{1.30}$$

which implies that the toroidal magnetic flux decays exponentially in time with a time constant $\tau_R = \mu_0 a^2/\eta$, as it is shown in Figure 1.11 for a RFP discharge, and spatial gradients of $\mathbf{B}$ tend to be smoothed. Here the experimental toroidal magnetic flux in a RFX shot (continuous line) is compared with that computed from Equation (1.30) (dashed line). It is observed that the RFP configuration lasts as long as the plasma current is sustained, which is usually longer than the resistive diffusion time. Some mechanism must be present that regenerates the magnetic field continuously lost through resistive diffusion. As anticipated above, this mechanism is called *dynamo*.

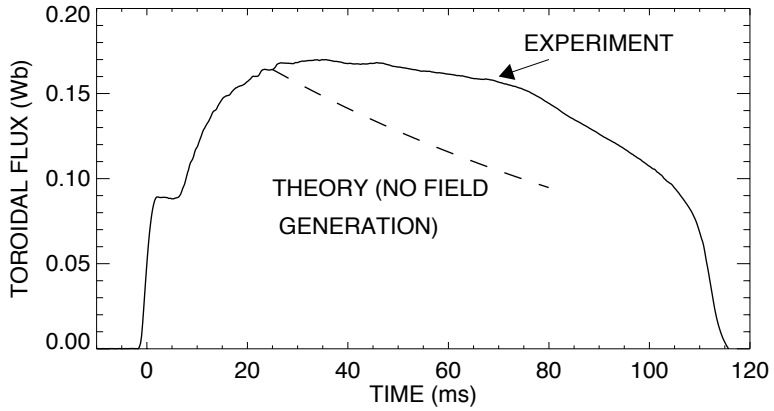

Figure 1.11: Waveform of the toroidal magnetic flux in a RFX discharge (continuous line), and comparison with that predicted by a resistive diffusion cylindrical model without dynamo (dashed line).

To understand the dynamo mechanism in the RFP, it has to be highlighted that the magnetic field profiles of this configuration, and in particular the characteristic reversal of the toroidal magnetic field, cannot be sustained in a toroidally symmetric plasma. Let us consider the parallel component of the mean-field Ohm's law:

$$E_{||} = \frac{\mathbf{E}\cdot\mathbf{B}}{B} = \frac{E_\phi B_\phi}{B} = \eta j_{||}. \tag{1.31}$$

Here $\mathbf{E} = E_\phi \hat{\phi}$ is the externally applied electric field, which has only a toroidal component. Since E_ϕ and B are always positive throughout the radius, $E_{||}$ at each radial position is proportional to B_ϕ, which reverses its sign near the edge. On the other hand, the term $\eta j_{||}$ is always positive, which shows that other terms are needed to balance the Ohm's law. This mismatch is represented in Figure 1.12, which has been obtained with a MHD simulation: current is over-driven in the core, where the applied electric field is almost parallel to the magnetic field $E_{||} \simeq E_\phi$, while it is under-driven near the edge, where $E_{||} \simeq E_\theta$.

The RFP is externally driven by the applied toroidal electric field E_ϕ. Ohmic deposition is higher in the core and thus tends to produce peaked electron temperature profiles. Given the inverse dependence of the plasma resistivity on electron temperature $\eta \propto T_e^{-3/2}$ [2], a local increase in electron temperature brings to a decrease in resistivity, and hence to a further peaking of the current density profile and related Ohmic deposition. In this way, steep spatial gradients of the normalized current density profile $j_{||}/B$ tend to form, which have enough free-energy to drive unstable a broad spectrum of tearing modes with $(m = 1, n \geq 2R_0/a)$. Modes whose resonance is inside the reversal radius have negative toroidal mode

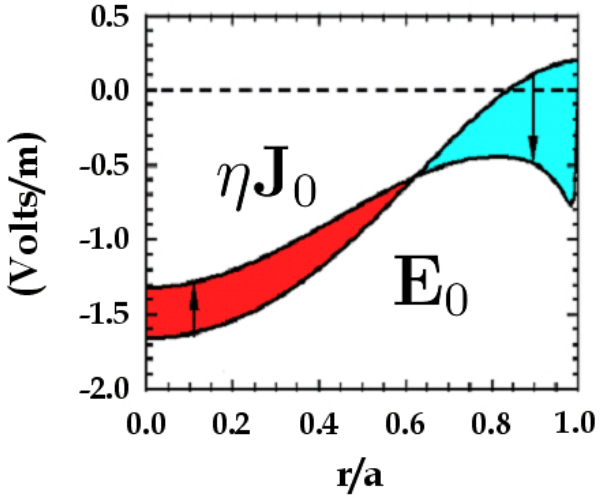

Figure 1.12: The applied parallel electric field $E_{||}$ and the $\eta j_{||}$ term from a MHD simulation. The mismatch between these two terms in Ohm's law is balanced by the dynamo terms, which oppose to the externally driven toroidal current in the core (anti-dynamo effect) and drive poloidal current at the edge (dynamo effect).

number in the convention used here.

RFX-mod discharges with low plasma current, below $1MA$, are characterized by a broad spectrum of tearing modes, with toroidal mode numbers in the range $n \in [-16, ..., -7]$ and comparable amplitude. In this case, the plasma is in the so-called *multiple-helicity* (MH) state. In MH states, the magnetic islands associated with each tearing mode overlap and produce a stochastic magnetic field, which drives anomalous heat and particle transport [21].

Such a spectrum of tearing modes plays an important role, since their interaction produces the mean dynamo electric field necessary to sustain the magnetic configuration in time. For this reason, they are also called *dynamo modes*. In fact, if we write the magnetic and velocity fields as a sum of a mean-field plus a fluctuation term, $\mathbf{B} = \mathbf{B}_0 + \tilde{\mathbf{b}}$ and $\mathbf{v} = \mathbf{v}_0 + \tilde{\mathbf{v}}$, a new mean-field electric field term arises in the parallel Ohm's law, which is called dynamo electric field $\mathbf{E}_d$, and is given by the product of the velocity and magnetic field fluctuations:

$$E_{0||} + E_{d||} = E_{0||} + \langle \tilde{\mathbf{v}} \times \tilde{\mathbf{b}} \rangle_{||} = \eta j_{0||}. \tag{1.32}$$

On the other hand, visco-resistive MHD simulations predict that the dynamo mechanism required to sustain the RFP equilibrium can be provided by the non-linear saturation of a single tearing mode, in the so-called single helicity (SH) state [25]. SH states do not suffer the high level of magnetic turbulence typical of a RFP in the MH state. This state would thus be beneficial for plasma confinement.

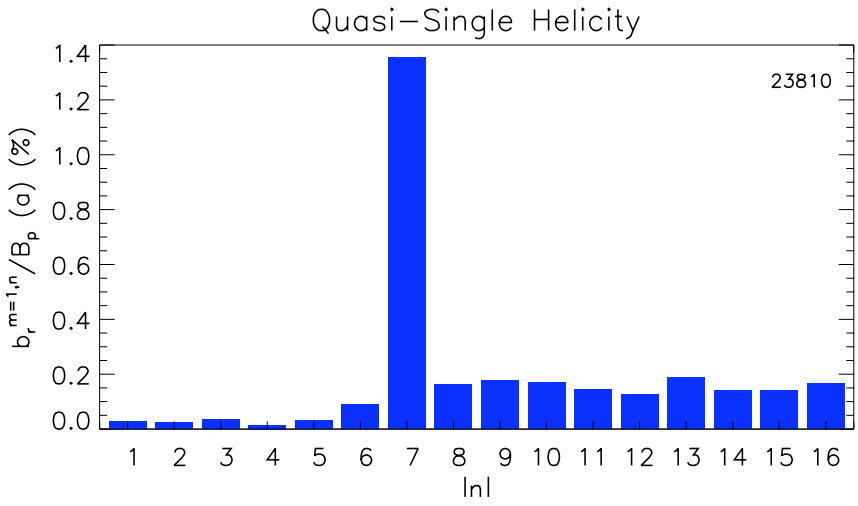

Figure 1.13: Typical toroidal mode number spectrum of $m = 1$ modes in a quasi-single helical state. The flat-top average of the radial magnetic field amplitude normalized to the poloidal magnetic field of each $(1, n)$ mode, $b_r^{m=1,n}/B_p(a)(\%)$, is shown for a $1.5MA$ plasma experiment (23810).

On the experimental side, in several machines the plasma was observed transiently in a quasi-SH (QSH) state [26, 27, 28, 29]. QSH states are the closest experimental approximation of the theoretical SH state. In QSH states one single $m = 1$ mode dominates the magnetic spectrum, but other modes with finite, low amplitude are still present and contribute to some residual magnetic chaos. Usually these modes are named *secondary* modes.

In RFX-mod, at relatively high-plasma currents, above $> 1MA$, the magnetic topology spontaneously self-organizes into a QSH state, in which the magnetic dynamics are dominated by the innermost resonant mode with $(m = 1, n = -7)$, as shown in the toroidal mode spectrum of a $1.5MA$ plasma reported in Figure 1.13. Inside the helical structure, the energy confinement is enhanced and electron temperatures exceeding $1keV$ have been measured with steep gradients, which identify an internal transport barrier [30]. This will be described more in detail in §1.3.1.

It should be highlighted that in these self-organized equilibria the $(1, -7)$ mode dynamics is intermittent and is reminiscent of the sawtooth activity of the tokamak $(1, 1)$ mode. This is due to magnetic relaxation events associated with an increase of the secondary modes [31]. Despite this intermittent behavior, as the plasma current increases, QSH states become progressively more persistent and purer. This experimental evidence has been quantified by calculating the so-called QSH persistency, defined as the ratio between the total time in the discharge spent in QSH divided by the current flat-top duration [32, 33]. High-current RFX-mod

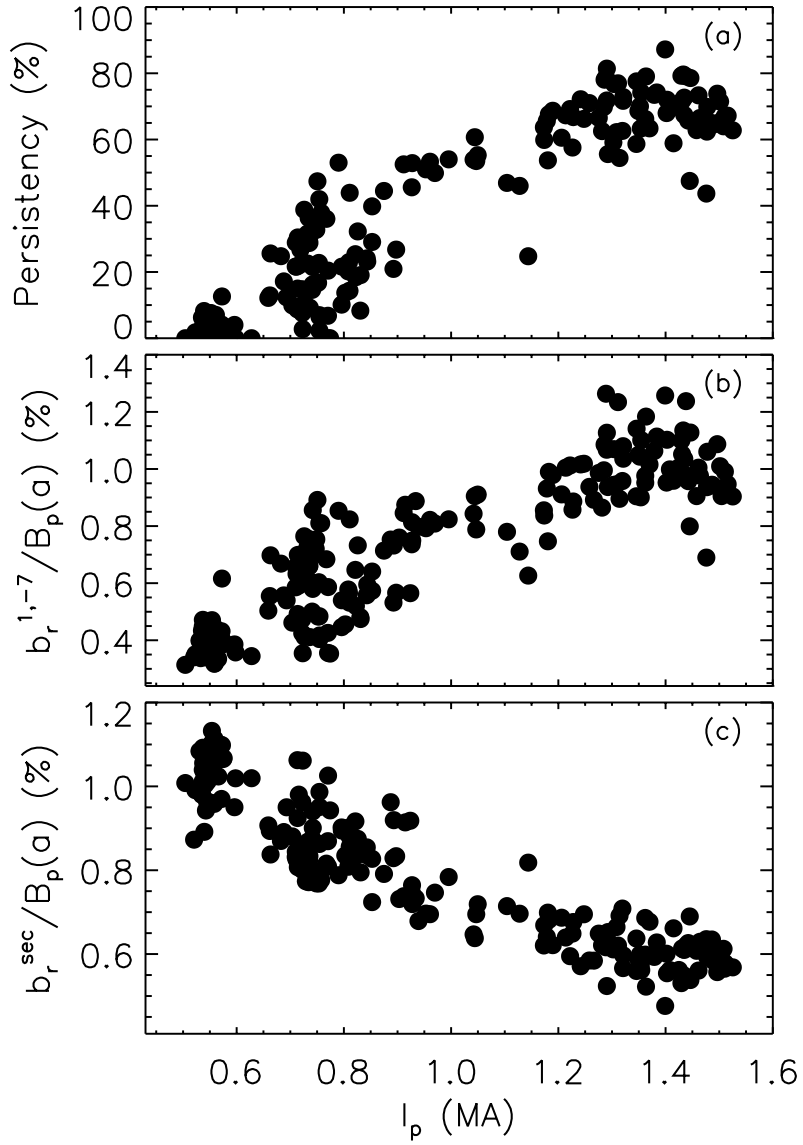

Figure 1.14: (a) QSH persistency, (b) normalized edge radial magnetic field amplitude of (b) the $(1,-7)$ mode and (c) of $m = 1$ secondary modes, for different levels of plasma current. These quantities are defined in the text.

plasmas are characterized by QSH phases that occupy a significant fraction of the discharge flat-top, up to 90%, as shown by the statistical analysis of the QSH persistency at different levels of plasma current reported in Figure 1.14(a). As the plasma current raises, the edge radial magnetic field amplitude of the $(1,-7)$ mode normalized to the poloidal magnetic field, $b_r^{m=1,n}/B_p(a)$, increases and the

secondary mode amplitude, $b_r^{sec}/B_p(a)$, calculated as

$$b_r^{sec}/B_p(a) = \sqrt{\sum_{m=1,n=-16}^{-8} b_r^{1,n}(a)^2}/B_p(a), \tag{1.33}$$

decreases. These two evidences are shown in Figures 1.14(b) and (c), respectively.

The exploration of high-plasma currents and thus the discovery of self-organized helical equilibria has been possible by controlling the edge radial magnetic field perturbations, produced by tearing modes and *error fields*, through an advanced magnetic feedback system, that will be described in detail in Chapter 2. Magnetic field errors may originate from several sources, such as axi-symmetric coil misalignments, coil feeds, 3D structures in the wall surrounding the plasma, presence of ferromagnetic materials near the plasma surface, and others [34]. In the following Section, the role of magnetic feedback control in high-performance operational scenarios will be summarized, with particular reference to the RFX-mod RFP [23] and the DIII-D tokamak [35], which are the two experiments in which the Thesis work has been carried out.

1.3 Active control of high-performance regimes in RFPs and tokamaks

As introduced in §1.1.1, an important goal of thermonuclear fusion research, and in particular of ITER, is to demonstrate steady-state operation. This requires to minimize or zero the inductively driven current, working in high-β conditions to maximize the bootstrap current fraction [36]. In these high-performance scenarios, plasmas with high pressure are likely to operate near one or more stability limits, thus the control of MHD instabilities and magnetic field errors is crucial.

In the last decades, advanced feedback control strategies have been developed in tokamaks and RFPs to mitigate or suppress MHD instabilities and several reactor-relevant results have been obtained [37]. In this Section, the role of magnetic feedback control on high-performance scenarios in the RFX-mod and the DIII-D experiments will be described. Both experiments are equipped with sets of sensors to detect magnetic field perturbations and with active coils to control the mode perturbations. The magnetic feedback systems available in these experiments are very flexible and allow to test different feedback control schemes.

1.3.1. Helical equilibria at high-plasma current in RFX-mod

RFX-mod is equipped with a state-of-the-art magnetic feedback system constituted by 192 active coils, fully covering the torus surface, and with respective 192 sensors that measure the B_r, B_ϕ, and B_θ magnetic field components [23]. Each

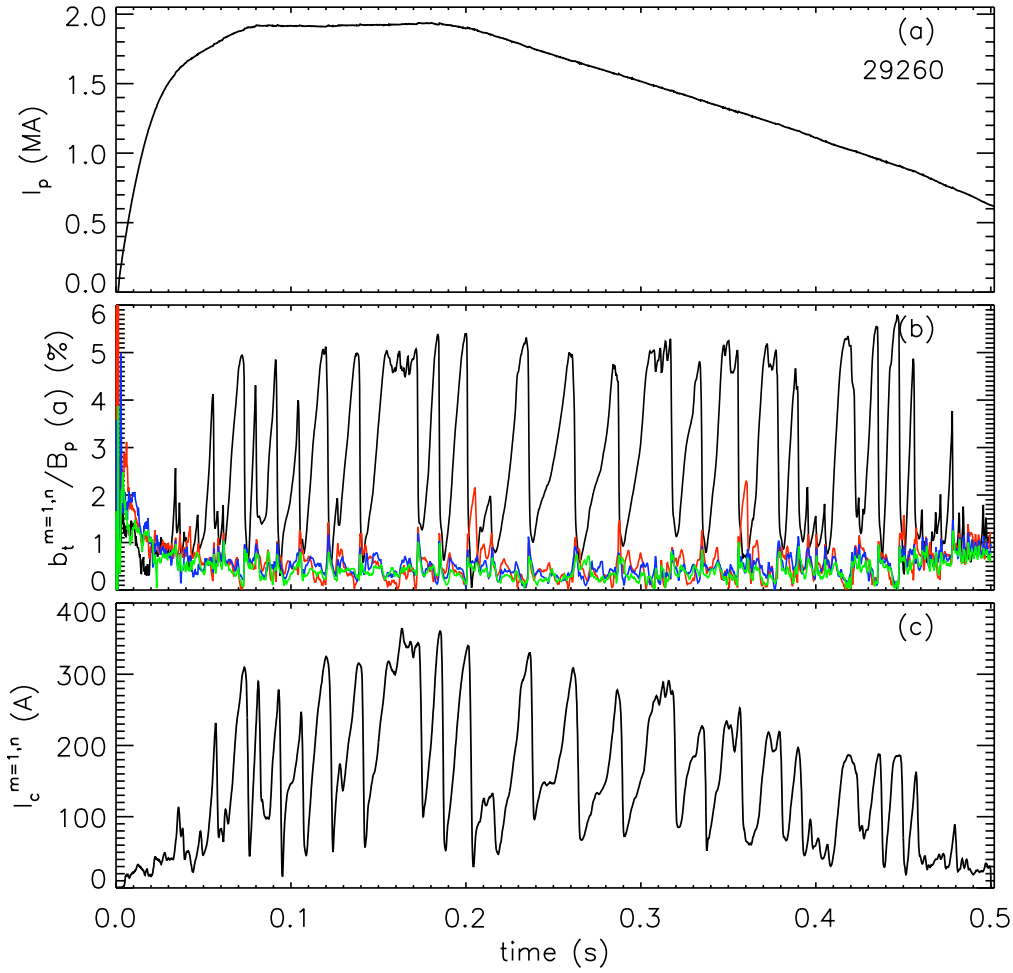

Figure 1.15: (a) Plasma current, (b) normalized edge radial magnetic field amplitude of the $(1,-7)$ mode (in black), $(1,-8)$ mode (in red), $(1,-9)$ mode (in blue), (c) coil current amplitude of the $(1,-7)$ mode in a $1.9MA$ discharge (29260).

active coil is independently driven by a digital controller, which allows great flexibility in the implementation of different feedback control algorithms, which will be described more in detail in Chapter 2.

The active control of magnetic field perturbations due to tearing modes and error fields allows for the exploration of high-plasma currents up to $2MA$ for the first time in a RFP configuration [24]. One of these experiments, realized in the 2010 experimental campaign, is shown in Figure 1.15. The plasma discharge lasts for about $0.52ms$ and the plasma current reaches $1.9MA$.

As described in §1.2.4, at high-plasma currents the $m = 1$ mode spectrum is characterized by the fact that the $(1,-7)$ mode dominates over the secondary

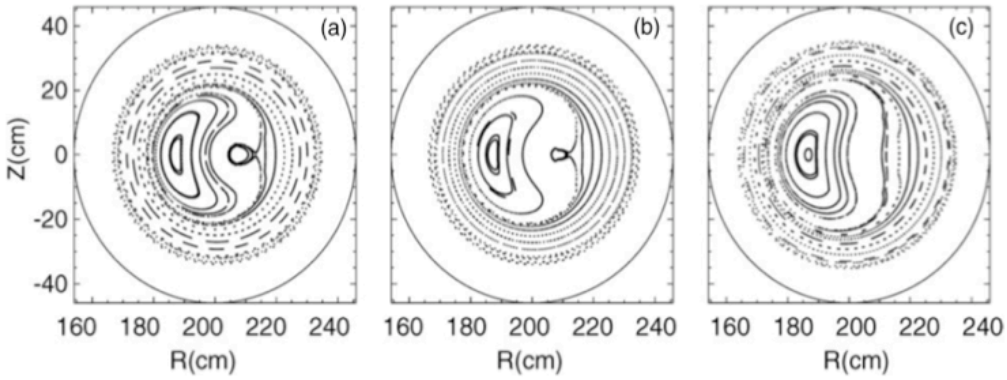

Figure 1.16: (a)-(c) Poloidal Poincaré plots of the magnetic field at increasing amplitude of then the $(1, -7)$ mode (3%, 4% and 5%, respectively) in the SH state. The cases analyzed have the same magnetic equilibrium and include the $(1, -7)$ mode only (this picture has been taken from [33]).

modes, as shown in Figure 1.15(b). The dominant mode repetitively grows and saturates to a value of about 5% of the normalized toroidal magnetic field, which exceeds the average amplitude of the secondary modes by a factor of 30. The coil current requested to control the magnetic field perturbations associated with the $(1, -7)$ mode at the edge is shown in Figure 1.15(c), and it amounts to about $300A$, near the current limit of the active coils of about $320A$.

The helical states spontaneously assessed at high-plasma current can be characterized by two different types of magnetic topology: in the first one a helical magnetic island is present and the plasma maintains its axisymmetric magnetic axis. In this case the helical structure is bounded by a magnetic separatrix, as shown by the Poincaré plot of the magnetic field in Figure 1.16(a). The Poincaré plot has been reconstructed in this case with the field line tracing code ORBIT [38, 39] and includes the $(1, -7)$ harmonic only. Above a threshold of the normalized $(1, -7)$ mode amplitude, $b_t^{1,-7}/B_p(a)$, of about 4%, the island X-point merges with the former axi-symmetric axis and the island O-point becomes the only helical axis of the configuration, as represented in Figure 1.16(c). This magnetic field configuration has been dubbed single-helical-axis state (SHAx) [40].

These two different magnetic topologies correspond to different electron temperature profiles, as shown in Figure 1.17 by Thomson scattering measurements. In QSH states with a magnetic island, named here QSH_i states, a large temperature peak is present near the island O-point and extends throughout the island width, corresponding to approximately 10% of the plasma volume, as shown in Figure 1.17(a). In SHAx states the hot region surrounded by the helical transport barrier is much broader than for the islands described above and can occupy up to 50% of the plasma volume, as shown in Figure 1.17(b).

The broadening of the hot helical region has a clear link with the magnetic

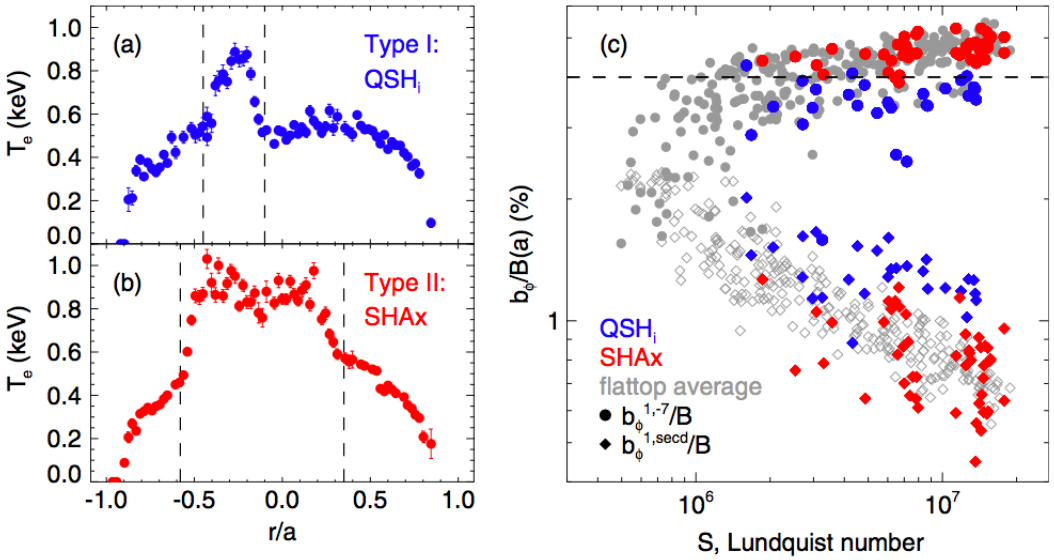

Figure 1.17: Electron temperature profiles measured by Thomson scattering during (a) a QSHi state, (shot 21982 at t =0.125s) and (b) a SHAx state, (shot 23962 at t =0.224s). (c) Relative amplitudes of the $(1, -7)$ mode (circles) and of the secondary modes (diamonds): flat-top average (grey) and instantaneous values, when Thomson scattering data are available, during QSHi (blue) and SHAx (red) (this picture has been taken from [33]).

topology. The normalized toroidal magnetic field amplitudes of the $(1, -7)$ mode and secondary modes, evaluated at the times when the Thomson scattering measurements are taken, are plotted in Figure 1.17(c) as a function of the Lundquist number, S, a dimensionless parameter expressed as the ration between the resistive diffusion time and the Alfvén time. S can be written in terms of measurable plasma quantities, as follows:

$$S = \tau_R/\tau_A = \frac{30 I_p T_e^{3/2}}{(0.4 + 0.6 Z_{eff}) \ln\Lambda \sqrt{m_i n_e}}, \tag{1.34}$$

where $I_p(kA)$ is the plasma current, $T_e(eV)$ and $n_e(10^{19} m^{-3})$ are the core electron temperature and density, Z_{eff} the effective ionic charge and m_i the proton mass. The Coulomb logarithm $\ln\Lambda$ in this case is fixed and amounts to 17.

The points plotted in Figure 1.17(c) corresponding to the two types of temperature profiles described above are marked with different colors. Blue circles refer to QSH_i states, while red circles to SHAX states. The hot region broadens as the normalized $(1, -7)$ mode amplitude exceeds a value of about 4%, above which the island separatrix is expected to disappear. In these cases also the secondary mode amplitude is lower.

The increased magnetic order obtained at high-plasma current has an impact

on the energy confinement, calculated as the ratio of the total thermal content and the Ohmic input power, $\tau_E = W_{th}/P_\Omega$. In SHAX states τ_E is doubled with respect to the QSH_i states [33]. The energy confinement improvement in SHAx states is due both to a decrease in the secondary mode amplitude, which reduces the overall level of magnetic chaos in the core, and to the saturation of the normalized $(1, -7)$ mode amplitude above 4%, which determines the broadening of the helical good-confinement region.

The observation of this new self-organized helical equilibrium in high-current plasmas is an important step towards the SH state predicted by MHD simulations, in which the configuration is sustained by a global and chaos-free helical deformation of the plasma [41]. Moreover, the plasma self-organization can be exploited to attain high-performance regimes in a fusion device, and provides a robust base for future experiments at event higher current.

To further improve the plasma performance in high-plasma current experiments, in this Thesis work, an optimization of the tearing mode and error field control has been performed [42, 43] and the main results will be described in Chapters 3 and 4. Recent experiments have shown that the helical equilibria, which spontaneously develop in high-plasma currents, can be induced by imposing proper helical boundary conditions through magnetic feedback [44]. The main findings and the approaches used to optimize these helical states will be discussed in Chapters 5 and 6 [45].

1.3.2. Active control of high-β plasmas in the DIII-D tokamak

In advanced tokamak scenarios, operation with high values of β requires the stabilization of the external kink mode [16]. As discussed in §1.2.2, an ideal wall placed close to the plasma can provide the required stabilization. However, in presence of a real wall, which has a finite conductivity, the external kink mode is not completely stabilized, but it is converted to a RWM.

Research carried out on the DIII-D tokamak and other tokamaks has demonstrated that the RWM can be stabilized either by plasma toroidal rotation [46, 47, 48, 49, 50] or by active feedback using magnetic coils [51, 52, 53, 54, 55, 56]. Two well known examples of the application of these techniques in high-β experiments in DIII-D will be described in the following.

Experiments showed initially that passive RWM stabilization relies on rapid plasma rotation, at a frequency of a few percent of the Alfvén frequency. The idea is that the RWM interacts with plasma rotation, since its growth rate and toroidal rotation frequency are limited to about τ_w^{-1}, which is usually much slower than the toroidal plasma rotation frequency, leading to a significant differential rotation between the plasma and the quasi-static magnetic perturbation. It has been shown that plasma rotation in conjunction with a dissipative term in the ideal MHD equations can stabilize the RWM [57].

1.3. Active control of high-performance regimes in RFPs and tokamaks

The existence of a critical rotation frequency Ω_{crit} for passive RWM stabilization has been originally demonstrated by a series of DIII-D experiments in which the rotation rate was modified through magnetic braking applied by an external magnetic perturbation. As the braking magnetic field was increased, the plasma decelerated more rapidly and the onset of the RWM occurred earlier, corresponding to a fixed value of the rotation [58]. First experiments suggested that the critical rotation frequency, evaluated at the $q = 2$ surface, above which the RWM is destabilized was $\Omega_{crit}\tau_A \approx 1 - 2\%$ [59, 60, 61, 62].

More recent experiments using near-balanced neutral beam injection revealed that a RWM can be stabilized even at toroidal rotation frequencies of the order of $\Omega_{crit}\tau_A \approx 0.3\%$ at the $q = 2$ surface. An example of these low-rotation experiments, taken from [63], is shown in Figure 1.18. In this discharge, as the rotation is slowly

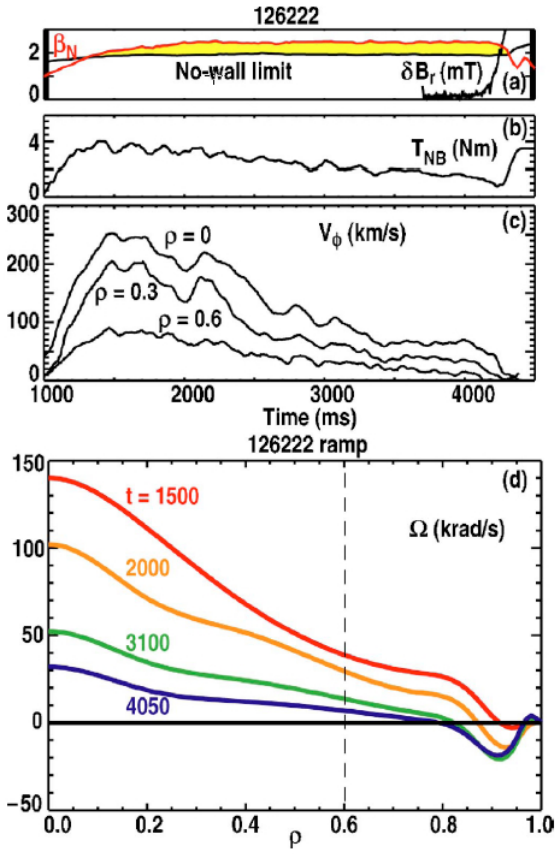

Figure 1.18: Time evolution of a discharge with diminishing neutral beam torque. (a)-(c) Time histories, including (a) normalized β, estimated no-wall stability limit, and amplitude δB_r of the non-rotating $n = 1$ RWM; (b) neutral beam torque; and (c) toroidal rotation velocity at several values of normalized radius r/a. (d) Radial profiles of the measured rotation frequency at several times during the discharge (this Figure has been taken from [63]).

reduced by properly programming the beams, the normalized beta is maintained at about 30% above the no-wall stability limit $\beta_N^{no-wall}$, which is the β_N limit predicted without the stabilizing effect of the wall. The plasma remains stable until the rotation at the $q = 2$ surface reaches about $15km/s$, corresponding to only $\Omega_{crit}\tau_A \approx 0.3\%$. At this time instant, as shown in Figure 1.18(a), a RWM grows.

The main difference with previous experiments is that the plasma rotation was reduced by decreasing the neutral beam torque as shown in Figure 1.18(b), removing the need to use non-axisymmetric magnetic fields to slow down the plasma rotation. In fact, the resonant interaction of externally applied fields with the RWM leads to strong braking of the plasma rotation, since the non-axisymmetric field is amplified by the plasma response. In addition, changing the neutral beam torque can result in rather different shape of the rotation profile, with negative rotation developing near the edge, as the positive core rotation decreases, as shown in Figure 1.18(d) for different time instants. The edge negative rotation could have a significant stabilizing effect. Similar low critical rotation values have been observed also in experiments carried out in the JT-60U tokamak with reduced neutral beam torque and reduced magnetic field errors [64].

However, burning plasma experiments, such as ITER, are expected to rotate rather slowly [65]. For this reason, active feedback control of RWMs is recognized as important for future tokamak operations. In particular, the development of active control techniques able to cope with different MHD instabilities is essential to perform reactor-relevant plasmas. In advanced tokamak operations, a stable RWM can in fact be non-linearly excited by fast MHD instabilities [56] . Typical examples are RWMs driven by edge-localized modes (ELM) or by off-axis fishbones. In the following, the synergetic action of active coils both external (so-called C-coils) and internal (I-coils) to the vacuum vessel to suppress RWMs driven by these fast MHD events in DIII-D will be investigated.

The experiment in Figure 1.19 on the left, taken from [56], represents a high-β plasma characterized by the onset of a series of ELMs, as shown in the D_α emission measurement in Figure 1.19(e). The time traces of the feedback coil currents reported in Figures 1.19(c) and (d) indicate that the feedback is provided in this case by the internal coils only. At each ELM event, a RWM is excited and the feedback reacts to reduce the mode amplitude and is successful in holding the $n = 1$ poloidal magnetic field amplitude down to about $2 - 3G$ with a coil current that amounts to few hundred Amperes up to $t = 1550ms$. Even though the mode amplitude is almost constant, the requested coil current increases slowly in time up to the point that the mode amplitude reaches more than $5G$, leading to the saturation of the I-coil current.

The slow increase in the I-coil current is probably a response to a small uncorrected error field. This static uncorrected error field itself should remain constant on this timescale of about $300ms$, however the error field evolves in time when

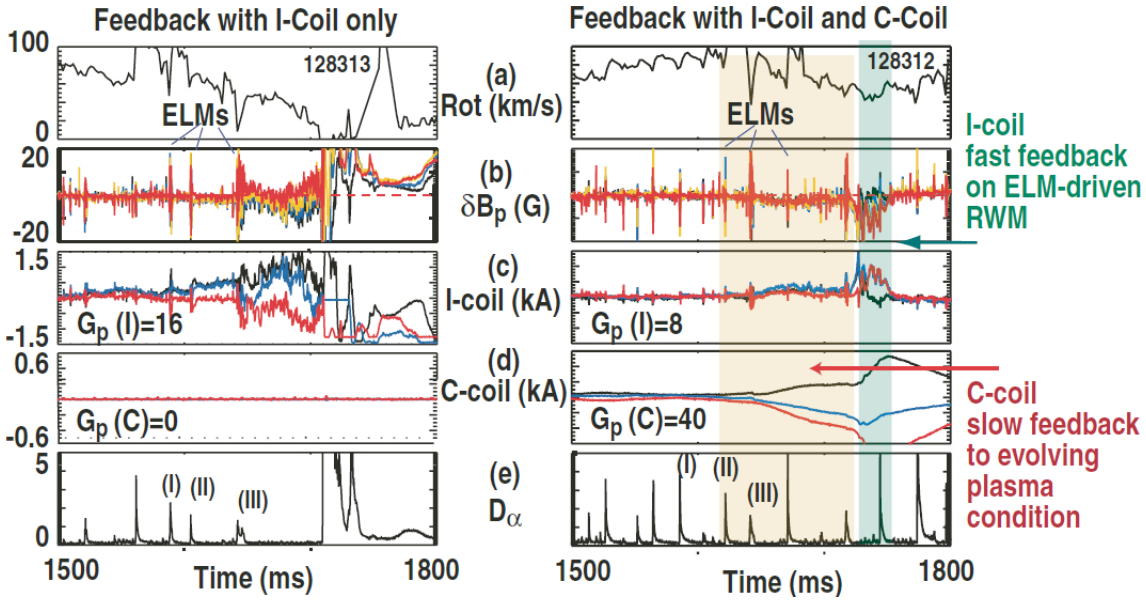

Figure 1.19: β_N collapse with frequent ELMs with I-coil only and I and C-coil feedback. Left column: feedback with I-coil-only suppressed the RWM for a few ELMs. Right column: simultaneous operation with both the I-coil (fast feedback) and C-coil (slow feedback) reduced the accumulation of RWM amplitude. (a) Plasma rotation at $q \approx 2$, (b) δB_p magnetic sensor signals (c) I-coil currents, (d) C-coil currents and (e) D_α(au) (this picture has been taken from [56]).

the plasma approaches the marginally unstable condition, which occurred around $t = 1730 - 1740ms$. This experiment demonstrates that successful feedback operation, in high-β regimes and in the presence of fast MHD activity, requires not only direct control of unstable RWMs but also careful control of residual oscillations resulting from the pile-up of ELM-driven RWMs.

A good recipe to improve the feedback control in this experiment is to separate the control process into two parts: one using internal I-coils for fast MHD-driven RWM control and the other using external C-coils for the slow control of the error fields. This feedback approach has been tested in the experiment shown in Figure 1.19 on the right and allows to reduce the onset of β_N collapses due to the ELM-driven RWM. The slow increase in the C-coil currents shown in Figure 1.19(d) replaces the slow rise seen previously in the I-coil current. With two feedback systems energized simultaneously, the I-coil responds to the ELM-driven RWM on a fast time scale and the required current is reduced to $100 - 200A$, while in the other experiment the I-coil current is above $1kA$, since the feedback tries to reduce also the uncorrected error field.

The application of simultaneous fast and slow feedback reveals to be a powerful strategy to cope with RWMs driven by fast MHD events, as in the case described

above, and slowly growing error fields that can be amplified by the resonant field amplification (RFA) mechanism at high-β [60], causing the beta-collapse. The RFA phenomenon has been observed for the first time in DIII-D and reveals that if an external error field has components and frequency that can resonate with a plasma instability, such as a RWM, the plasma response can become very large. In other words, RFA enhances the effect of error fields on the plasma. Therefore, it is crucial to compensate the error field component to make sure it is minimized and reduced to a level at which the plasma response is kept below the noise level.

The presence of uncompensated error fields in DIII-D Ohmic and high-β plasmas has been investigated during this Thesis work, in the framework of a collaboration between the RFX-mod and DIII-D teams. Based on the analyses which will be described in Chapter 7 [45, 66], a possible source of error field is introduced by the algorithm used in DIII-D for the compensation of the magnetic field measurements. In the DIII-D feedback logic, the quantity the feedback reacts to is the so-called plasma response, which is obtained by subtracting from the magnetic field measurements the magnetic fields external to the plasma, for instance those induced by the feedback and axi-symmentric coil currents. This algorithm computes only the static components of these external fields. In this way, the dynamic response of the wall to any time-varying external magnetic field is neglected.

The analyses of Ohmic and high-β experiments suggest that, if the frequency-dependent or AC effects introduced by the response of the wall are not taken into account in the signal compensation algorithm, they can introduce error fields. These error fields can further destabilized RWMs or be amplified through a RFA effect, especially at high-β, where the plasma is less resilient to uncompensated error fields.

CHAPTER 2

RFX-mod and DIII-D: description of the machines and of their magnetic feedback systems

This Chapter will be dedicated to the description of the two devices, where most of this Thesis work was performed, and of their magnetic feedback systems for the control of MHD modes and error fields: the RFX-mod reversed-field pinch and the DIII-D tokamak. The active control strategies and the techniques that were important for the work discussed in this Thesis will be presented.

2.1 The RFX-mod experiment

The Reversed Field eXperiment-mod (RFX-mod) is based in Padova, Italy, and is the largest RFP experiment in the world, with aspect ratio $R_0/a = 2m/0.457m \simeq 4.4$, where R_0 and a are the major and the minor radius, respectively [23]. RFX-mod can operate at high-plasma current, up to 2MA, a record high value for a RFP experiment [24]. A picture of this experiment is shown in Figure 2.1. The main machine components are described in the following.

- **Vacuum vessel**: this is the toroidal chamber containing the plasma. It is an all-welded, rigid structure made of INCONEL 625, composed of 72 elements welded together. The vacuum vessel is also an interface between the plasma and the outside. It is equipped with 96 ports for gas inputs, vacuum pumping and diagnostic systems. In the scheme reported in Figure 2.2, the vacuum vessel is plotted in white.

- **First wall**: this is the inner side of the vacuum vessel, exposed to the plasma. It is composed of 2016 graphite tiles that cover completely the inner part of the vacuum vessel and can be baked at temperatures between $350 - 400°C$. Graphite was chosen because it is a low-Z material to lower the plasma Z_{eff} value.

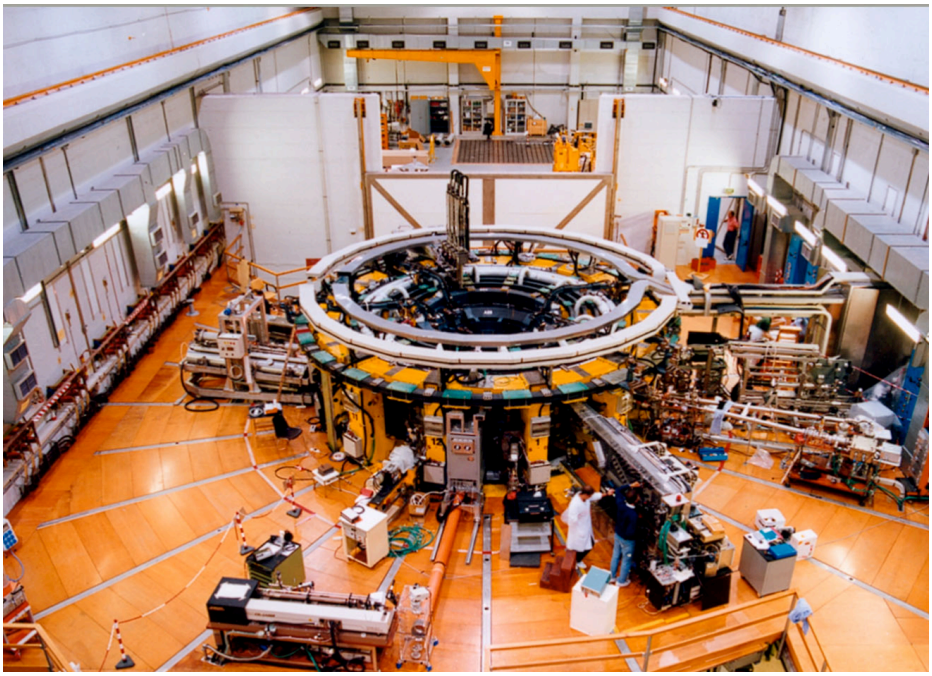

Figure 2.1: A picture of the RFX-mod experiment.

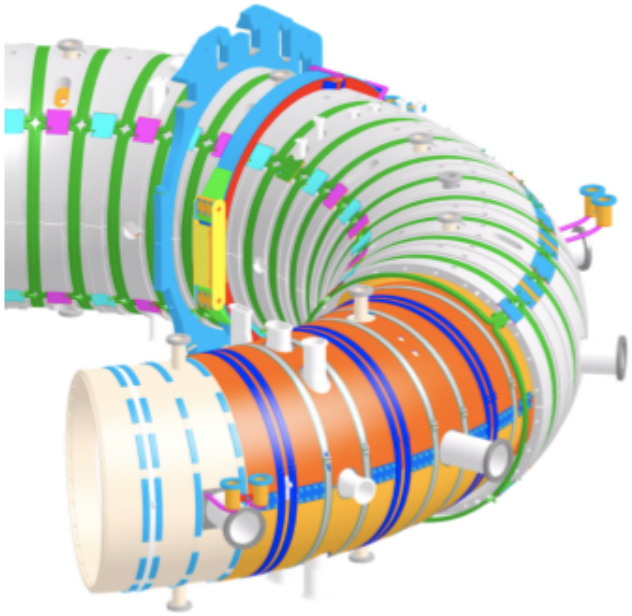

Figure 2.2: Scheme of the RFX-mod assembly: the shell is plotted in orange, the vacuum vessel in white, the active coils in green. Note the presence of portholes for diagnostic accesses.

- **Stabilizing shell**: this has the purpose of providing passive stabilization of the fast MHD instabilities. It is not uniform neither in the poloidal direction, as an inner equatorial cut is present, nor in the toroidal direction, as a poloidal gap and a region where the two edges of the shell toroidally overlap are also present, respectively at the toroidal positions $\phi = 112.5°$ and $\phi = 292.5°$. The two gaps in the shell allow for the penetration of the axi-symmetric toroidal magnetic field and of the axi-symmetric toroidal electric field. In the scheme plotted in Figure 2.2, the copper shell is plotted in orange, while the stainless steel supporting structure, which lays outside the shell and sustains it, is shown in grey.

- **Magnetizing coils**: they provide the time-varying poloidal magnetic flux that induces the plasma current during the discharge. The 40 magnetizing windings can carry a maximum current of $50kA$ and produce a $15Wb$ maximum flux. No iron core has been adopted, even though it would have reduced the coil dimensions, power demand and costs, in order to avoid magnetic field asymmetries and improve the accessibility.

- **Toroidal coils**: the toroidal field winding system consists of 48 coils uniformly distributed along the toroidal direction, that surround the vessel and

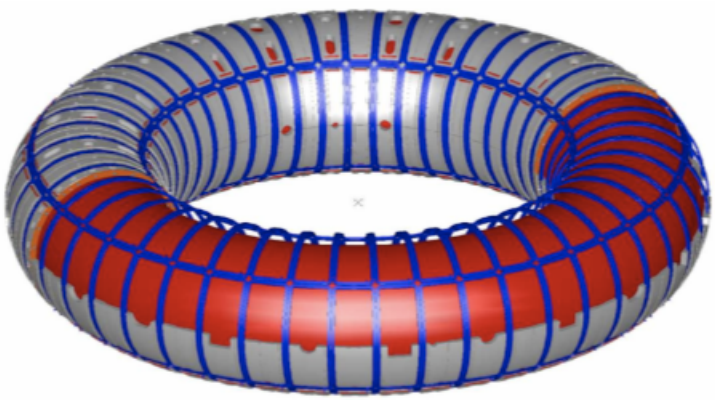

Figure 2.3: Scheme of the RFX-mod active control system: 192 active coils (in blue), located external vacuum vessel (in grey), which fully cover the torus surface.

the shell. They are designed to generate the toroidal magnetic field needed to set-up and maintain the discharge. The coils are series-connected in 12 groups of 4: each group is connected to an independently controlled power supply unit. During normal operations, the toroidal coils produce a maximum toroidal bias field $B_\phi = 0.7T$ at the beginning of the discharge and a maximum reversed field at the wall $B_\phi(a) = 0.44T$ during the plasma current flat-top.

- **Field shaping coils**: this set of 16 poloidal coils is designed to generate a vertical field aimed at feedback controlling the position of the plasma column with respect to the vessel during the discharge.

- **Active control system**: it is the most distinct characteristic of the RFX-mod experiment. It is made up of 192 active saddle coils, shown in blue in Figure 2.3, distributed in 48 toroidal and 4 poloidal positions; they extend 90° poloidally and 7.5° toroidally and fully cover the torus. The coils lay on the external surface of the support structure, while on its internal surface 192 radial field sensors are located, covering the same solid angle of the active coils, and also 192 pick-up probes are present, which measure the toroidal magnetic field in the middle of each saddle coil. For their shape and position, the saddle coils can produce a relatively strong local magnetic field with a substantial radial component. They are designed to carry a maximum current of $400A$ for $300ms$, producing a maximum local radial field of about $50mT$. An integrated digital feedback system controls the toroidal and poloidal circuits, the toroidal equilibrium, and the 192 saddle coils.

  Each of the 192 active coil is independently fed by a power supply, which

is digitally controlled by a set of dedicated CPUs that can process 192 sensor inputs and generate 192 reference outputs at a rate of $\approx 2 - 5kHz$. A Proportional Integral Derivative (PID) digital controller allows a great flexibility in the implementation of different feedback schemes, for example, in the so-called *virtual shell* (VS) algorithm [67] the coils cancel the magnetic flux linked to it, and the feedback gains are applied to the coil power supplies. Instead, in the *clean mode control* (CMC) scheme [68, 32] the feedback variables to be controlled are the helical mode amplitudes and phases. These feedback schemes will be described more in detail in the next Section.

2.2 Magnetic feedback schemes tested in RFX-mod

In RFX-mod, MHD instabilities and magnetic field errors are real-time controlled using the magnetic feedback system described above. The encouraging progress obtained in this field in the last years allows for the exploration of high-plasma current regimes, up to $2MA$, for the first time in a RFP, as described in Chapter 1. In the following a description of magnetic feedback control schemes tested in RFX-mod will be presented.

The VS scheme The first control scheme implemented in the RFX-mod feedback logic is a VS algorithm similar to that proposed by Bishop in [67]. The VS relies on a grid of active coils counteracting in a feedback scheme the radial field measured by an identical grid of radial field sensor loops. In this way, in principle it is possible to zero the flux measured by each sensor loop, as an ideal conducting wall would do, hence the name virtual shell. In RFX-mod, the VS algorithm determines the currents flowing into the 192 active coils in order to keep the measurements of the corresponding 192 radial magnetic field sensors at the plasma edge as close as possible to zero.

The VS allowed to obtain good results in terms of RWM stabilization and tearing mode control. Full feedback stabilization of single and multiple RWMs has been demonstrated [69]. These findings confirm and extend the results obtained on the Extrap-T2R RFP experiment [70]. On the other hand, tearing modes can not be suppressed even with an ideal feedback system, which perfectly cancels the edge radial magnetic field. Nevertheless, it is crucial to reduce their edge radial magnetic field amplitude since it causes $m = 1$ non-axisymmetric distortions of the last closed flux surface (LCFS), δ_1, defined here through the formula $b_r = B_0 \cdot \nabla \delta_1$, where b_r and B_0 are respectively the perturbed radial magnetic field and the equilibrium magnetic field at the plasma edge [71]. A large non-axisymmetric distortion can cause strong plasma-wall interaction. If multiple modes are phase-locked together, the δ_1 non-axisymmetric distortion can be localized in limited areas of the wall. This can pose severe limits to high-current operations if not properly controlled.

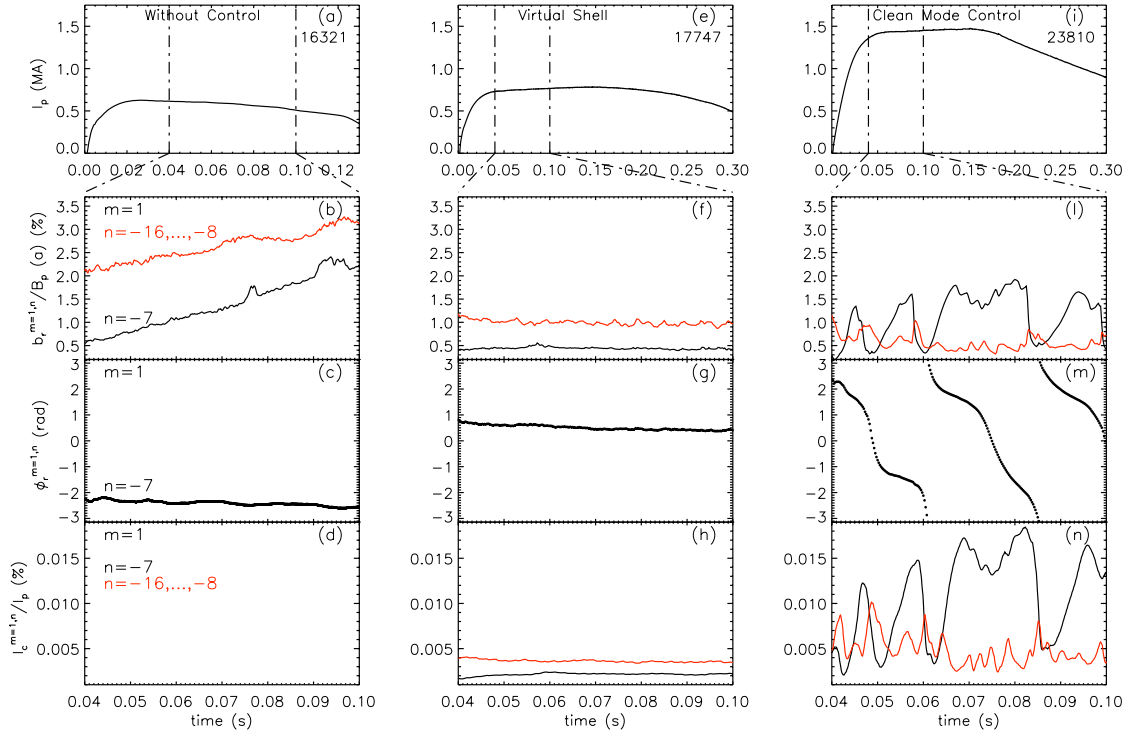

Figure 2.4: Plasma waveforms for a typical discharge without active control (left hand side), with VS (center) and CMC (right hand side): (a-e-i) plasma current, (b-f-l) normalized edge radial magnetic field amplitude of the $(1,-7)$ (black) and secondary $m=1$ modes (red), (c-g-m) $(1,-7)$ mode phase, and (d-h-n) feedback coil current amplitude of the $(1,-7)$ (black) and of the $m=1$ secondary modes (red).

The VS is able to reduce the tearing mode radial magnetic field amplitude with respect to the case without feedback control. This is highlighted in Figure 2.4. In this Figure, on the left, a plasma experiment in which only the copper shell provides passive stabilization of MHD modes, is represented. The record plasma current obtained in this configuration in RFX-mod is $0.7MA$ and the plasma lasts up to $120ms$, as show in Figure 2.4(a). The radial magnetic field amplitude of the tearing modes at the plasma edge grows continuously during the discharge, as shown in Figure 2.4(b), where the normalized edge radial magnetic field amplitude of the $(1,-7)$ mode is shown in black, while the red trace represents the total amplitude of the secondary modes, calculated with the Equation (1.33).

The experiments without active control, as mentioned before, are limited by strong plasma-wall interaction, which is affected by wall-locking and phase-locking of multiple tearing modes. An example is reported in Figure 2.5(a), where the edge radial magnetic field pattern is shown as a function of the toroidal angle and time.

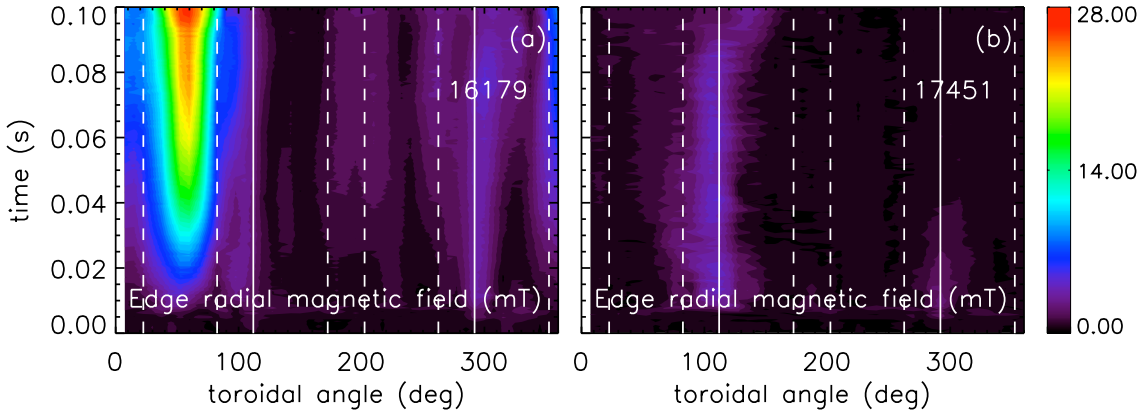

Figure 2.5: Radial magnetic field perturbation at the sensors as a function of toroidal angle and time (a) without magnetic feedback control and (b) with the VS scheme. The experiments represent the 16179 and 17451 discharges.

Early in the discharge a toroidally-localized deformation, due to tearing-mode phase-locking, sets in and grows to very large amplitudes. This phenomenon can cause strong, localized power deposition, associated to parallel transport along field lines directly striking the first wall.

The application of active control, using the VS scheme, allows to reduce the radial magnetic field at the edge due to tearing modes. As shown in Figure 2.4(f), the normalized edge radial magnetic field amplitude of the $(1, -7)$ mode and the secondary modes is significantly reduced, by more than 50%, with respect to the experiment without active feedback. The reduction of magnetic field perturbations due to tearing modes at the plasma edge produces a smoother flux surface at the plasma edge, as reported in Figure 2.5(b).

The application of active control produces remarkable effects on the plasma performance. A 3-fold increase in pulse length and well controlled $300ms$ pulses are routinely obtained at $0.8MA$ plasma current. Often, the mode dynamics is dominated by the $(1, -7)$ mode, and the QSH state, described in Chapter 1, has thus been observed, for example, with soft-x ray tomographic measurements. The maximum electron temperature, measured by the Thomson scattering diagnostic, doubles, with radial profiles significantly steeper with respect to the case without feedback [72]. The energy confinement time of RFX-mod is 50% higher than without feedback control [74]. On a statistical basis, a good correlation between high energy confinement times and low radial magnetic field amplitudes of $m = 1$ secondary modes is found [33, 73].

The mode control. After an initial period of operations with VS, it was realized that an intrinsic limitation did not allow for further improvements of the plasma performance. The origin of the problem is the aliasing of the sideband harmonics generated by the discrete coil system, coupled with coils with the same periodicity.

Of course, the DFT harmonics correspond to Fourier harmonics only if the aliasing phenomenon does not occur. This condition is not satisfied when the feedback coils are active, since they produce sidebands not resolved by the sensors. This condition is satisfied for the spectrum of MHD modes in RFX-mod, but it is not true when the saddle coils generate a field. In fact, a regular grid of MxN saddle coils covering a torus, such as in RFX-mod where M=48, N=4, can produce magnetic fields with helicities up to $m = M/2$ and $|n| = N/2$ together with an infinite number of sideband harmonics. When the active coils induce magnetic fields, the aliasing of sideband harmonics pollutes the DFT spectrum. Therefore, the perfect cancellation of the radial magnetic flux does not correspond to the cancellation of the instability harmonics at the sensor radius.

To overcome this systematic error, an algorithm that computes and subtracts the aliased sidebands from the measurements has been implemented in real-time. The sidebands are estimated from the feedback coil currents, using a cylindrical model of the active coils. The "cleaned" harmonics obtained in this way are used as the feedback variable of a new control scheme, named clean mode control (CMC) [32, 68]. The real-time implementation of the CMC algorithm implied a significant upgrade of the control system, since the real-time acquisition of 48×4 coil currents was required.

In the CMC scheme, the coil current acting on the (m, n) harmonic, $I_c^{m,n}(t)$, is determined through a PID feedback law:

$$I_c^{m,n}(t) = K_p^{m,n} b_r^{m,n}(t) + K_i^{m,n} \int_0^t dt' b_r^{m,n}(t') + K_d^{m,n} \frac{db_r^{m,n}(t)}{dt}, \qquad (2.1)$$

where $b_r^{m,n}$ is a complex cleaned Fourier harmonic. The feedback action is applied to cancel independently each harmonic, extrapolated at the plasma wall radius [68]. The actual reference value for each active coil is then obtained by performing, at each control cycle, a real-time inverse Fourier transform of the $I_c^{m,n}(t)$ current references. Before this Thesis work, an empirical approach, which will be described in detail in Chapter 3, was used to choose the feedback parameters of the mode controller, i.e. the PID gains.

The main differences among the VS and the CMC schemes is on tearing mode rotation and radial magnetic field amplitude at the plasma edge. Regarding the first point, while the $m = 1$ modes are always locked with the VS, they slowly rotate with the CMC, with an angular frequency in the range $10 - 100 Hz$, depending on the choice of the feedback gain.

A statistical distribution of the $(1, -7)$ mode angular frequency is shown in Figure 2.6 for an ensemble of similar VS (red) and CMC (black) discharges. The plasma current has been selected in the range $I_p \in [0.4, 0.9] MA$, the reversal

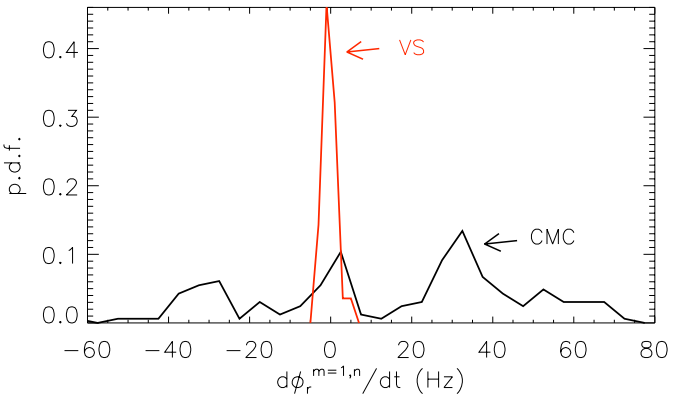

Figure 2.6: Probability distribution function of the $(1, -7)$ mode angular frequency for a database of VS (red) and CMC (black) discharges. With VS the mode is locked, while with CMC it rotates both with positive and negative angular frequencies.

parameter F, defined in Equation (1.29), $F \in [-0.045, -0.030]$, while the ratio between the electron density and the Greenwald density, $n/n_G \equiv n/(I_p/\pi a^2) \in [0.05, 0.26]$. With VS, the angular frequency is always very close to zero, while in the empirically-optimized CMC discharges it peaks around $\pm 30Hz$, using a proportional gain $K_p = 800$.

The removal of the systematic error due to the sideband aliasing allowed to improve significantly the control of the magnetic boundary. This is highlighted in Figure 2.7(a), where a statistical analysis of the flat-top averages of the total normalized edge radial magnetic field amplitude due to tearing modes $b_r^{tot}/B_p(a)$, defined as:

$$b_r^{tot} = \sqrt{\sum_{m=1,n=-16}^{-7} b_r^{1,n}(a)^2}/B_p(a), \tag{2.2}$$

is reported for various levels of plasma current. The discharges considered here have similar magnetic equilibrium and density: $F \in [-0.08, -0.036]$, $n/n_G \in [0.06, 0.22]$). The CMC scheme keeps the edge amplitudes to a lower level, of about 30% with respect to the VS scheme, and simultaneously induces tearing mode rotations. These effects allow a reduction of the maximum $m = 1$ non-axisymmetric distortion of the LCFS, at present to values as low as $0.9cm$, as shown in Figure 2.7(b).

To quantify the phase-locking among multiple tearing modes, the locking strength parameter LS has been calculated. LS represents, on a scale from 0 to 1, the degree of constructive interference of an ensemble of modes and it is defined as the normalized sum over $m = 1, n = -16, .., -8$ of the cosine of mode phase differences, $LS \propto \sum_{m=1,n1,n2=n_{min}}^{n_{max}} cos(\phi_r^{m=1,n1} - \phi_r^{m=1,n2})$ [75]. The LS of CMC discharges is

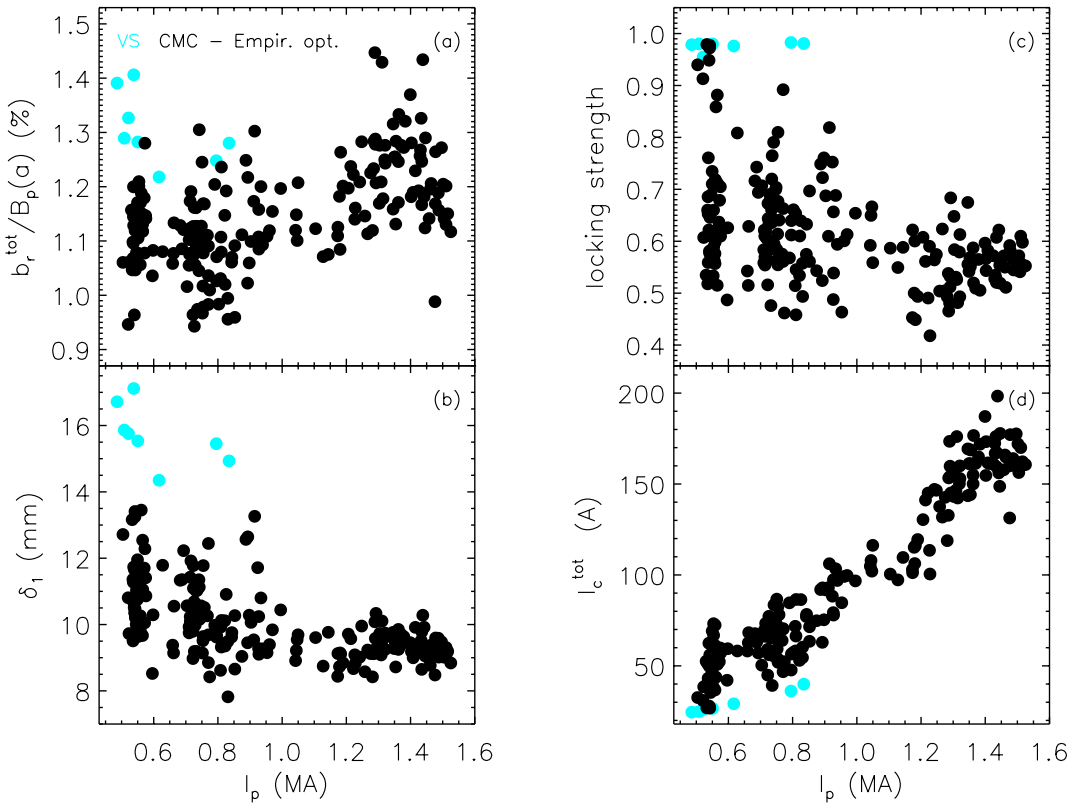

Figure 2.7: (a) Total edge radial magnetic field amplitude, (b) non-axisymmetric $m = 1$ distortion of the LCFS, (c) locking strength, and (d) total coil current amplitude for discharges with different plasma current. VS discharges (cyan dots) are compared with the CMC (black dots) discharges.

significantly lower than that of the VS ones. Moreover, the LS decreases with the plasma current, as shown in 2.7(c).

The improvements on tearing mode control highlighted above have been obtained with a higher request of coil current, quantified by:

$$I_c^{tot} = \sqrt{\sum_{m=1,n=-16}^{-7} (I_{coil}^{1,n})^2}, \tag{2.3}$$

where $I_{coil}^{1,n}$ is the feedback coil current on each $(m = 1, n)$ harmonic. This is shown in Figure 2.7(d).

As the wall-locking is partially broken, the plasma-wall interaction is more spread over the first wall. This allows for the exploration of high-plasma current regimes up to $2MA$, which was not possible in the VS scheme, due to the tearing mode wall-locking and subsequent plasma-wall interaction.

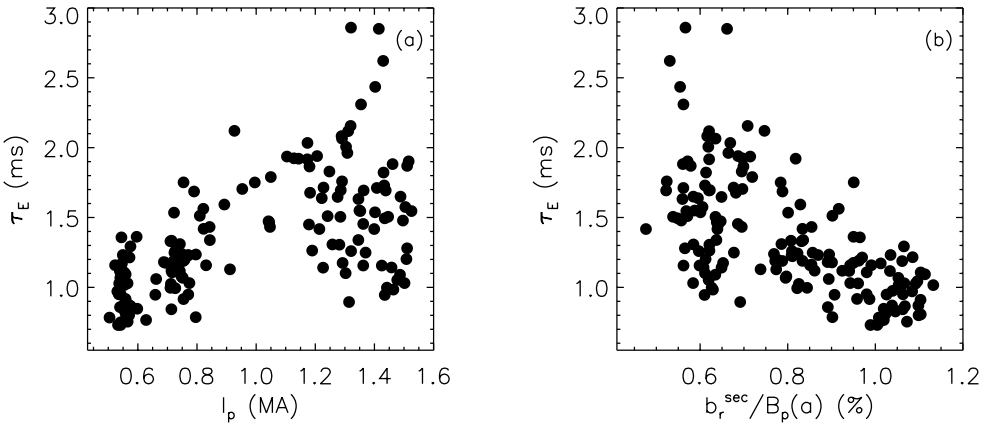

Figure 2.8: Flat-top averages of the total energy confinement time as a function of (a) plasma current and of (b) normalized radial magnetic field amplitude of secondary modes, calculated as defined in Equation (1.33).

As discussed in Chapter 1, as the plasma current is increased, the QSH states become more frequent and purer. In these states, a strong improvement of the energy confinement is found within the helical structure. The fact that the $(1, -7)$ mode does not contribute to the magnetic field stochasticity, which is affected only by the residual secondary modes, provides the possibility of getting good confinement. This aspect is highlighted by a statistical analysis of the flat-top averaged total energy confinement time τ_E, reported in Figure 2.8(a), as a function of plasma current. Best τ_E values at low-plasma current, in the range $I_p \in [0.4 - 0.8]MA$, amount to about $1ms$, and increase up to about $3ms$ in QSH states. The energy confinement improvement in QSH is due to a decrease in the secondary mode amplitude, which reduces the overall level of magnetic chaos in the core, as shown in Figure 2.8(b).

A further improvement of the total energy confinement time has been obtained in high-performance RFP scenarios, as described in Chapter 1, characterized by the presence of QSH states with a single helical axis (SHAx) [40]. SHAx states were, in fact, shown to be much more resilient to magnetic chaos than QSH states including a magnetic island [33].

2.3 The DIII-D experiment

The DIII-D tokamak is operated by General Atomics, San Diego, CA, USA. The "D" suffix in the name refers to the D-shaped cross-section of the vacuum vessel, having a major radius of $1.66m$ and a minor radius of $0.67m$. Figure 2.9 shows a cross-section of DIII-D with contours of constant magnetic flux shown to illustrate

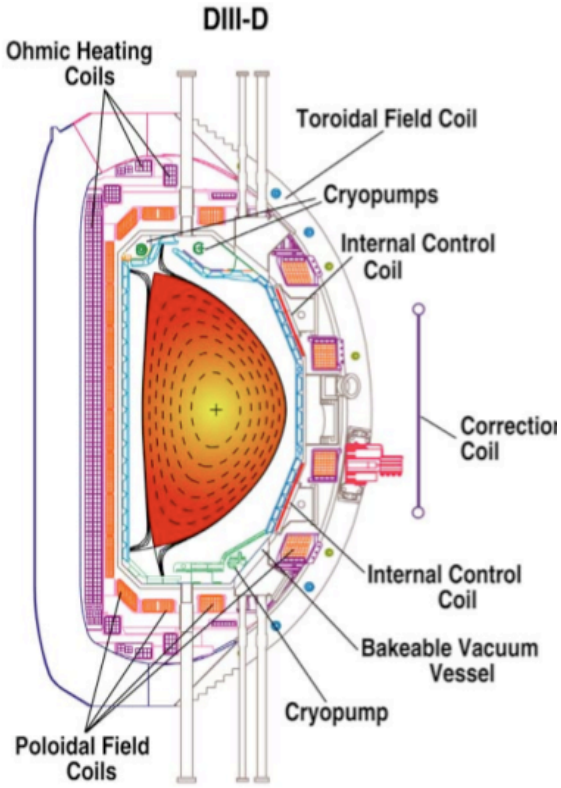

Figure 2.9: Cross-section of DIII-D tokamak.

a typical plasma shape.

DIII-D is approximately one-fourth the size of ITER and produces plasmas with ITER-relevant temperatures, collisionality, and normalized pressure (or beta). Because of these similarities in physics regimes and control capabilities, DIII-D can provide significant information for the design and operation of ITER.

The main DIII-D components are described in the following.

- **Vacuum vessel**: the graphite tiles cover more than 90% of the interior plasma-facing surface. The tiles absorb heat during the discharge and are cooled by water channels in the vessel wall in the period between discharges. In the high heat flux areas of the upper and lower divertor regions and centerpost the edge-to-edge tile misalignments and the tile gaps are less than $0.25mm$, to reduce erosion and provide axi-symmetry.

- **Ohmic heating coil**: the Ohmic heating coil (named E-coil) solenoid, plotted in magenta in Figure 2.9, provides the electric field needed to initiate the plasma. It heats the plasma through Ohmic heating and provides a plasma current that can be shaped by external currents.

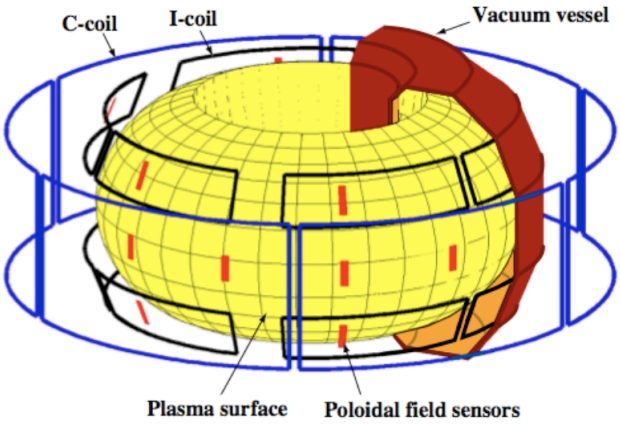

Figure 2.10: Locations of the C-coil and I-coil and poloidal magnetic field sensor used for feedback.

- **Field shaping coil**: the 18 poloidal field coils (F-coils), named F1A to F9A and F1B to F9B, plotted in orange in Figure 2.9, are used to control the shape and position of the plasma. Power supplies act as voltage sources, in series with the F-coils, to provide a wide range of highly shaped, non-circular plasma cross sections.

- **Active control system**: this is made of two systems of active coils: six coils that are located at the vessel midplane, external to the vessel, named C-coils, and twelve internal coils, located above and below the midplane, the I-coils. These coils are used mainly to correct magnetic field errors and to stabilize the $n = 1$ RWM. More recently they have been used for the creation of resonant magnetic field perturbations for ELM stabilization [76].

  The C-coils, shown in blue in Figure 2.10, have been installed in 1994. They form to sets of six 4-turn picture frame coils and can produce a radial field perturbation strength of $15G$ at the plasma surface. They can apply magnetic field perturbations with toroidal mode number up to three.

  The I-coils, shown in black in the same figure, were installed in 2003. This is a set of twelve picture-frame coils located between the vacuum vessel and the carbon tiles. They are six above and six below the midplane.

  The coupling of the I-coils to the plasma is improved with respect to the C-coils because they are closer to the plasma, are inside the vacuum vessel, and have the capability of applying a wide spectrum of magnetic field perturbations. In addition, feedback with the I-coils reduces the phase shift of the feedback field due to the finite impedance of the resistive wall, resulting in a faster time response.

  Magnetic field perturbations with $n = 1$ can be applied with the I-coils by controlling the currents in the upper and lower I-coil arrays. The toroidal

and poloidal mode number of the applied magnetic field can be modified by varying respectively the toroidal and poloidal phase difference between the currents in the upper and lower arrays.

More than 50 poloidal field probes and radial flux loops are installed inside and outside the vacuum vessel. Internal poloidal field sensors are normally used for feedback, as these probes detect the RWM signals enhanced by the eddy-currents on the resistive wall, in contrast to the B_r loops, which are shielded.

The 4 poloidal magnetic field sensors used for feedback are couples of sensors located 180° apart, located at $\phi = 67°, 97°, 127°, 157°$, and hardware subtraction of opposite sensors allows for the elimination of even-n harmonics. By Fourier decomposition, the amplitude and phase of the $n = 1$ mode is then computed, which is used by the feedback controller.

- **Plasma control system** (PCS): it provides a state-of-the-art high-speed, digital control of the magnetic configuration and of various plasma parameters that influence the discharge performance. The system can control the plasma shape, density, pressure, current profile, and toroidal rotation, as well as perform feedback stabilization on the neoclassical tearing mode, resistive wall mode, and apply pre-programmed error field correction.

- **Auxiliary heating systems**: the neutral beam injection (NBI) is the main source of auxiliary heating in DIII-D. Seven neutral beams are routinely used in most experiments ($14MW$ for $5s$ or $17.5MW$ for $3.8s$). By pulse-modulating the sources and adjusting the mix between the co- and counter sources, the injected power and momentum can be continuously and independently controlled. This provides the capability to vary the torque applied to the plasma, decoupling the injected energy and angular momentum.

2.4 Magnetic feedback schemes tested in DIII-D

As described in Chapter 1, steady-state plasmas in advanced tokamak scenarios require the stabilization of RWMs for operation at high-β_N values, above the $\beta_N^{no-wall}$, which is the β_N limit without the wall stabilization. In the presence of a real wall, the external kink mode is in fact converted into a slowly growing RWM, which can be stabilized by active feedback control. The main progresses in developing advanced techniques for magnetic feedback in DIII-D will be described in the following.

As in the RFX-mode case, first RWM control experiments started in DIII-D using the so-called VS algorithm [67], which cancels the radial magnetic field measurements, approximating a perfectly conducting wall. In particular, these experiments used the external C-coils (the internal coils were installed after these

tests) and six radial magnetic field sensors. Let I_k be the current supplied by the feedback amplifier to the coil k. The feedback law, in the VS scheme, can be expressed by the following formula:

$$I_k \propto K_p B_r^{total}(\phi_k) + K_d \frac{B_r^{total}(\phi_k)}{dt}, \tag{2.4}$$

where K_p and K_d are respectively the proportional and derivative feedback gains, and B_r^{total} is the total measured radial field at the vessel wall.

Figure 2.11, taken from [77], shows a comparison of plasma experiments with the same reproducible RWM onset and characteristics, without (solid line) and with active feedback control (dotted line). Without feedback control, at $t \approx 1.4s$, as shown in Figure 2.11(b), a RWM grows causing a β_N collapse. In the experiment which uses the VS scheme with a PD controller, the feedback currents are turned on starting from $t = 1.35s$. In this case, the average RWM amplitude is kept at a low value of about $2 - 3G$, when crossing the stability limit, and the onset of the RWM is postponed by about $40ms$ with respect to the case without feedback.

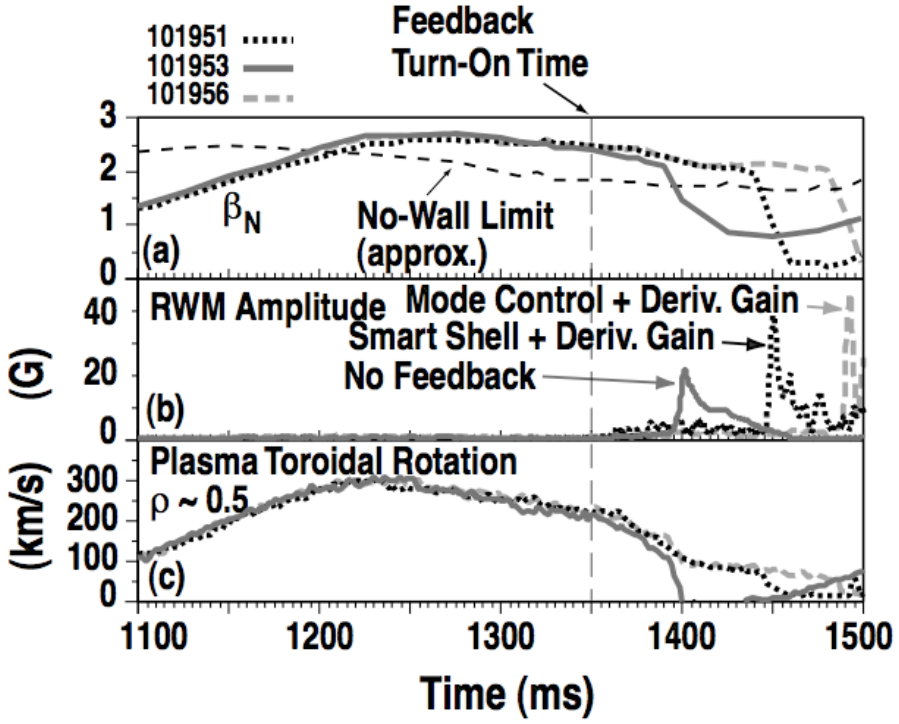

Figure 2.11: Comparison between discharges with feedback applied (#101951, dotted curve, #101956, dashed curve) and without feedback (#101953, solid curve). (a) β_n, (b) the $n = 1$ amplitude of the RWM at the sensor loops and (c) plasma toroidal rotation at the normalized minor radius $\rho \approx 0.5$ (this Figure has been taken from [77]).

The performance of the VS algorithm was improved by changing the connection of the sensors signals, used for feedback, and the C-coils. The radial magnetic field sensors, located 180° apart, have been connected in pair, and hardware subtraction of these opposite sensors allows to compute in real-time the $n = 1$ contribution to the signal. Instead, each of the three feedback coil pairs has been connected in order to respond to the corresponding sensor pair independently. In this way, the resulting external field have $n = 1$ component. Figure 2.12, taken from [77], represents a comparison between experiments with this new configuration of feedback and radial field sensors, and without feedback. With these modifications the efficacy of the feedback system improves: the RWM growth rate increases from about $200s^{-1}$, which is approximately the $1/\tau_w$ in the case without feedback, to about $700s^{-1}$. Moreover, higher derivative gain yields longer stabilization period, with an extension of up to $120ms$ with respect to the no-feedback cases.

The performance of the VS algorithm was further improved when the $n = 1$ poloidal magnetic field measurements were used as feedback variables instead of the radial magnetic field ones. Figure 2.13, published in [78], represents the comparison of feedback control performances when the poloidal and radial field sensors are used in the feedback logic. As shown in Figure 2.13(b), in the magnetic feedback experiments, which used the radial loops, the duration of the high-β period extended up to $40ms$ with respect to the case with no-feedback. In comparison, the use of poloidal magnetic field sensors, not only extended the duration by up to $200ms$ over the no-feedback case, but also allowed the plasma to reach β values about 50% higher than the estimated no-wall stability limit. The improvement produced by the poloidal field sensors has also been confirmed by MARS [79, 80] and VALEN [81] simulations.

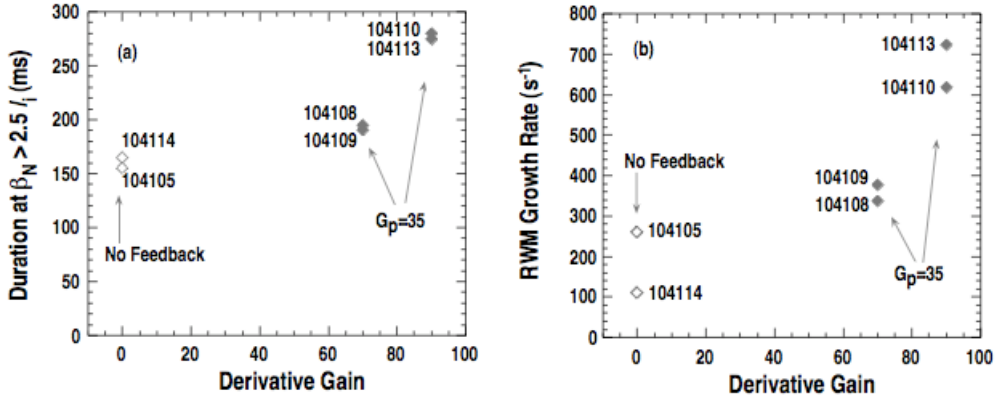

Figure 2.12: Efficacy of the VS feedback system, with the radial and C-coil connection, shown by varying the derivative gain. Plotted versus the derivative gain used are (a) the discharge duration at β_N above the approximate no-wall limit and (b) the growth rate of the RWM which terminates the duration at high beta (this Figure has been taken from [77]).

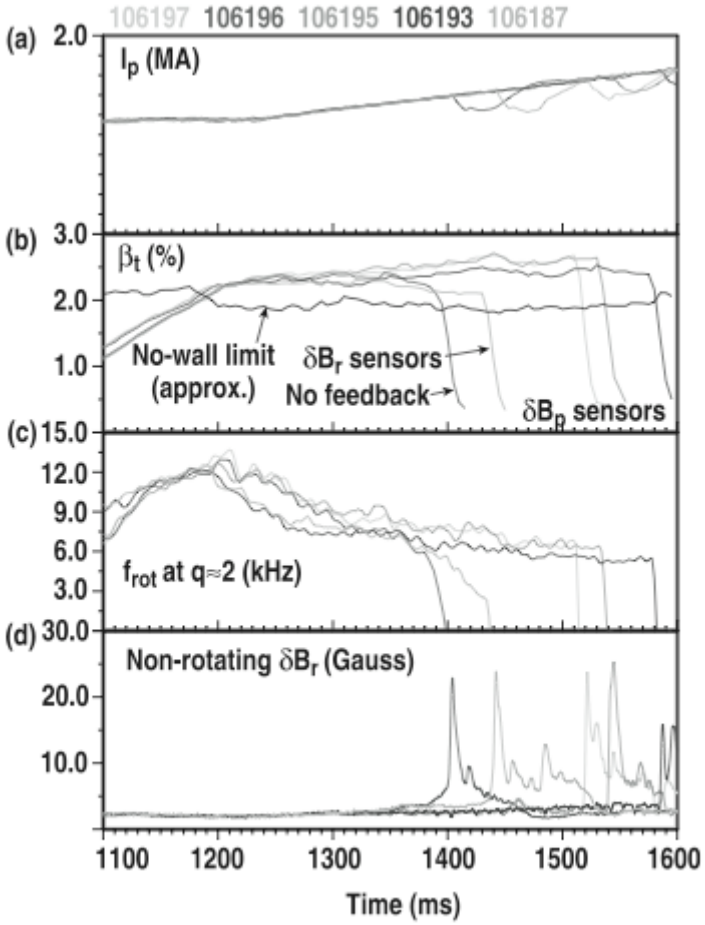

Figure 2.13: Comparison of feedback control with poloidal field sensors (106193, 5, 7), radial field sensors (106187), and no-feedback (106196), showing the time evolution of (a) plasma current, (b) normalized beta, (c) toroidal rotation at the $q = 2$ surface, and (d) amplitude of the $n = 1$ RWM (this Figure has been taken from in [78]).

The advantages of internal over external magnetic field sensors originate primarily in their distance from the plasma, since the normal magnetic field component is continuous across a conducting boundary and it is not shielded by eddy-currents induced in the wall. Moreover, with poloidal magnetic field sensors, a faster time response and improved spatial coupling to the RWM mode structure have been obtained.

Another feedback logic tested in DIII-D is the so-called mode control [82]. The mode control essentially consists of overdriving the VS algorithm by decoupling the sensors from external magnetic fields. In this approach, the portion of the magnetic field measured by the sensor loops due to external field sources B_p^{ext}, is subtracted from the sensor signals B_p^{total}. The remaining portion of the sensor signal is due only to the field from the plasma. In this way, the plasma response,

B_{plasma}, is calculated, which is the quantity the feedback reacts to. The feedback law, in the mode control scheme, becomes:

$$I_k \propto K_p(B_p^{total} - B_p^{ext})(\phi_k) + K_d \frac{(B_p^{total} - B_p^{ext})(\phi_k)}{dt}, \tag{2.5}$$

where δB_{ext} is the contribution from the external coils, and it is determined from the couplings at zero-frequency between each actuator and sensor, as will be described in Chapter 7. A test of the mode control scheme is shown in Figure 2.11. Longer stabilization periods, up to about $90ms$, are obtained with this mode control algorithm and derivative gain, with respect to the case without feedback, and up to about $50ms$, with respect to the VS scheme.

This feedback control algorithm differs from the RFX-mod one, described in Section 2.2. In DIII-D mode control scheme, the magnetic field measurements are compensated in real-time from external magnetic fields. In this way the plasma response is calculated which is the quantity the feedback reacts to. Instead, in RFX-mod the feedback variable is the total radial magnetic field (the magnetic field due to the plasma and that produced by external field sources) measured by the radial sensor loops.

In DIII-D the feedback control algorithm normally used is the mode control. In the last years, advanced error field correction strategies have been developed to improve magnetic feedback control in advanced tokamak scenarios: pre-programmed and dynamic error field correction, which will be described in the following.

The magnetic feedback control in the DIII-D experiment can be divided into a fast feedback action (with timescale $< \tau_w$) and a slow feedback action (with timescale $> \tau_w$). The C-coils are normally used for the slow feedback part, in particular for error field correction (EFC), in a pre-programmed manner. The EFC allows for the correction of the external non-axisymmetric fields that come from misalignments of coils and other non-axisymmetric structures, such as large portholes or coil feeds. Instead, the I-coils are used for fast feedback actions, not only for the control of RWMs, but also for dynamic error field correction (DEFC). The DEFC scheme compensates for the component of the error field, which can resonate with the stable RWM, destabilizing it through resonant field amplification.

When DEFC is used, the plasma is sustained above the no-wall stability limit for long durations. An example that clarifies the role of the DEFC has been published in [55], and is reported in Figure 2.14. The plasma experiments are very similar. In both cases a ramp of I-coil current is pre-programmed, but, in the test plotted with a solid curve, the I-coil current is feedback-controlled starting from $t = 1300ms$, while in the other one (dotted line) the I-coil current is removed at $t = 1500ms$, as shown by the I-coil signals plotted in the top panel in Figure 2.14.

With DEFC provided by the I-coils, β_N is sustained at values well above the no-wall stability limit for almost $3s$. Instead, in the other discharge, when the I-coil current is removed at $t = 1500ms$ there is an immediate response by the stable

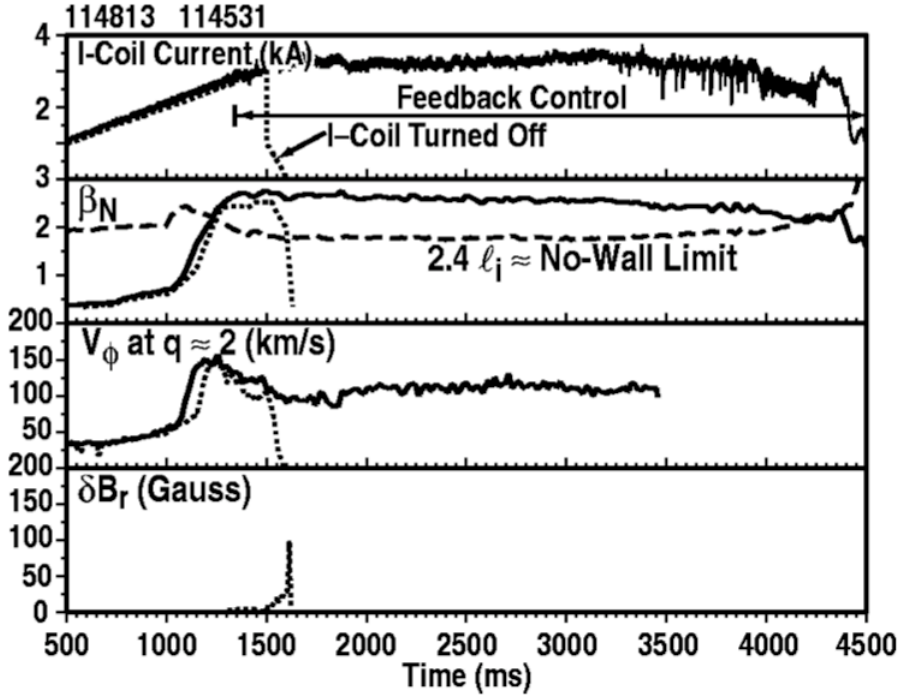

Figure 2.14: Feedback-controlled error field correction of discharge 114531 (solid curve), and a similar discharge without error correction, 114813 (dotted curve). Shown are (a) I-coil current, which is feedback-controlled after $t = 1300ms$ in discharge 114531, (b) normalized beta and the estimated no-wall limit, (c) toroidal rotation speed at $r/a = 0.6$, and (d) amplitude of the RWM (this picture has been taken from [55]).

RWM, which slowly increases in amplitude as the plasma rotation decreases. After $100ms$, the rotation has decreased below the stability threshold and the RWM grows more rapidly leading to a β-collapse.

As shown in this experiment, the combination of fast and slow feedback allows to improve the plasma performance and an important role is played by the DEFC, which suppresses the magnetic field errors that can resonate with marginally stable RWMs. Since tokamak plasmas with high-β and low rotation are less resilient to error fields, this results indicate that the response of the plasma must be considered carefully, also in the preparation of error field correction schemes for ITER [83].

CHAPTER 3

Model-based design of tearing mode control in RFX-mod

In this Chapter, a non-linear torque-balance model, which describes the tearing mode dynamics in presence of the multiple-shell layout and of the magnetic feedback of RFX-mod, will be presented, along with its application to find an optimized gain set for the mode controller. This model-based optimization approach is then compared with an empirical one, used before this Thesis work. The effect of feedback gains on mode dynamics has been simulated and an extensive gain scan has been performed, to find an optimal gain set for a spectrum of multiple tearing modes. The goal is to reduce to the lowest possible value the edge radial magnetic field, maintaining at the same time the modes into slow rotation and avoiding coil current saturations. In the empirical optimization approach, on the other hand, a partial gain scan was executed in the experiment for a limited set of tearing modes, given the large number of discharges needed for a complete optimization. The differences between the two control optimizations and the main experimental results obtained will be presented.

3.1 Empirical optimization of the tearing mode magnetic feedback control in RFX-mod

As described in Chapter 1, the magnetic feedback control for multiple MHD modes, made with the RFX-mod active control system, allowed the exploration of high-plasma current regimes up to $2MA$, for the first time in a RFP [24], and for the discovery of a new self-organized helical equilibrium, the so-called SHAX state, which features low magnetic chaos and good confinement properties [40].

An optimization of these high-current regimes has been performed in the last years with the aim of improving the confinement performance and the machine operation efficiency. The optimization strategy was focused on tearing mode control and error field correction. The experimental results obtained during this Thesis work on this subject will be presented respectively in this Chapter and in the next one.

During this Thesis work, a model of the non-linear dynamics of multiple interacting tearing modes [84] has been used to optimize the mode controller. The aim of this model-based optimization is to find a gain set, which produces the lowest possible value of the edge radial magnetic field amplitude, maintaining at the same time the modes into slow rotation and avoiding coil current saturations [42].

The model-based gain set has been compared with an empirical one, which had been identified previously with the following approach. A partial gain scan was performed in the experiment for a limited set of tearing modes, given the large number of discharges needed for a complete optimization. The criterion for selecting the proportional-derivative (PD) gains in the empirical approach was to reduce δ_1, the maximum non-axisymmetric $m = 1$ distortion of the LCFS due to the spatial overlap of multiple tearing modes, defined in Chapter 2, page 37. Since a large non-axisymmetric distortion due to the phase-locking of multiple tearing modes can cause strong plasma-wall interaction localized in limited areas of the RFX-mod first-wall [23] and the Ohmic input power increases with the plasma current and reaches values of a few $10MW$, the plasma-wall interaction may represent an operational limit, particularly at high-current.

An example of a discharge with a strong phase-locking of multiple tearing modes, which leads to a severe plasma-wall interaction is shown in Figure 3.1. In this case, the gains applied to the $m = 1$ tearing modes are not optimal. The QSH state does not develop, as shown in Figure 3.1(b), where the normalized edge radial magnetic field amplitude is shown for the innermost resonant $m = 1$ tearing modes, and the modes do not rotate, as reported in Figure 3.1(c) where the phase of the same modes is plotted. Hence, a high value of the $m = 1$ deformation of the LCFS has been obtained, up to $2cm$, as shown in Figure 3.1(d). In addition the LCFS deformation is not spread along the toroidal angle, but the phase-locked tearing modes produce a deformation toroidally-localized at the poloidal gap of the wall structure at $\phi = 292.5°$, represented with continuous lines in Figure 3.1(e).

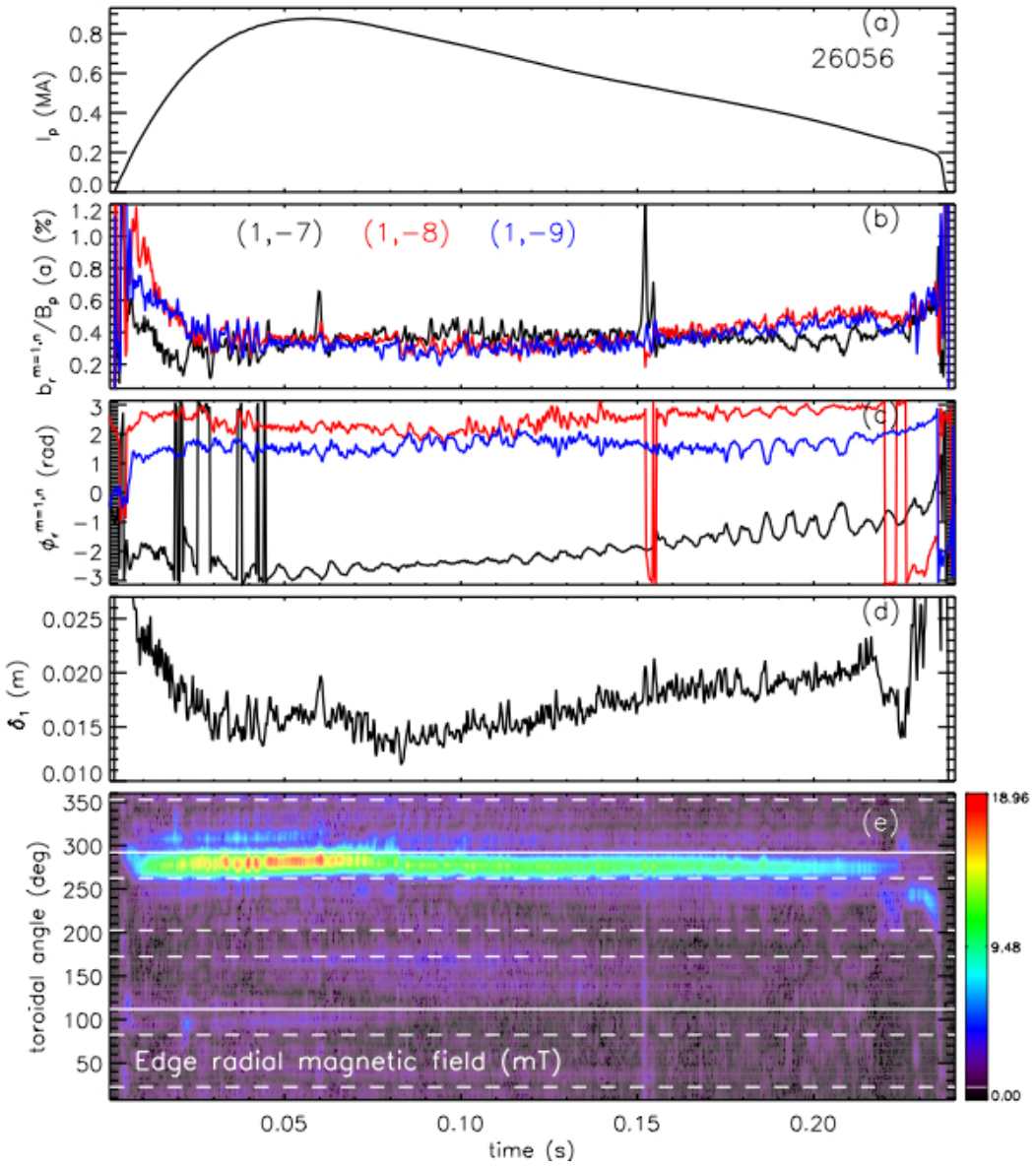

Figure 3.1: (a) Plasma current, (b) normalized edge radial magnetic field amplitude and (c) phase of the (1,-7) (in black), (1,-8) (in red), (1,-9) (in blue) modes, (d) non-axisymmetric $m = 1$ distortion of the LCFS and (e) contour plot of the edge radial magnetic field as a function of time and the toroidal angle for the discharge 26056. The toroidal positions of poloidal gaps of the wall structure are represented with continuous lines, white those of the portholes with dashed lines.

In the empirical approach, the PD gains in the mode controller were adjusted to break as much as possible the phase-locking among these modes with the aim of reducing the toroidally-localized $m = 1$ deformation of the LCFS evidenced above.

m=1,n=	-7	-8	-9	-10	-11	-12	-13	-14	-15	-16
K_p	800	700	700	500	500	600	550	550	550	550
K_d	0	0.5	1	0	1	1	0.5	0.5	0.5	0.5

Table 3.1: Proportional and derivative gains of the empirical gain set.

This was obtained by differentiating the mode rotation frequency, setting different derivative gains on $m = 1$ tearing modes with consecutive n values. The PD gains obtained in this way are reported in the Table 4.1:

3.1.1. Using complex gains allows to better control the mode rotation frequency

To further reduce the phase-locking among different modes, complex gains has been also applied to single or multiple tearing modes. Using a complex gain consists in adding a spatial phase difference between the measured harmonic and the externally applied one, which exerts a net torque on the mode, that can be increased by increasing the phase of the complex gain. This is realized by adding

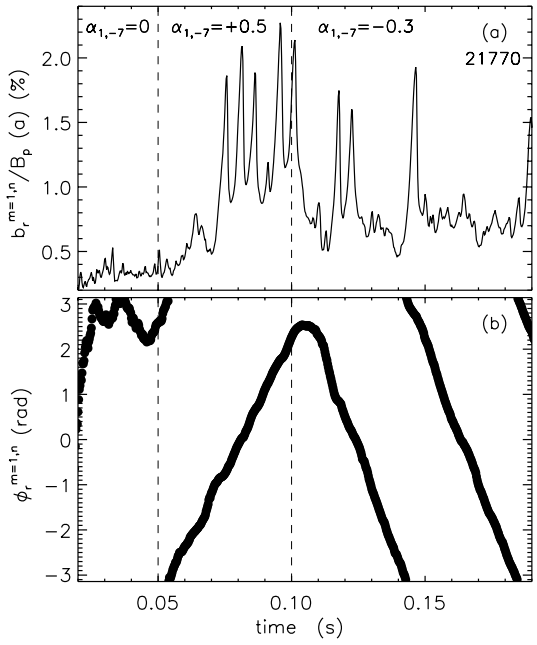

Figure 3.2: Time evolution of (a) the normalized edge radial magnetic field amplitude and (b) phase of the $(1, -7)$ mode for shot 21770, in which different values of the proportional gain phase have been tested in different time periods.

an imaginary part to the proportional gain, which has been redefined as $K_p^{m,n} = |K_p^{m,n}|e^{i\alpha_{m,n}}$.

An example of the application of a complex gain to the (1,-7) mode is shown in Figure 3.2. Here the gain phase has been varied in different time windows and the effect on the mode dynamics can be observed. As anticipated above, the angular frequency increases with $\alpha_{m,n}$ and the sign of $\alpha_{m,n}$ sets the sign of the angular frequency, as confirmed in Figure 3.2(b).

The same exercise has been then applied to multiple modes, trying to determine simultaneously the signs and values of their angular frequencies. In particular, a phase with alternating signs on consecutive modes has been set in the experiment

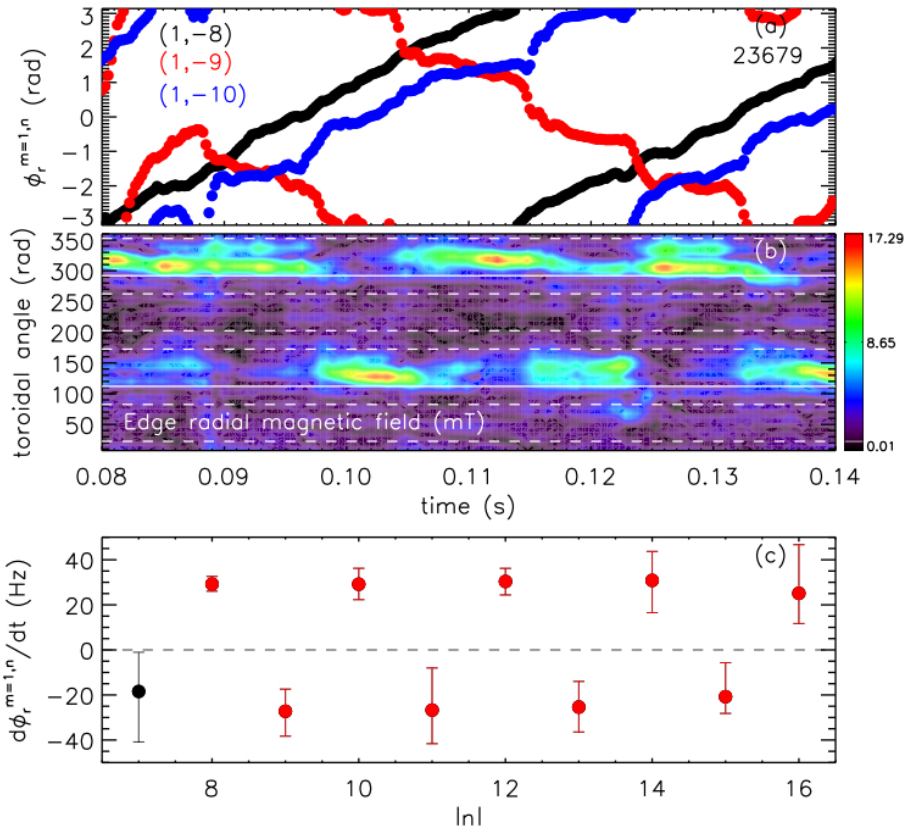

Figure 3.3: (a) Time evolution of the (1,-8) (black), (1,-9) (red), and (1,-10) (blue) mode phases. (b) Contour plot of the edge radial magnetic field as a function of time and toroidal angle. The toroidal positions of poloidal gaps of the wall structure are represented with continuous lines, white those of the portholes with dashed lines. (c) Angular frequency of tearing modes. Each point represents a flat-top average and the error bars are the 25^{th} and the 75^{th} percentiles of the data. The red color indicates the range of tearing modes with complex gain applied. The plasma experiment corresponds to the 23679 discharge.

reported in Figure 3.3. While the sign of the mode angular frequency is alternated, as shown in Figure 3.3(c), no significant reduction of the LCFS distortion is observed. This may be explained by the fact that, when $\alpha_{m,n}$ is not zero, the effective gain is reduced and therefore a slight increase of the edge radial magnetic field occurs. This may instead increase the phase-locking between the modes. As a result, the localized $m = 1$ deformation is not reduced, and jumps between two locations, which correspond to the two poloidal gaps in the wall structure, as shown in Figure 3.3(b). Here localized error fields may be present that increase the phase-locking among the modes.

Adding an imaginary part to the proportional gain is thus effective in maintaining the modes into rotation at the requested angular frequency, but in the experiments performed so far it has not allowed to reduce the phase-locking among the secondary $m = 1$ modes.

3.2 A model of the tearing mode dynamics with magnetic feedback

A model of the non-linear dynamics of multiple interacting tearing modes, including their feedback control, has been developed and implemented in the so-called RFXlocking code. The code has been described in [84]. In the version used in this Thesis work for the controller optimization, a model of the wall reproducing the multiple shell structure of RFX-mod has been implemented. The model adopts cylindric geometry and, for simplicity, the copper shell is assumed to be uniform, so that the effects of gaps and portholes are not considered.

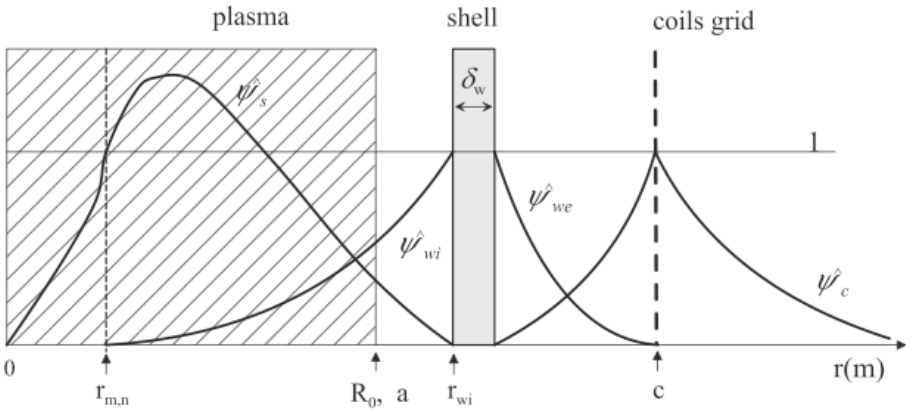

Figure 3.4: Schematic representation of Newcomb's solution splitting for each (m, n) mode. The shaded region represents the plasma region, the shell is considered uniform and with width δ_w, and the coil mesh is placed outside the shell as in RFX-mod. This picture has been taken from [84] and the scheme is a simplification of the multiple-shell layout of the RFX-mod experiment.

The radial magnetic field eigenfunction $\psi^{m,n}(r,t)$ of each (m,n) tearing mode is obtained solving the Newcomb's equation. The approach used to calculate its solution is to split it as a linear combination of different contributions $\psi^{m,n}(r,t) = \psi_s^{m,n}(t)\hat{\psi}_s^{m,n}(r) + \psi_{wi}^{m,n}(t)\hat{\psi}_{wi}^{m,n}(r) + \psi_{we}^{m,n}(t)\hat{\psi}_{we}^{m,n}(r) + \psi_c^{m,n}(t)\hat{\psi}_c^{m,n}(r)$, obtained in separate radial regions delimited by the magnetic axis at R_0, the resonant surface at $r_{m,n}$, the shell at r_{wi} and the active coils at c, as shown in Figure 3.4.

The radial derivative of $\psi^{m,n}(r,t)$ has jumps across the resonant surface and the coil radius, as shown in Figure 3.4. These jumps are associated with helical current sheets flowing at the resonant surface, related to the presence of a magnetic island and with the coil currents.

The Newcomb's solution is discontinuous also at the shell, due to the presence of eddy-currents induced by time-varying magnetic fields. Moreover, the solutions are not valid inside the shell region, where another equation holds, the so-called *thick-shell approximation equation* [85] that describes the radial field diffusion inside the shell. Therefore, the Newcomb's solutions for each tearing mode are matched at $r = r_{m,n}$ and $r = r_{m,n} + \delta_w$ with the solution of the thick-shell approximation equation.

RFXlocking solves the flux-surface averaged momentum equations for both the toroidal and the poloidal angular frequency, including the viscous torque due to the fluid motion and the electromagnetic torques produced by the external currents (i.e. the feedback and the eddy-currents on the wall) on the mode rational surface, and by the non-linear interaction between different tearing modes. In particular, RFXlocking solves the following fluid equation of motion for the toroidal Ω_Φ and poloidal Ω_θ flux-surface averaged angular frequencies:

$$\rho\frac{\partial\Omega_\Phi}{\partial t} = \frac{1}{r}\frac{\partial}{\partial r}\left(\mu r\frac{\partial}{\partial r}\Omega_\Phi\right) + S_\Phi + \sum_{\substack{m\in Z\\ n>0}}\frac{\delta T_{EM}^{m,n}}{4\pi^2 r R_0^3}\delta\left(r - r_{m,n}\right), \tag{3.1}$$

$$\rho\frac{\partial\Omega_\theta}{\partial t} = \frac{1}{r^3}\frac{\partial}{\partial r}\left(\mu r^3\frac{\partial}{\partial r}\Omega_\theta\right) - \frac{\rho}{\tau_D}\Omega_\theta + S_\theta - \sum_{\substack{m\in Z\\ n>0}}\frac{m}{n}\frac{\delta T_{EM}^{m,n}}{4\pi^2 r^3 R_0^3}\delta\left(r - r_{m,n}\right), \tag{3.2}$$

where μ is the plasma perpendicular viscosity, ρ is the density, τ_D is the poloidal flow damping time, and S_ϕ, S_θ are phenomenological momentum source densities, which are constant and maintain the plasma rotation.

The model evolves the mode edge amplitudes and phases under the action of the feedback coils, while the mode amplitudes at the resonant surface are fixed during the simulation and can be calculated from the experimental measurements [71]. The mode amplitudes at the rational surface are zero at the beginning of the simulation and then increase exponentially up to the fixed value chosen for the simulation. The initial mode phases can be also chosen here as in the experiment and tearing modes co-rotate with the ion fluid at the resonant surface in order to satisfy the no-slip condition. More details on these simulations, and in particular

on the initial conditions, can be found in [84]. A self-consistent model should also include the non-linear evolution of the whole mode eigenfunction by solving the full system of MHD equations. Nonetheless this would imply a much more demanding numerical effort, which is beyond the scope of the present work.

The model introduced above reproduces with good accuracy the experimental results. For example, the model foresees rather well the request of coil current

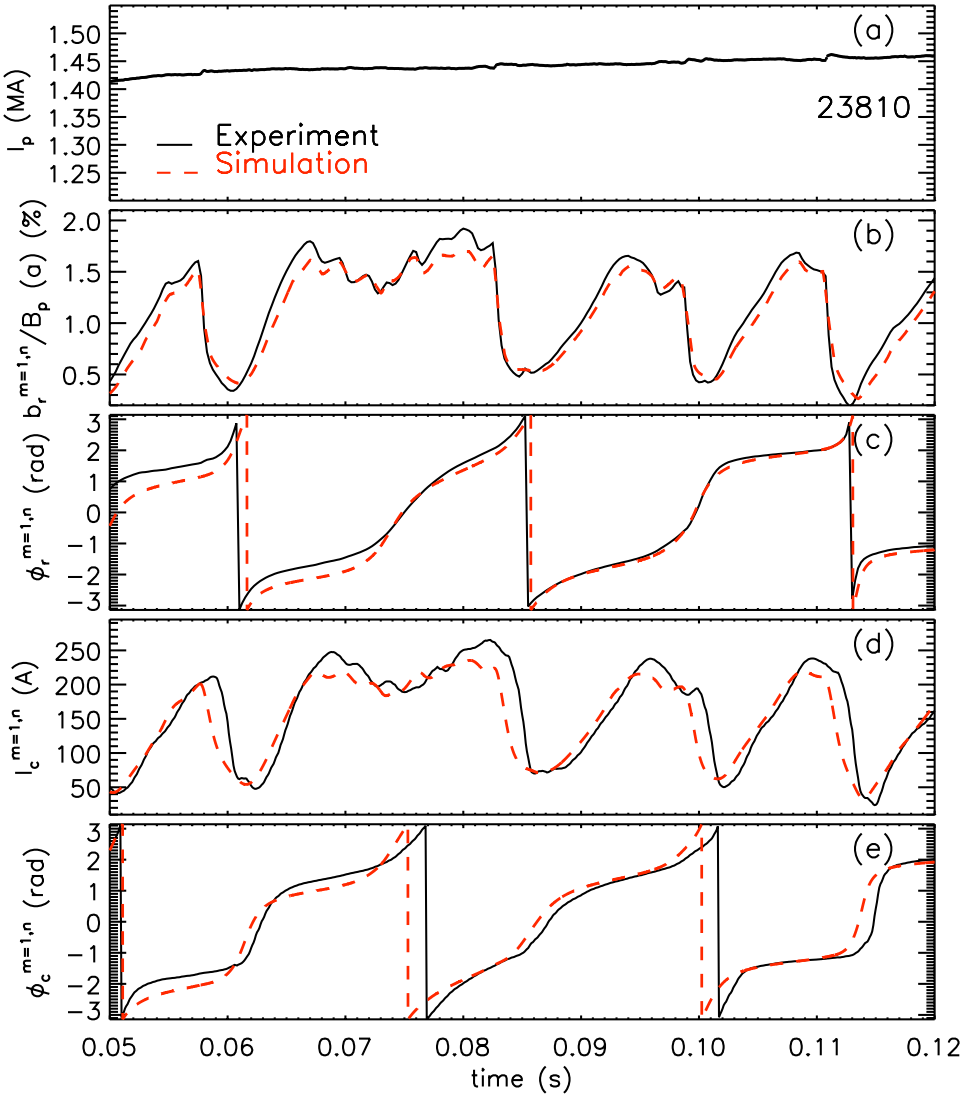

Figure 3.5: (a) Plasma current, (b) normalized edge radial magnetic field amplitude of the $(1,-7)$ mode, (c) $(1,-7)$ mode phase, (d) $(1,-7)$ coil current amplitude, and (e) the corresponding phase in a 1.45 MA discharge (straight black line) and from the simulation described in the text (dashed red line). The plasma experiment refers to the 23810 discharge.

for the $(1, -7)$ mode control and the corresponding phase, as reported in Figures 3.5(d) and (e). In this Figure, which represents a $1.45MA$ RFX-mod discharge, the experimental time traces are plotted with black continuous lines, while the corresponding RFXlocking predictions with dashed red lines. Note that the mode dynamics of the $(1, -7)$ mode under the feedback action is characterized by a sawtooth-like behavior due to relaxation events [31], as shown in Figure 3.5(b), where the the normalized edge radial magnetic field amplitude of the $(1, -7)$ mode is plotted with the corresponding simulated time trace.

The model proves to be effective also in reproducing the feedback action on tearing mode dynamics by varying the feedback gains. The effect of the proportional gain on the $(1, -7)$ mode angular frequency, the normalized edge radial magnetic field amplitude and the coil current amplitude is shown in Figure 3.6. The experimental data (full circles) are compared with the model predictions for the same type of discharges (red dashed line). Each point represents a time average over the discharge flat-top. Note that the error bars represent the temporal variation of the above quantities associated with the sawtooth-like dynamics of the $(1, -7)$ mode already illustrated in Figure 3.5. They are not measurement errors, which are actually much lower.

The simulation predicts the existence of a broad minimum of the normalized edge radial magnetic field amplitude plotted as a function of the proportional gain. The $(1, -7)$ normalized edge radial magnetic field amplitude is reduced by increasing the proportional gain, up to a threshold $K_p^{m,n}$ value, above which any further increase is not beneficial, but leads only to faster mode rotation, as it can be seen in Figures 3.6(a) and (b). This is due to delays introduced by the shell, the vacuum vessel and the power supplies, which are modeled in the RFXlocking code with a one-pole filter law, with a cut-off frequency corresponding to a delay $\tau_d = 1.5ms$. The delays determine a phase shift between the targeted harmonic and the field produced by the feedback system. The phase shift introduces a torque, which sustains the tearing mode rotation against the braking effects of the shell and the vacuum vessel. Note that, both in the model and in the experiment, positive and negative angular frequency solutions are obtained, even if the former is more frequent in the experiment, as was already shown in the statistical analysis in Figure 2.6.

The above results indicate that the RFXlocking code can reproduce quite well the tearing mode dynamics with magnetic feedback. It can be thus regarded as a useful tool to predict the mode behavior when the feedback parameters of the mode controller are varied. In this way, it is possible to fine-tune offline the tearing mode controller, saving experimental time. As it will be discussed in the next Section, in this Thesis work, this approach has been adopted to find a model-based gain set.

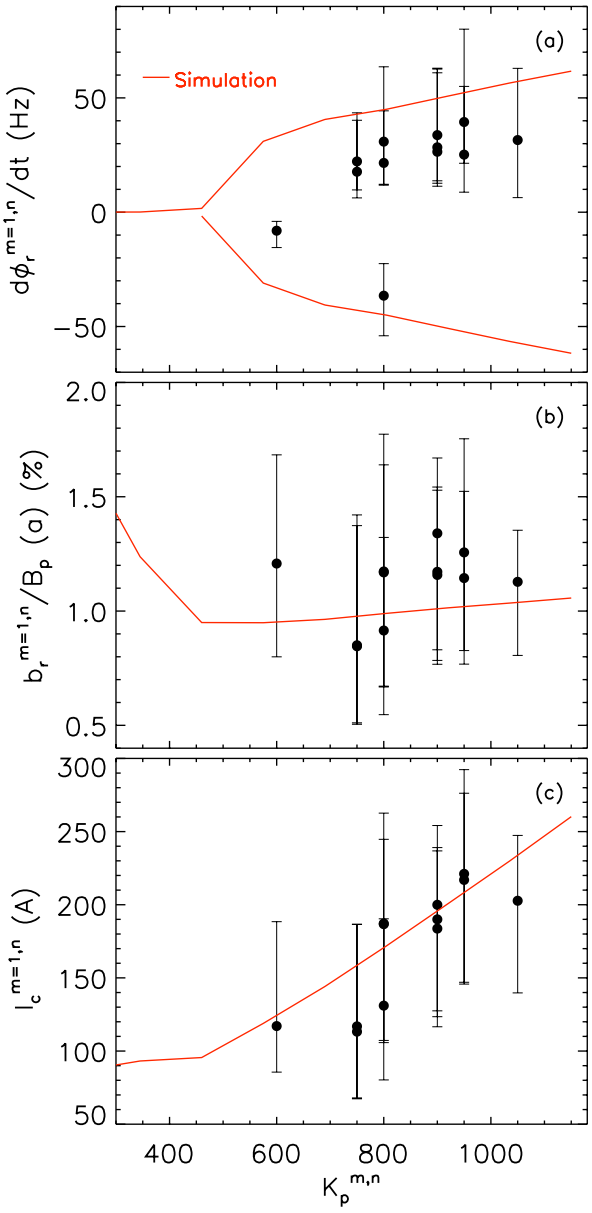

Figure 3.6: Effect of a proportional gain scan on (a) the $(1,-7)$ mode angular frequency, (b) the $(1,-7)$ normalized edge radial magnetic field amplitude, and (c) the $(1,-7)$ coil current amplitude. Each point represents a flat-top average and the experimental points are from a set of $1.4MA$ reproducible discharges. The error bars are 25^{th} and the 75^{th} percentiles of the data. They represent the variation of the above quantities due to the natural mode dynamics, not measurement errors. The red curve represents the RFXlocking code prediction.

3.3 Model-based approach to the mode controller optimization

In this Section, the model-based approach applied to optimize the mode controller will be described. The strategy employed for the optimization has been to simulate the dynamics of each tearing mode under the action of magnetic feedback, scanning the proportional and derivative gains over a $2D$ grid, looking for a gain set that produces the lowest possible value of the edge radial magnetic field amplitude predicted by the model, maintaining at the same time the modes into rotation and avoiding saturations of the feedback coil currents. In this case, only the PD gains were used. The integral gain has been neglected since it proved not to be effective on this type of modes. Tearing modes in fact slowly rotate, while an integral gain would be more useful for static or slowly growing perturbations.

The reference discharge chosen for this scan is the same as in Figure 3.5. Since the number of variables involved in the optimization is rather high (10 modes with $m = 1, n = -16, .., -7$ and different gain values), the $2D$ scan has been applied on each mode once at a time, neglecting the non-linear interaction among different modes. It has been also verified, by comparing multi-mode and single-mode simulations in some single cases, that the non-linear interaction has no great impact on the tearing mode edge amplitudes, which is the quantity one wants to reduce, but it has only a small effect on the mode angular frequencies. For this reason, it is expected that neglecting the non-linear interaction among tearing modes does not affect significantly the optimization procedure.

The $2D$ gain scans mentioned above predict that a minimum radial magnetic field exists for a couple of proportional and derivative gains. These gains can be different for each mode. This is shown for the $(1, -7)$ mode in Figure 3.7 on the left, which represents the normalized edge radial magnetic field amplitude in the top figure and the coil current amplitude in the bottom figure, as a function of the proportional and derivative gains. The variables represented in the contour plots are averages in the time interval $\Delta t = [50, 120]ms$. The minimum radial magnetic field amplitude predicted by the RFXlocking code is obtained at $K_p^{m,n} = 720$ and $K_d^{m,n} = 1.8$ and is indicated with the star in Figure 3.7(a). These gains differ significantly from the values obtained with the empirical optimization, which are indicated in the same Figure with a rhomb.

The model also predicts that the feedback coil current amplitude on the $(1, -7)$ mode increases as a function of both $K_p^{m,n}$ and $K_d^{m,n}$, as shown in Figure 3.7(b) on the left. This introduces an important constraint in the mode controller optimization, since coil current saturations, which happen at $320A$ for the RFX-mod power supplies, must be avoided. The region above which the saturations take place is shown in Figure 3.7(b) with a black contour line.

Instead, Figure 3.7 on the right represents the 2D gain scan applied to the $(1, -8)$ mode. Also in this case, the empirically-optimized gains differ from the

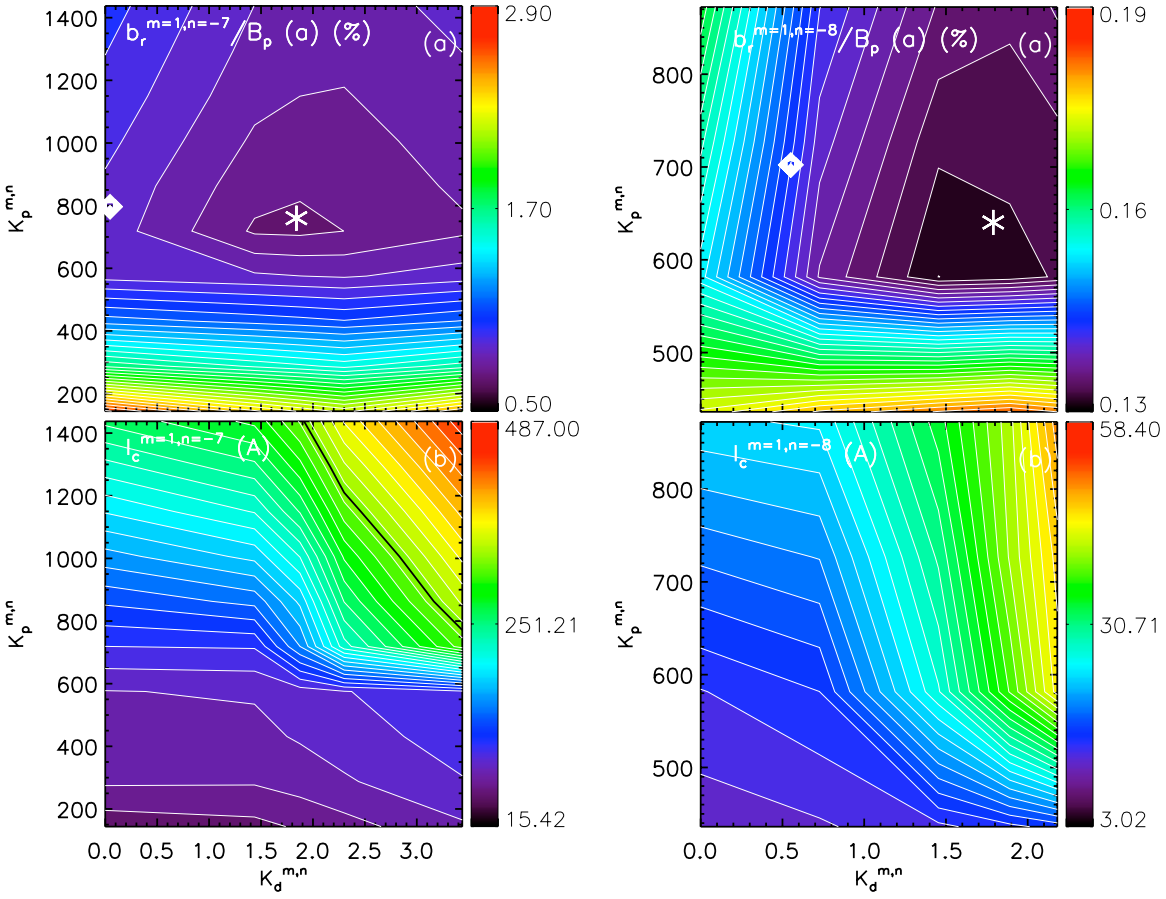

Figure 3.7: On the letf: (a) contour plot of the $(1,-7)$ normalized edge radial field amplitude and (b) of the $(1,-7)$ mode coil current amplitude as a function of proportional and derivative gains. The coil current $320A$, above which the coil current saturations take place, is marked with a black contour. On the right: the same plots for the $(1,-8)$ mode. The rhomb corresponds to the empirically-optimized gain set, the star to the model-based one.

model-based ones, plotted in the Figure respectively with a rhomb and a star.

The $2D$ scan in the $K_p^{m,n} - K_d^{m,n}$ plane described above has been applied to each tearing mode with $m = 1, -16 \leq n \leq -7$, searching for the gains that allow to obtain, for each mode, the minimum edge radial magnetic field amplitude compatible with the tearing mode dynamics and the feedback system limits. The $K_p^{m,n}$ and $K_d^{m,n}$ gains calculated in this way are plotted with red squares in Figure 3.8, where they are compared with the empirically-optimized gains, reported in Table 4.1, and plotted here with black circles. The obtained $K_p^{m,n}$ values in the model-based case are lower than in the empirical gain set, while the $K_d^{m,n}$ values are higher.

Note that these two optimization strategies are actually different. As discussed in Section 3.1, the empirical gain set was selected to differentiate each mode angular frequency and hence to reduce the phase-locking among the modes, while the model-based set is devoted to the reduction of the edge radial magnetic field amplitude of each mode to the lowest possible value, regardless of the phase relations among the modes. As it will be described later, the fact that the phase-locking among tearing modes has not be taken into account in the model-based approach has a consequence: the LS parameter, which quantifies the strength of constructive interference among tearing modes as described in Chapter 2, increases slightly in the model-based case.

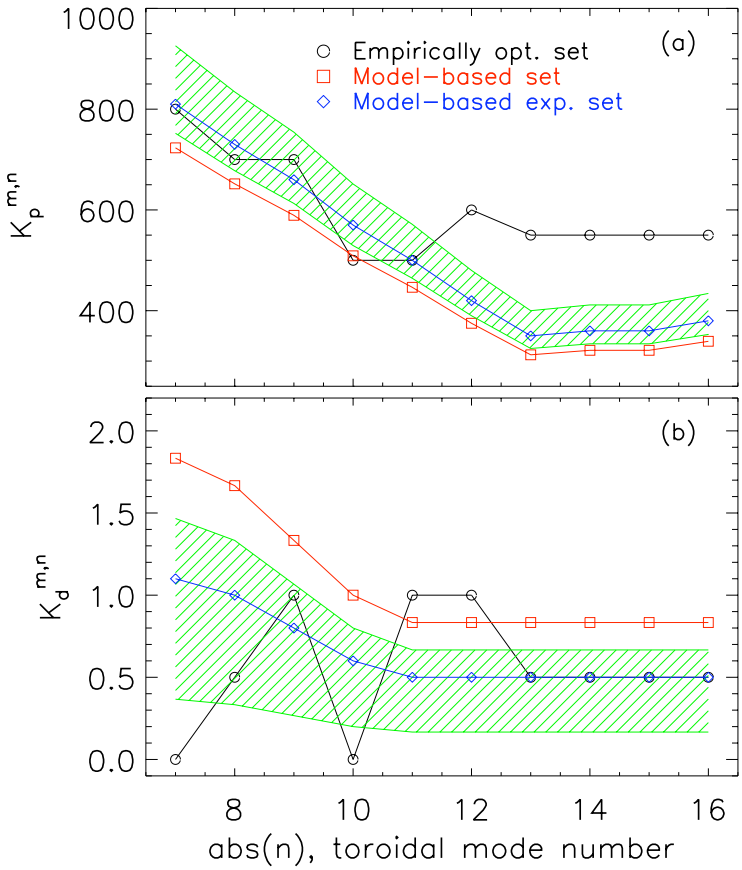

Figure 3.8: (a) $K_p^{m,n}$ and (b) $K_d^{m,n}$ gains applied to the tearing modes with $m = 1, n = -16, .., -7$. The black open circles correspond to the empirically-optimized gain set, the red squares to the set predicted by the RFXlocking code, and the blue diamonds to the optimal model-based set found in the experiment, as explained in the text. The ranges of gains explored in the experimental campaign are indicated by the green shaded region.

3.4 Application of the model-based PD gains to the experiment

The existence of a minimum edge radial magnetic field amplitude in the $K_p^{m,n}$-$K_d^{m,n}$ plane predicted by the model and described in the previous Section has been tested in an extensive experimental campaign. Given the large number of discharges that this would require, it is practically impossible to perform a complete $2D$ scan on each mode, as it was done in the model. For this reason, the criterion adopted for the experimental scans was to maintain the trends of $K_p^{m,n}$ and $K_d^{m,n}$, as function of n, suggested by the model and to multiply all of them respectively by the same constants α_{K_p} and α_{K_d}.

These two constants have been varied in the experiment in the range $\alpha_{K_d} \in [0.2, 0.8]$ and $\alpha_{K_p} \in [1., 1.3]$. The explored gain range, indicated with the green shaded region in Figure 3.8, is limited in the experiment by two effects: first, by hardware limits, since at high gains the feedback coil currents saturate, as said above; second, at low gains by the fact that the modes become wall-locked and the discharge performance degrades significantly.

The existence of a minimum edge radial magnetic field amplitude for some optimal gain values has been confirmed by a statistical analysis of a set of 35 reproducible discharges with plasma current in the range $I_p \in [0.85, 0.95]MA$, reversal parameter $F \in [-0.045, -0.030]$, and density normalized to the Greenwald density $n/n_G \in [0.05, 0.25]$. Figures 3.9(a) and (b) show respectively the experimental and simulated contour plot of the total normalized edge radial magnetic field amplitude, defined by the Equation (2.2), as a function of α_{K_p} and α_{K_d}. In particular, each point in the simulated contour plot corresponds to an average of several multi-mode simulations of different discharges with the same gain set.

The minimum $b_r^{tot}/B_p(a)$ value has been obtained with α_{K_p}= 1.12 and α_{K_d}= 0.6 and the corresponding gain set is plotted with blue diamonds in Figure 3.8. The model-based proportional gains are lower than the empirical ones for $n < -11$, while the model-based derivative gains are significantly different for $n > -13$ with respect to the empirically-optimized ones. The difference in the derivative gains, in particular, reflects the different criteria used in the two optimizations: as said above, in the model-based approach the aim is only to reduce the edge radial magnetic field amplitude, while in the empirically-optimized one to avoid the phase-locking among different modes. This can be obtained by differentiating the mode angular frequency, which can be realized differentiating the derivative gains in consecutive modes.

The minimum $b_r^{tot}/B_p(a)$ values found in the experiment and in the multi-mode simulations are in reasonably good agreement. The two minima occur for similar values of the gains, small discrepancies being possibly due to some simplifications made in the model. In fact, the minimum predicted by the model occurs at slightly higher derivative gains than in the experiment. The derivative gain has usually

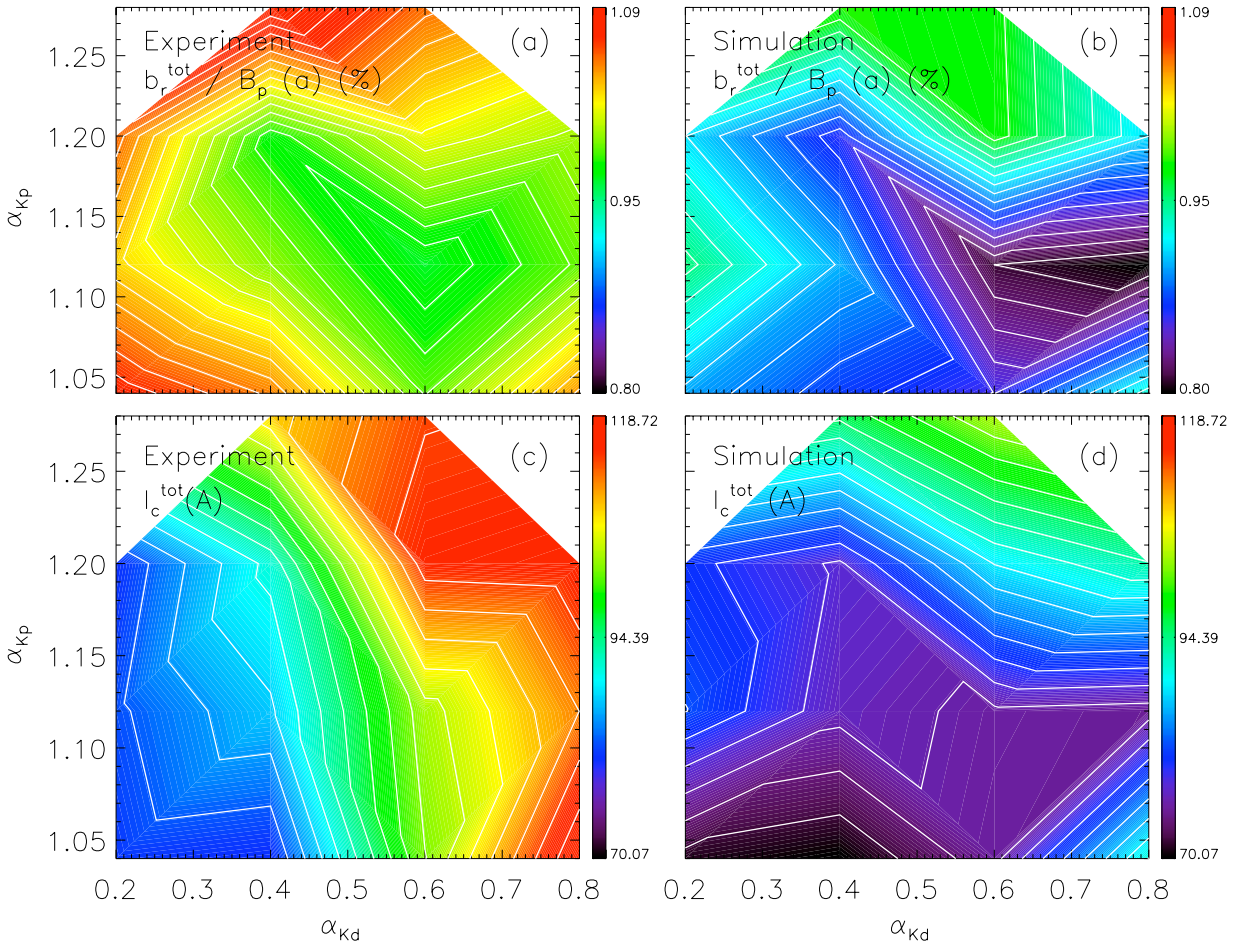

Figure 3.9: Contour plot of b_r^{tot} and I_c^{tot} for (a-c) the experiment and (b-d) the simulation as a function of α_{K_p} and α_{K_d}, respectively. The above quantities are defined in the text.

the function to counteract the various delays present in the feedback loop. An over-estimation of these delays in the model may explain such a discrepancy.

To quantify the total requested coil current amplitude, the quantity I_c^{tot}, defined by the Equation (2.3), has been calculated. The $2D$ contour plots of I_c^{tot} for the experiment and the simulation are shown respectively in Figures 3.9(c) and (d) as a function of α_{K_p} and α_{K_d}. Also in this case the agreement is generally good. Small deviations may be possibly attributed to the same causes explained above.

3.4. Application of the model-based PD gains to the experiment

3.4.1. Effects of the model-based gain optimization on the plasma performance

The effects of the gain optimization described above are not only limited to a reduction of the edge radial magnetic field amplitude. Since the tearing mode eigenfunctions are extended throughout the plasma radius, it is expected that the reduction of the radial magnetic field amplitude at the plasma edge has also sizable effects in the plasma core, in terms of reduction of the magnetic field stochasticity and of improvement of the plasma confinement. The radial eigenfunctions of the $m = 1$ secondary modes have been reconstructed by solving the Newcomb's equation, using as boundary conditions the edge measurements [71]. The total $m = 1$ secondary mode amplitude in the core is then estimated using the perturbed radial magnetic field at the resonant radius, $b_{res}^{1,n}$, as follows:

$$b_{res}^{sec}/B_p(a) = \sqrt{\sum_{m=1,n=-16}^{-8} (b_{res}^{1,n})^2}/B_p(a). \tag{3.3}$$

The flat-top averages of $b_{res}^{sec}/B_p(a)$ and τ_E have been calculated for the ensemble of discharges in Figure 3.9 and the results are plotted, as a function of α_{K_p} and α_{K_d}, in the contour plots shown in Figure 3.10. The maximum value of τ_E corresponds to the lowest value of $b_{res}^{sec}/B_p(a)$, showing that the magnetic feedback control at the edge has also an effect on the overall level of magnetic chaos in the plasma core. In other words, this beneficial effect is not limited to the decrease of the edge radial

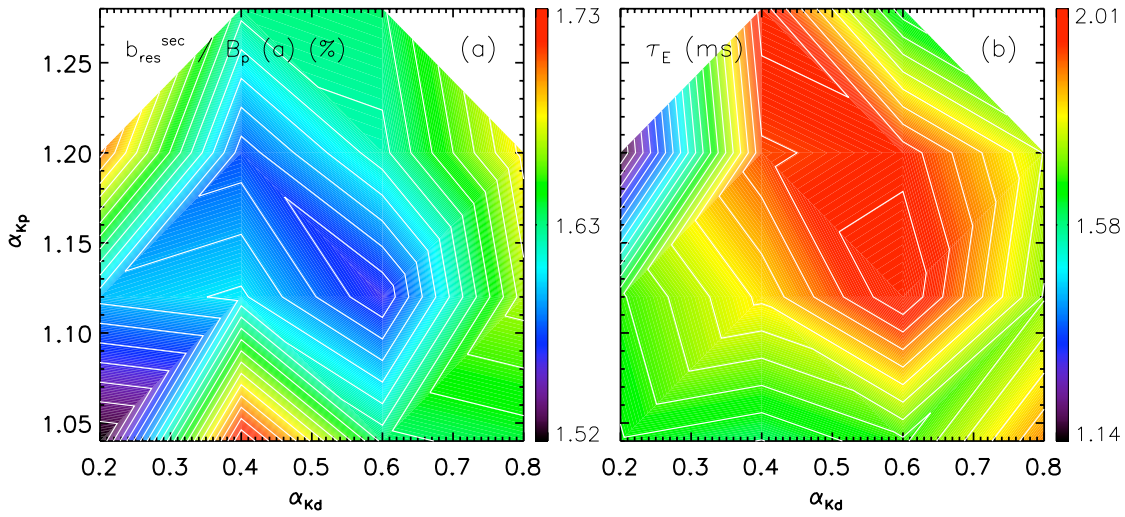

Figure 3.10: Contour plot of (a) the $m = 1$ secondary mode amplitude calculated at the resonant surface as in Equation (3.3) and (b) the energy confinement time as a function of α_{K_p} and α_{K_d}.

magnetic field amplitude, but also to lower level of magnetic field stochasticity in the plasma core.

A statistical analysis of the flat-top averages of the total normalized edge radial magnetic field amplitude, the $m = 1$ deformation of the LCFS, the locking strength parameter and the total coil current amplitude has been performed for discharges with different plasma current, comparable magnetic equilibrium and plasma density: $F \in [-0.08, -0.036]$, $n/n_G \in [0.06, 0.22]$. The results of the analysis are shown in Figure 3.11. The discharges differ in the control parameters: the black circles represent experiments which used the empirically-optimized gain set, while the red circles the model-based optimized one.

The model-based optimization of the mode controller systematically gives lower values of the total edge radial magnetic field amplitude, $b_r^{tot}/B_p(a)$, compared to the results obtained with the empirical gain set, as highlighted in 3.11(a). The

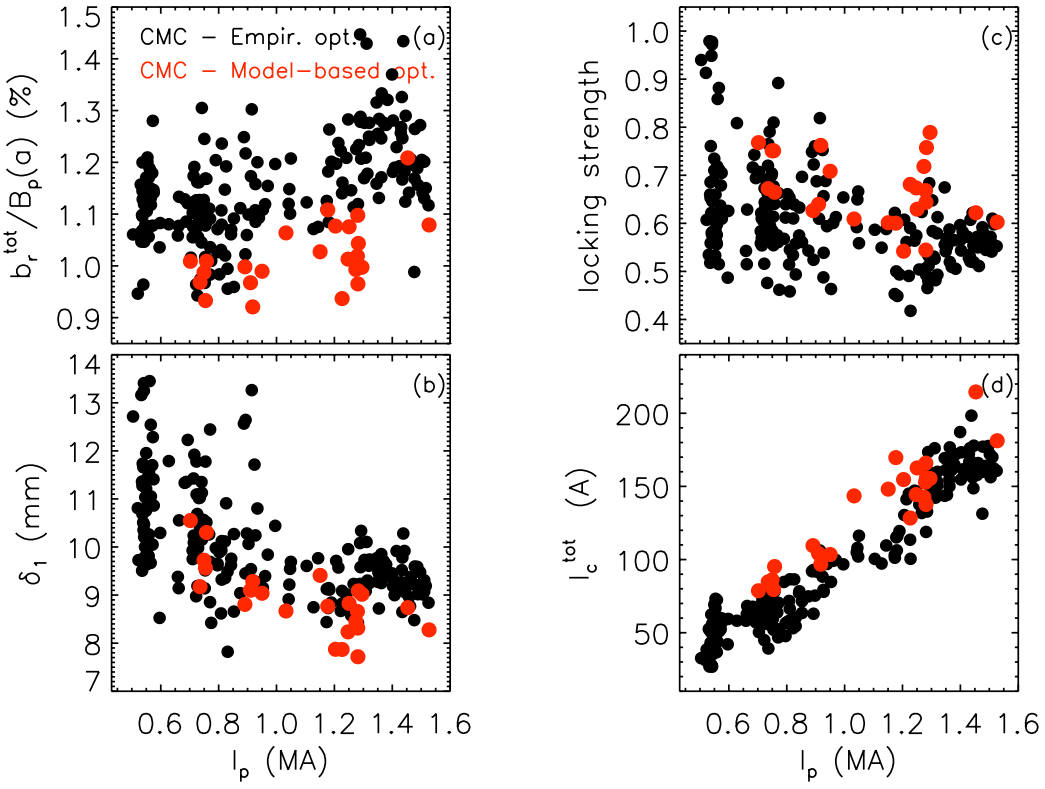

Figure 3.11: (a) Total edge radial magnetic field amplitude, (b) non-axisymmetric $m = 1$ distortion of the LCFS, (c) locking strength, and (d) total coil current amplitude for discharges with different plasma current. Discharges with empirically-optimized gains (in black) and model-based optimized gains (in red) are compared.

reduction is about 10% for plasma currents in the range $I_p \in [0.65, 0.9]MA$ and about 15% for $I_p \in [1.1, 1.3]MA$.

The reduction of the non-axisymmetric distortion δ_1 shown in Figure 3.11(b) is instead not very large and amounts to about 5% for $I_p \in [0.65, 0.9]MA$ and 7% for $I_p \in [1.1, 1.3]MA$. As suggested by the higher values of the locking strength parameter plotted in Figure 3.11(c), this is mainly due to a higher non-linear coupling between different tearing modes, which has not been optimized in the model-based approach. Moreover, the higher derivative gains used in the model-based gain set imply a faster response of the feedback coil currents. This may induce larger error fields localized near the gaps or portholes, as it will be explained more in detail in Chapters 4 and 6. These results have been achieved with an increase of the total coil current amplitude of the order of 30% for $I_p \in [0.65, 0.9]MA$ and 16% for $I_p \in [1.1, 1.3]MA$.

An accurate comparison of the energy confinement time between the empirically-optimized and the model-based optimized discharges could not be performed, since the electron temperature measurements were unfortunately not available for all the discharges in the database.

3.4.2. Effects of the optimization at high-plasma current

Even if the model-based optimization has been performed in experiments with plasma current in the range $0.8 - 1MA$, the optimal gain set has been used also in high-plasma current regimes, which have been explored in the 2010 experimental campaign reaching the maximum design point of $2MA$.

At the beginning of the high-current experimental campaign, some initial tests showed that the request of coil current for the $(1, -7)$ mode control was too high, near the saturation value when the model-based gains were used ($K_p^{m,n} = 810$ and $K_d^{m,n} = 1.1$). This is due to the fact that the edge radial magnetic field amplitude of the $(1, -7)$ mode increases as the plasma current is raised, and consequently the request of coil current to suppress this mode increases with the plasma current. Moreover, the coil current amplitude is higher with respect to a purely proportional gain when derivative gains are set in the mode controller. This aspect is highlighted in the contour plot of the $(1, -7)$ coil current amplitude suggested by the RFXlocking code, already discussed in Figure 3.7(b). To overcome the current saturation for the $(1, -7)$ control at high-plasma current, the approach used was to neglect the derivative gain on the $(1, -7)$ mode, maintaing the model-based gain values for the secondary modes.

To identify the optimal gain set for high-plasma current operations, both the empirical set and the model-based one modified as described above have been used. A comparison between the two gain sets has been performed. Figure 3.12 shows the results, in terms of flat-top averages of the total edge radial magnetic field amplitude, the non-axisymmetric $m = 1$ distortion of the LCFS, the total coil

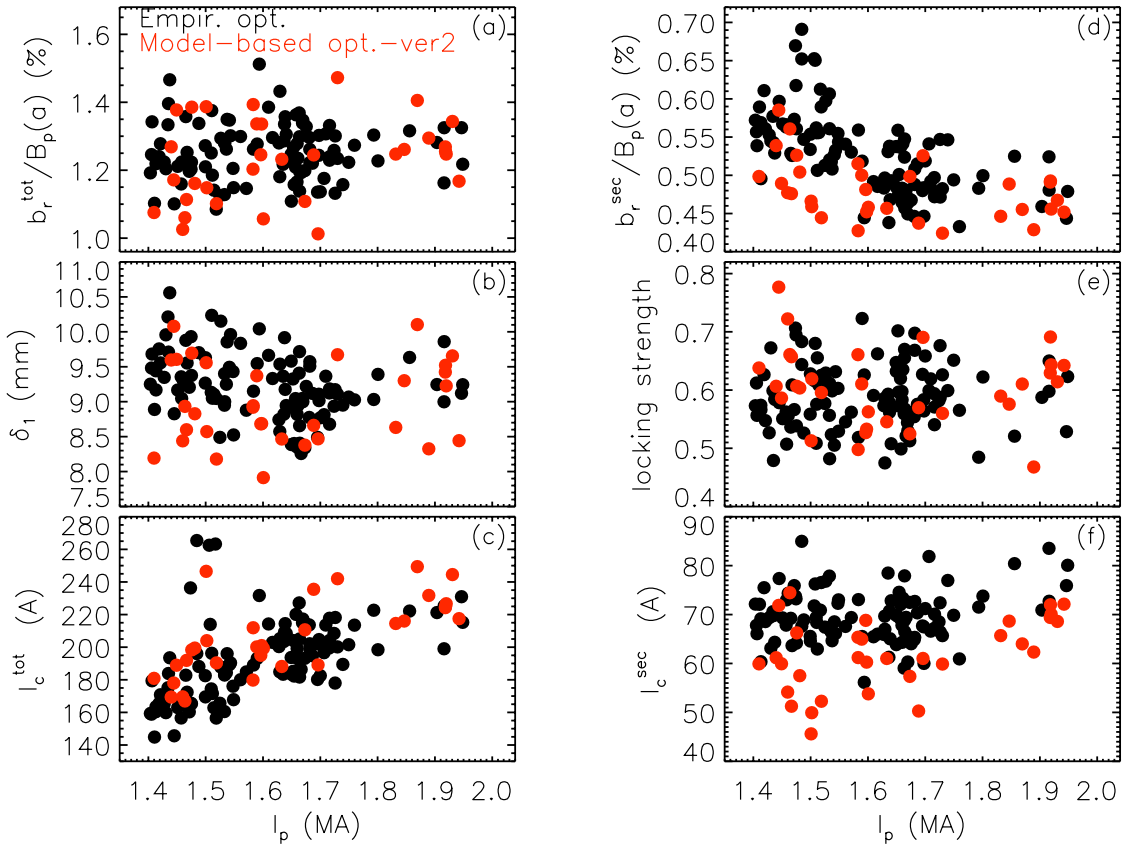

Figure 3.12: (a) Total edge radial magnetic field amplitude, (b) non-axisymmetric $m = 1$ distortion of the LCFS, (c) total coil current amplitude, (d) edge radial magnetic field amplitude of secondary modes, (e) locking strength and (d) coil current amplitude of secondary modes for an ensemble of high-plasma current experiments. Discharges with empirically-optimized gains (in black) and model-based optimized gains (in red) are compared. In the latter case, the derivative gain applied to the $(1, -7)$ mode is 0 instead 1.8.

current amplitude, the edge radial magnetic field amplitude of secondary modes defined in Equation (1.33), the locking strength, and the coil current amplitude of secondary modes, calculated as $I_c^{sec} = \sqrt{\sum_{m=1,n=-16}^{-8} (I_{coil}^{1,n})^2}$. The ensemble of analyzed discharges has high-plasma current above $1.4MA$, reversed parameter in the range between $F \in [-0.035, -0.015]$, electron density normalized to the Greenwald density $n/n_g \in [0.06, 0.22]$. The plasmas which used the empirical gain set are plotted in black, the new model-based one in red.

As shown in Figures 3.12(a) and (b) and (c), the values of $b_r^{tot}/B_p(a)$, δ_1, and I_c^{tot} for both sets are comparable. The difference among them is visible if one

considers the variation of the edge radial magnetic field amplitude of the secondary modes in the two sets. This quantity, plotted in Figure 3.12(d), seems lower for the discharges with the new model-based set, especially in the range of plasma current $I_p \in [1.4, 1.6]MA$. As a result, the requested feedback coil current on the secondary modes is lower, as shown in Figure 3.12(f).

The statistics of the locking strength parameter of high-plasma current discharges differs from the result found before and shown in Figure 3.11(c). In this Figure, the locking strength values of the model-based discharges are higher than the empirical set ones. Instead, at high-plasma currents the locking strength is comparable among the two sets, as highlighted in Figure 3.12(e). As mentioned before, discarding the derivative gain on the $(1, -7)$ mode, error fields possibly induced by the fast feedback action in presence of the $3D$ wall structures may be reduced and thus do not enhance the phase-locking among tearing modes.

In summary, based on this analysis it may be argued that in high-current plasmas the new model-based set is recommended with respect to the empirical one. Even if the differences between the two gain sets are not so significant, the new model-based set is able to further reduce the edge radial magnetic field amplitude of the secondary modes with respect to the empirical set. Consequently the request of coil current for secondary mode control is lower.

Despite some stringent hypotheses, for example a uniform wall structure, the RFXlocking code is able to reproduce the non-linear dynamics of multiple tearing modes. This Thesis work shows that this model is a powerful tool to optimize offline the feedback gains. This has the big advantage of saving experimental time.

To further optimize the mode feedback controller, some modifications of the RFXlocking code could be useful. For instance, the presence of non-uniformities of the wall structure, such as portholes and gaps, is not taken into account in the code. The 3D wall structure could modify the dynamic properties of the field penetration inside the wall, the non-linear coupling between different modes, and thus the tearing mode dynamics. Since the harmonics of the main error fields, due to the non-uniform penetration of various magnetic fields through the toroidal and poloidal gaps of the wall structure, have been identified, as will be described in Chapters 4 and 6, future work may consist in introducing these spurious harmonics in the model and analyzing their impact on the mode dynamics.

CHAPTER 4

Dynamic decoupling and multi-mode magnetic feedback for error field correction in RFX-mod

In this Chapter, one of the main sources of magnetic field errors in the RFX-mod experiment will be described, together with the control strategies that have been developed to compensate them. Error fields in RFX-mod are induced by 3D wall structures that introduce significant couplings among the plasma modes, affecting their stability and the feedback performance. The main error fields are due to the non-uniform penetration of the vertical magnetic field through the wall gaps, during the plasma current ramp-up phase. The correction scheme used to compensate these error fields combines pre-programmed current waveforms and multi-mode magnetic feedback, similarly to what done in tokamaks. The pre-programmed currents are computed with a dynamic decoupling algorithm, which accounts for the mutual interaction between different feedback coils and magnetic sensors modified by the dynamic response of the 3D wall structure. At the same time, multi-mode magnetic feedback is applied to the main error field harmonics. The results are encouraging: with error field correction, a significant reduction of the error field amplitude has been obtained and the tearing modes are no more phase-locked at a preferred toroidal angle, which is beneficial for the machine operation at high-plasma current.

4.1 Effects of 3D wall structures

In any magnetic fusion device, the wall surrounding the plasma can not be considered as uniform. It always presents complicated 3D structures, such as large portholes for diagnostics and auxiliary heating or current drive systems, coil feeds, gaps to allow the penetration of magnetic fields, and other features. Any magnetic field perturbation varying in time, such as that shown in the scheme in Figure 4.1, induces in the wall eddy-currents. In presence of 3D structures the pattern of eddy-currents is modified, giving rise to magnetic field errors that can be then amplified or shielded by the plasma.

Considering the frequency-response of the wall is particularly important in experiments dedicated to the feedback control of plasma instabilities by active coils. Modeling of the plasma stability with realistic wall and magnetic feedback finds that the plasma stability is significantly modified when 3D wall structures are taken into account. For example, the RWM growth rates tend to increase when gaps or holes are present in the wall, as confirmed also by comparison with the experiment in RFX-mod [86]. The 3D wall structures also tend to couple modes with different helicities, as predicted by [87]. All these effects may have consequences on the choice of the feedback control logic and on the design of the entire feedback system (number, shape, and position of the coils, bandwidth of the power supplies, etc.).

Such effects are dynamic in nature, depending on the characteristic frequency of the external magnetic field. Including them in a feedback scheme requires a very good knowledge of the eddy-current patterns induced in the wall, which can be obtained for istance by detailed electromagnetic (e.m.) modeling of the wall, coupled to a model of the plasma stability, as in the work done with the VALEN [88], CARMA [89, 90], or STARWALL [87] codes. Another approach is to measure in dry shots the e.m. couplings between the various external magnetic field sources, such as feedback and axisymmetric coils, and a sufficiently extended set of magnetic field sensors, as done for example in the RFX-mod experiment [91].

Commonly these e.m. couplings are expressed in terms of a transfer function in the frequency domain. The transfer function is a complex function of frequency, which describes the magnetic field at the sensor as a function of the current applied in the coil, and can be expressed as:

$$TF(\omega) = Y(\omega)/S(\omega), \tag{4.1}$$

where $Y(\omega)$ is a complex function which represents the measured magnetic flux, $S(\omega)$ the input coil current. Typically these functions can be chosen as complex polynomials.

In this Thesis work, the effects of the frequency response of the RFX-mod wall on the generation of error fields and on the plasma performance has been investigated in two cases: when the vertical magnetic field is applied to center the plasma

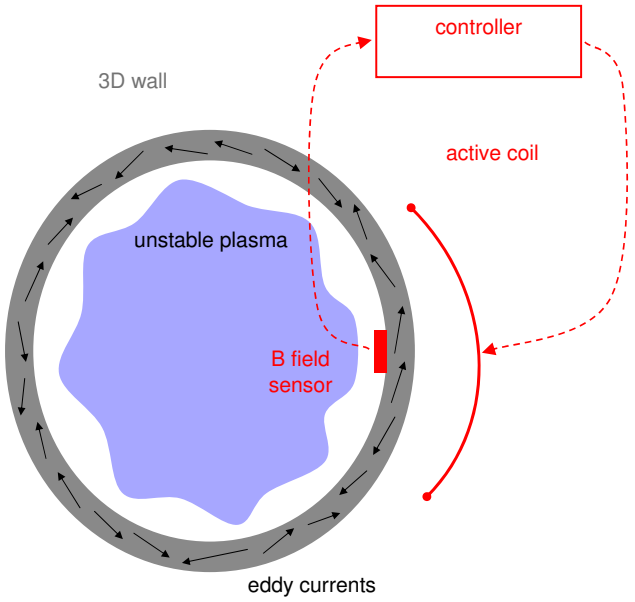

Figure 4.1: Schematic picture of a plasma, represented in violet, with the magnetic feedback system (magnetic field sensor, active coil, and controller). The 3D wall is plotted as a grey ring. Any magnetic field perturbation induces eddy-currents in the wall, plotted as arrows, whose pattern can be modified if the wall has 3D structures, such as gaps and portholes. In this case, magnetic field errors are induced.

in the current ramp-up phase (Chapter 4) [43] and when external magnetic fields applied with the feedback coils are used to sustain helical equilibria in RFX-mod (Chapter 6) [45]. In both cases, the presence of the $3D$ structures induces error fields that can enhance plasma-wall interaction phenomena and degrade the energy confinement time. As will be described in this Chapter sophisticated feedback schemes have been applied to correct them.

The wall dynamic response has been investigated also in the DIII-D tokamak [45, 66]. In this experiment, external magnetic fields, such as those induced by the feedback and field-shaping coils, are subtracted in real-time from the magnetic field measurements. The magnetic fields external to the plasma are computed from the static couplings between each actuator and sensor. In this way, the frequency-dependent couplings, due to eddy-currents induced in the wall, are neglected. The relevance of such effects for RWM control and error field correction has been analyzed and this work is described in Chapter 7.

4.2 Error fields in the current ramp-up phase

As described in Section 4.1, the presence of $3D$ wall structures, such as poloidal gaps in the wall, modify the pattern of eddy-currents induced in the wall by any magnetic field varying in time, thus forming localized error fields. In the RFX-mod experiment, the main error fields are produced during the current ramp-up phase of the discharge, when, in few tens of milliseconds, the plasma current achieves its flat-top value that can reach up to $2MA$. In this phase, the vertical magnetic field necessary to maintain the plasma centered in the torus varies on a time scale of the order of τ_w, as shown in Figure 4.2(a), and penetrates faster where the boundary is not uniform thus giving rise to error fields localized at these positions.

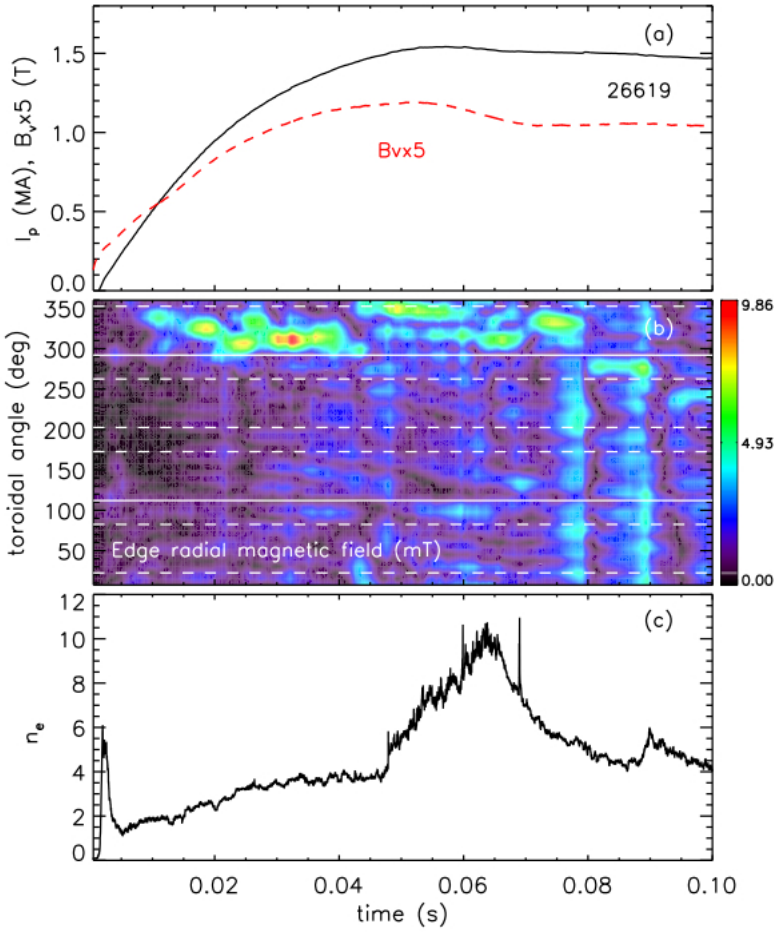

Figure 4.2: (a) Plasma current (black) and vertical magnetic field (dashed red line) during the current ramp of discharge 26619. (b) Contour plot of the radial magnetic field as a function of the toroidal angle and time. The horizontal continuous lines in the panel indicate the two poloidal gaps, while the dashed lines the toroidal angle of some large portholes. (c) Electron plasma density.

The effects of these error fields on the plasma performance are reported in Figures 4.2(b) and (c). The phase-locking among the various unstable tearing modes is not toroidally uniform in the first $100ms$ of the plasma discharge, but it is localized near the poloidal gap at $\phi = 292.5°$, where the error fields grow, as shown in the contour of the radial magnetic field plotted as a function of time and toroidal angle in Figure 4.2(b). As anticipated in the previous Chapter, these events are associated with strong plasma-wall interaction, which heats locally the wall and can cause the release of Hydrogen and impurities, such as Carbon and Oxygen, from the graphite tiles. As a result, the plasma density in some cases can increase in an uncontrolled way, as shown in Figure 4.2(c). During these events the plasma resistance increases and the confinement is severely deteriorated.

A careful analysis of the error field pattern during the current ramp-up phase has been carried and the results are shown in Figure 4.3. The contour plot of the radial magnetic field at the beginning of the current ramp, at $t = 0.002s$, is shown in Figure 4.3(b) as a function of the poloidal and toroidal angles. The error field is clearly localized at the two poloidal gaps at $\phi = 112.5°$ and $\phi = 292.5°$, and peaks

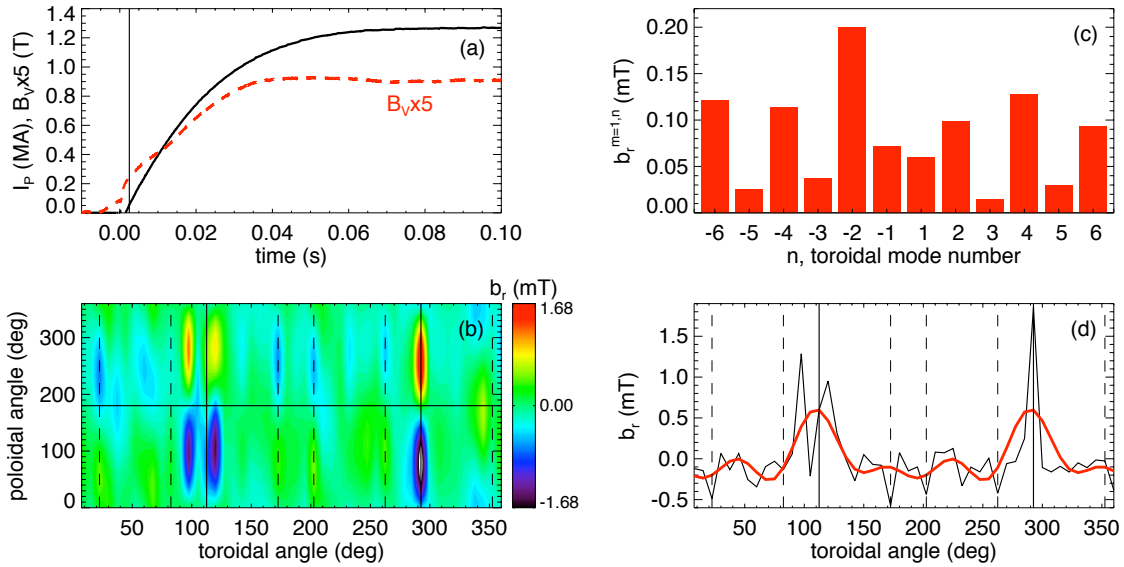

Figure 4.3: (a) Plasma current (black) and vertical magnetic field (dashed red line) during the current ramp of discharge 26135. (b) Contour plot of the radial magnetic field at $t = 0.002s$ from 4×48 sensors. (c) Radial magnetic field amplitude of the $m = 1, n$ harmonics corresponding to the magnetic field pattern in panel (b). (d) Radial magnetic field at $t = 0.002s$ as a function of the toroidal angle at poloidal angle $\theta = 90°$ (black) and same quantity computed summing the $m = 1, n = \pm 2, \pm 4, \pm 6$ harmonics only (red thick line). The vertical continuous lines in panels (b) and (d) indicate the two poloidal gaps, the horizontal one the toroidal gap. The vertical dashed lines indicate the toroidal angle of some large portholes.

at the top, $\theta = 90°$, and bottom, $\theta = 270°$, of the machine. The error field at the gap at $\phi = 112.5°$ has also a fine structure with two distinct peaks a few degrees apart. This is due to the particular structure of this gap, where the copper shell is not simply cut, but it has an overlap of 23° in the toroidal direction, as described in [23]. Other peaks with smaller amplitude are localized at the toroidal positions of some large portholes, indicated in Figure 4.3(b) with vertical dashed lines.

For a chosen operational scenario, the error fields described above and their time evolution are fairly reproducible. Due to the spatial symmetries of the error field highlighted above, its Fourier spatial spectrum is dominated by a few harmonics, with $m = 1, n = \pm 2, \pm 4, \pm 6$, as shown in Figure 4.3(c), where the $m = 1$ mode amplitudes, obtained by Fourier decomposing the radial magnetic field in Figure 4.3(b), are plotted as a function of the toroidal mode number.

Figure 4.3(d) compares the radial magnetic field at the same time instant, $t = 0.002s$, as a function of the toroidal angle and at fixed poloidal angle $\theta = 90°$, with the same quantity computed summing the $m = 1, n = \pm 2, \pm 4, \pm 6$ harmonics only. This confirms that the largest part of the error fields, localized at the poloidal gaps, is due to these harmonics. Higher toroidal mode numbers represent instead the error field fine structure. Note that the main error field harmonics fall within the RWM spectrum, which corresponds to $m = 1, -6 \leq n \leq 6$, and are thus amplified to some extent by the response of the plasma, similarly to what already observed in the Extrap-T2R experiment [92]. This aspect will be discussed at the end of this Chapter.

The temporal evolution of the main error field harmonics identified above is shown in Figure 4.4. The amplitude of the $m = 1, n = \pm 2, \pm 4, \pm 6$ harmonics increases as long as the vertical magnetic field varies in time and decreases to very low values during the discharge flat-top. It is interesting to note that the initial increase of the error field harmonics in the time interval from 0 to $0.01s$ is much faster than the resistive penetration time of the wall of about $0.05s$. A simple proportional feedback controller on these low-n harmonics would not be able to counteract such a fast dynamics, since its action would be shielded on these fast time scales by the resistive wall. A dynamic decoupler that includes information on the wall dynamic response and compensates for it is necessary in this case, as it will be demonstrated in the next Section.

4.3 Error field correction schemes developed in RFX-mod

The scheme developed in this Thesis work to correct the error fields due to the non-uniform penetration of the vertical magnetic field through the poloidal gaps combines two parts, similarly to what done also in other machines [56, 93, 94]: pre-programmed current waveforms calculated offline, based on the average evolution of the error field, to correct the most reproducible part of the error field, plus active feedback on selected harmonics, to correct the residual error fields due to small

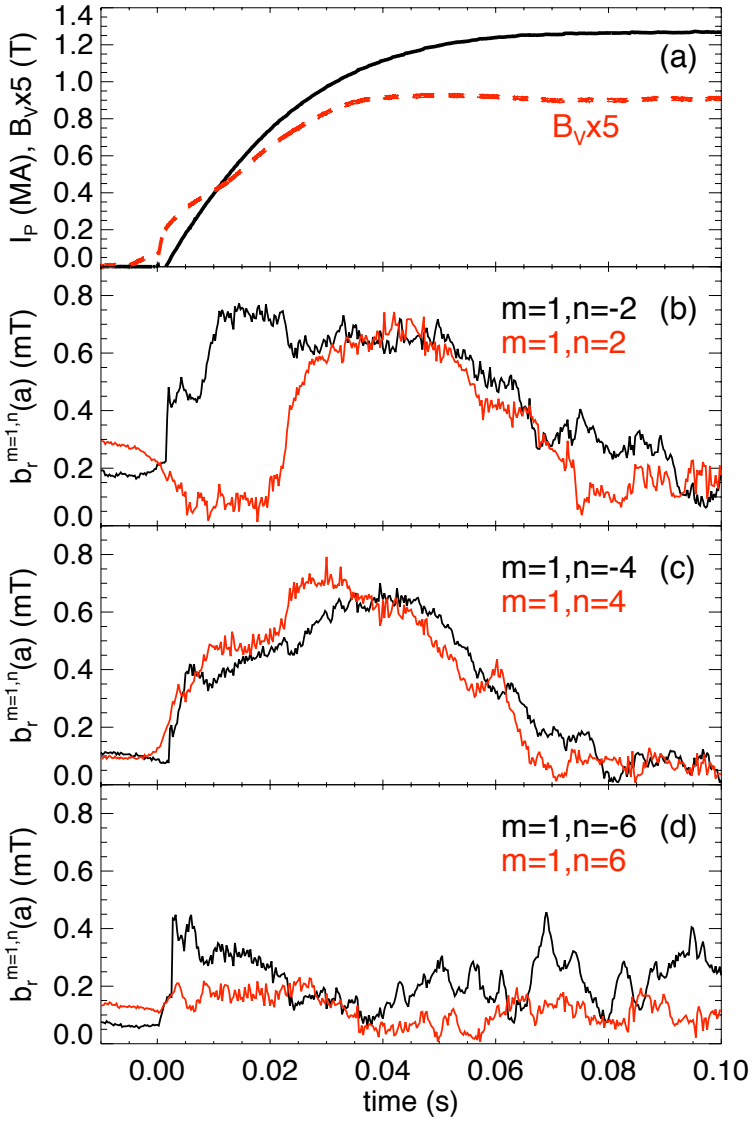

Figure 4.4: (a) Plasma current (black) and vertical magnetic field (dashed red line) during the current ramp of discharge 26135. (b)-(d) Temporal evolution of the main $m = 1$ error field harmonics.

shot-to-shot variations. In the following a detail description of the two techniques will be provided.

4.3.1. The dynamic decoupler

As mentioned in Section 4.1, an experimental approach that can be used to identify the wall-frequency response to any time-varying magnetic field consists in

measuring the e.m. couplings between each actuator and sensor. This was done in RFX-mod during an extensive dry-shot campaign, in which various active coils have been fed with a sinusoidal current waveform with frequency in the range $\omega \in [10 - 200]Hz$ [95]. Due to the large number of active coils in the RFX-mod feedback system, the wall frequency response has been identified by feeding active coils in standard zones without "special" features in the wall structure, and near the poloidal gaps and large portholes.

A typical example of transfer function between the active coil at $\phi = 195°$, $\theta = 270°$ and the radial field sensor at $\phi = 195°$, $\theta = 270°$ is reported in Figure 4.5. The red circles are the experimental data transfer function, while the blue points represent the fit calculated with a MATLAB toolbox routine called PEM, acronymous of Polymath-Excel-Matlab [96]. Given as input the estimated amplitudes, phases and frequencies of the e.m. couplings, the PEM calculates the fit using an iterative minimization error method. The fit represents a 1 pole transfer function.

Vacuum field analyses reveal that when a current flows in a some active coil, not only the correspondent radial magnetic field sensor senses the magnetic field, but of course also the nearby ones. This is highlighted in Figure 4.6, where the amplitudes and phases of the mutual inductances relative to active coil at $\phi = 120°$, $\theta = 90°$ are shown as a function of frequency. The relative numbering has been used to distinguish the different couplings: (0,0) represents the transfer function between the active coil at $\phi = 120°$, $\theta = 90°$ and the corresponding radial field sensor at $\phi = 120°$, $\theta = 90°$, while $(0, 1)$ stands for the mutual coupling between the active coil at $\phi = 120°$, $\theta = 90°$ and the adjacent radial field sensor, at $\phi = 127, 5°$, $\theta = 90°$, and so on. As shown in Figure 4.6, the values of the couplings at $0Hz$ differ for each sensor-actuactor couple since they depend on the geometry and relative position. It can be noticed that increasing the frequency, the coupling with the opposite $(0, 2)$ and the toroidally not adjacent $(\pm 2, 0)$ sensors becomes more important. This can be explained considering the presence of "special" features in the wall structure: the shell overlapped edges and the inner equatorial gap. In this case, the pattern of eddy-current induced in the wall is modified by these 3D wall structures, introducing frequency-dependent couplings.

To compensate for the couplings between each active coil and each radial field sensor, a dynamic pseudo-decoupler has been developed for RFX-mod [98]. The algorithm is based on a matrix of 192×192 frequency-dependent transfer functions, $\mathbf{M}(j\omega)$, which describes the frequency response of the wall to any external magnetic field which varies in time. The matrix $\mathbf{M}(j\omega)$ is represented as:

$$\mathbf{M}(j\omega) = \begin{bmatrix} M_{0,0}(j\omega) & M_{0,1}(j\omega) & .... & M_{0,192}(j\omega) \\ M_{1,0}(j\omega) & M_{1,1}(j\omega) & .... & M_{0,192}(j\omega) \\ ... & ... & M_{2,2}(j\omega) & .... \\ M_{192,0}(j\omega) & .... & .... & M_{192,192}(j\omega) \end{bmatrix}, \qquad (4.2)$$

where the diagonal terms represent the transfer functions between each actuator

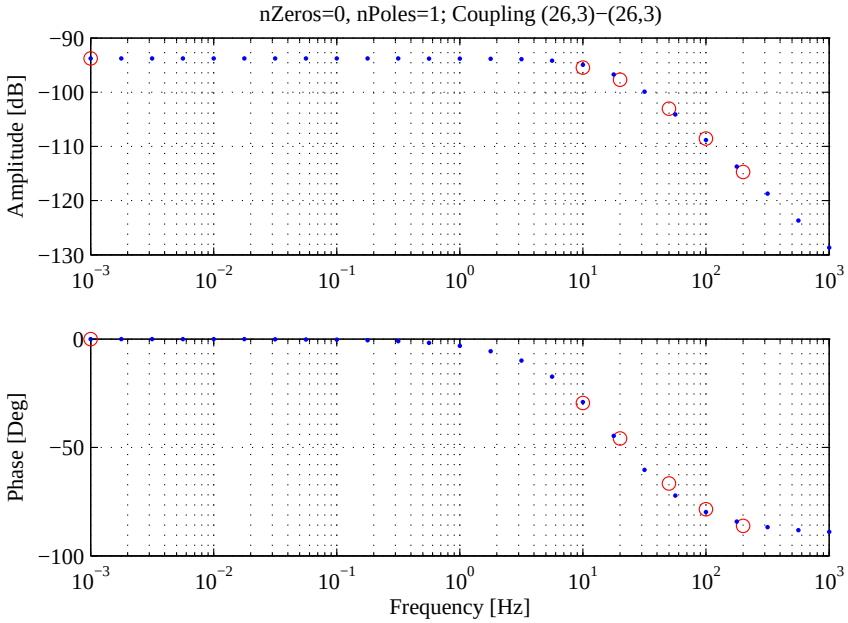

Figure 4.5: Transfer function between an active coil and the corresponding radial field sensor. The model PEM prediction is shown with blue points, the measurements with red circles (this picture has been taken from [97]).

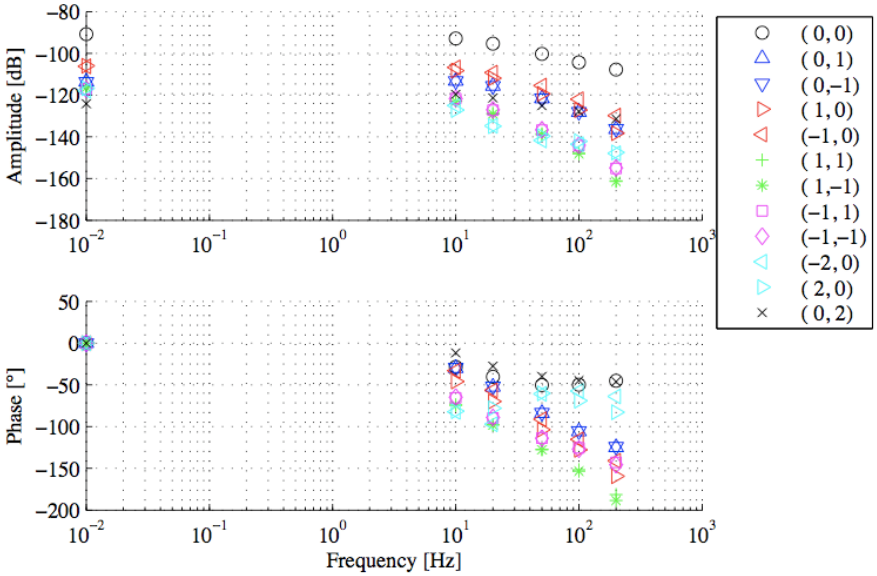

Figure 4.6: Mutual couplings between the coil at the position $\phi = 120°$, $\theta = 90°$ and nearby radial magnetic field sensors (this picture has been taken from [97]).

and the respective sensor, while the off-diagonal terms those between the same actuator and all the other sensors.

The coil currents needed to produce a particular magnetic field pattern at the sensors, $\mathbf{B}(t)$, can in principle be obtained by multiplying the field by the inverse of the coupling matrix, $\mathbf{I}(t) = \overleftrightarrow{\mathbf{M}}^{-1} \cdot \mathbf{B}(t)$, as it has been discussed in [98]. Since the $\mathbf{M}(j\omega)$ matrix is not full rank, and thus it is not invertible, a pseudo-inversion of $\mathbf{M}(j\omega)$ was done, using singular value decomposition method, hence the name pseudo-decoupler [98].

This tool has been used in this Thesis work to correct the error fields that grow in the current ramp-up phase of the plasma discharge. As mentioned before, for a chosen plasma ramp-up phase scenario the error fields pattern is highly reproducible, thus the mean error field spatial pattern given in input to the decoupler can be computed by averaging several similar discharges. Then the dynamic decoupler computes pre-programmed currents needed to compensate the error fields.

While the error field spatial shape is assumed to be fixed, the temporal evolution of its total amplitude, defined here as the sum of its main harmonics:

$$b_r^{EF} = b_r^{1,2} + b_r^{1,-2} + b_r^{1,4} + b_r^{1,-4} + b_r^{1,6} + b_r^{1,-6}, \tag{4.3}$$

is approximated by a linear fit, represented with a red dashed line in Figure 4.7(a) during the first fast rising phase of the error field from -0.005 to $0.03s$. The current waveforms computed by the dynamic decoupler are shown in Figure 4.7(b) as a function of time and in Figure 4.7(c) as a function of the poloidal and toroidal angles at $t = 0.002s$. The radial magnetic field produced by these currents has been measured in a vacuum discharge and is shown in Figure 4.7(d). It spatial pattern matches very well the error field pattern shown before in Figure 4.3(b).

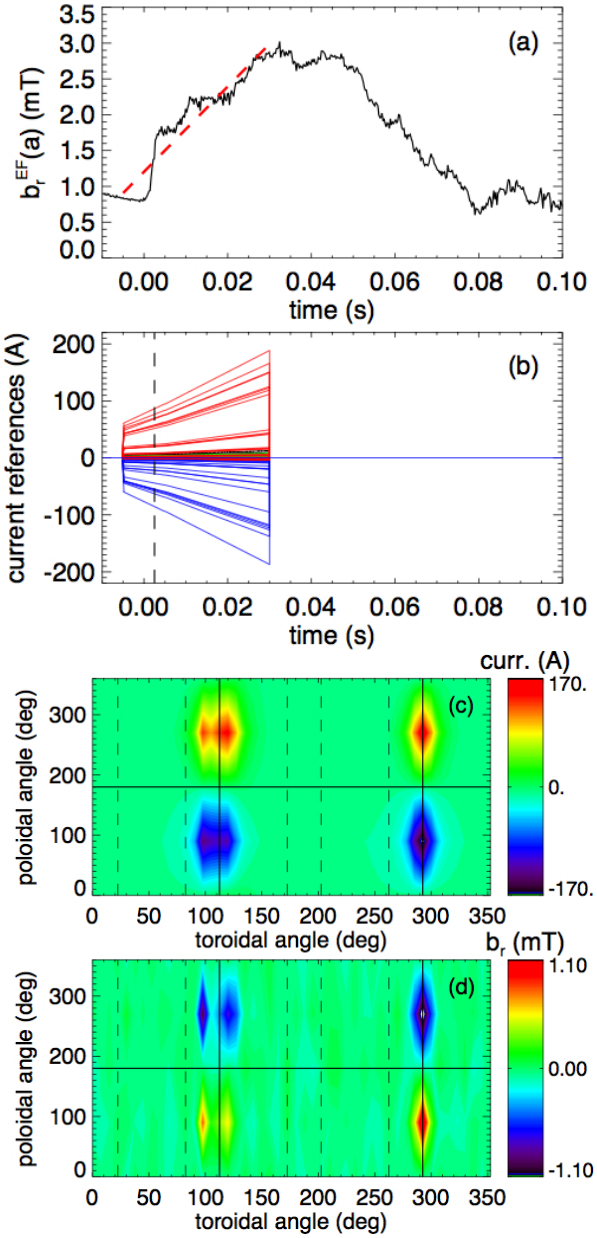

Figure 4.7: (a) Error field total amplitude in discharge 26135 as defined in Equation (4.3) (black) and linear fit in the interval $[-0.005, 0.03]s$ (red dashed line). (b) Current waveforms for all 192 feedback coils calculated by the dynamic decoupler as explained in the text and (c) contour plot of the same signals at $t = 0.002s$. (d) Contour plot of the radial magnetic field produced in a vacuum shot by the currents in the previous panels at $t = 0.002s$. The vertical continuous lines in panels (c) and (d) indicate the two poloidal gaps, the horizontal one the toroidal gap. The vertical dashed lines indicate the toroidal angle of some large portholes.

4.3.2. Multi-mode control of the main error field harmonics

Another error field correction scheme tested in this Thesis work is to apply magnetic feedback to the main error field harmonics identified before with $m = 1, n = \pm 2, \pm 4, \pm 6$. The optimal gains for each harmonic have been calculated with a Simulink model of the RFX-mod magnetic feedback system [91, 95]. This simulates the RFX-mod magnetic feedback loop with realistic parameters for the controller, the active coils, and the sensors, including saturations, delays, and a simplified model of the power supplies. The frequency-dependent couplings between the coils and the sensors are measured in vacuum and are the same used for the dynamic decoupler.

Simulations have been performed varying the proportional, derivative, and integral gains, searching for the values that allow the largest reduction of the main error field harmonics within the stability boundaries of the feedback loop. The best error field correction is obtained with high enough purely proportional gains, whose values are indicated for each harmonic in Table 4.1.

Adding an integral gain would help in further reducing the error field, but it also introduces unwanted oscillations when the error field naturally goes to zero during the flat-top. The problem is well known and is called integral windup [99]. It may be solved with dedicated anti-windup schemes, which were beyond the scope of the present work. A derivative gain is found to slightly improve the feedback performance in the present case, but it tends at the same time to amplify the noise present in the radial magnetic field measurements. For these reasons only proportional gains are used in the experiments considered in the following.

The simulated proportional gain scan is reported in Figure 4.8. This shows the maximum radial magnetic field amplitude of the $(1, -2)$ error field harmonic and the maximum coil current on the same harmonic as a function of the proportional gain. The $(1, -2)$ amplitude decreases as a function of the proportional gain up to a point where the feedback loop becomes unstable. The proportional gain used in the experiment, indicated with a vertical dashed line in Figure 4.8, was chosen to be sufficiently far from the feedback loop instability and well below the maximum available coil current of $320A$.

Similar scans have been performed for the other main error fields harmonics, and the trends of the edge radial magnetic field amplitude and the maximum requested coil current as a function of the proportional gain are very similar to the one reported in Figure 4.8.

m,n	$1, \pm 2$	$1, \pm 4$	$1, \pm 6$
K_p	2200	2000	800

Table 4.1: Proportional gains applied to the main error field harmonics.

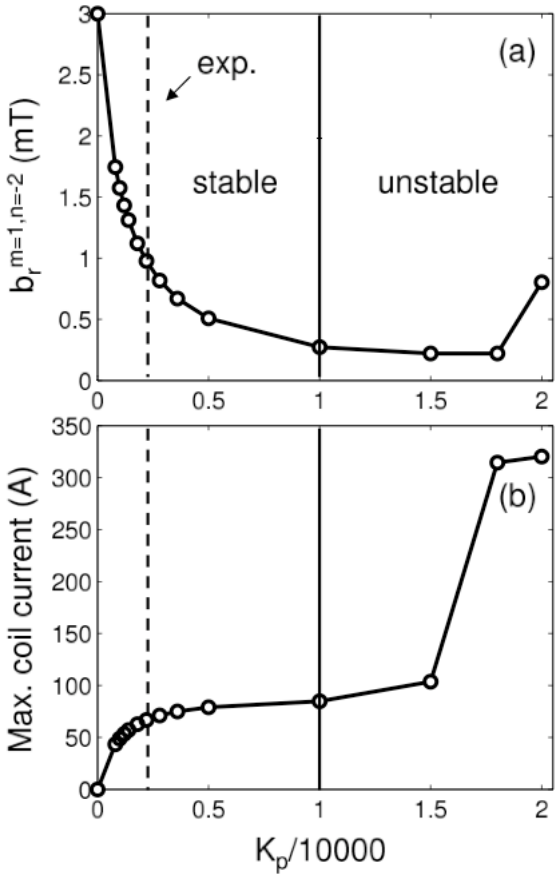

Figure 4.8: (a) Radial magnetic field amplitude of the $(1, -2)$ radial magnetic field harmonic and (b) maximum coil current on the same harmonic as a function of the proportional gain from the Simulink simulations of the feedback loop described in the text. The continuous line indicates the proportional gain above which the feedback loop becomes unstable. The dashed line indicates the proportional gain used in the experiment.

4.4 Error field correction experiments

To identify the best control strategy to correct the main error fields in RFX-mod, the two error field control schemes described in the previous section have been tested with plasma and the main results are reported in Figure 4.9. In this Figure, four similar discharges with different control settings are plotted. Figure 4.9(b) shows the temporal evolution of the total error field amplitude b_r^{EF}, defined in Equation (4.3), for these four cases. In black a case with no error field correction (i.e. without pre-programmed currents and insufficient proportional gains) is shown, showing the evolution of the error field during the current ramp-up similar to that already described in Figure 4.4. The green line corresponds to a case with feedback control only. In this case, it is evident that, without dynamic decoupling,

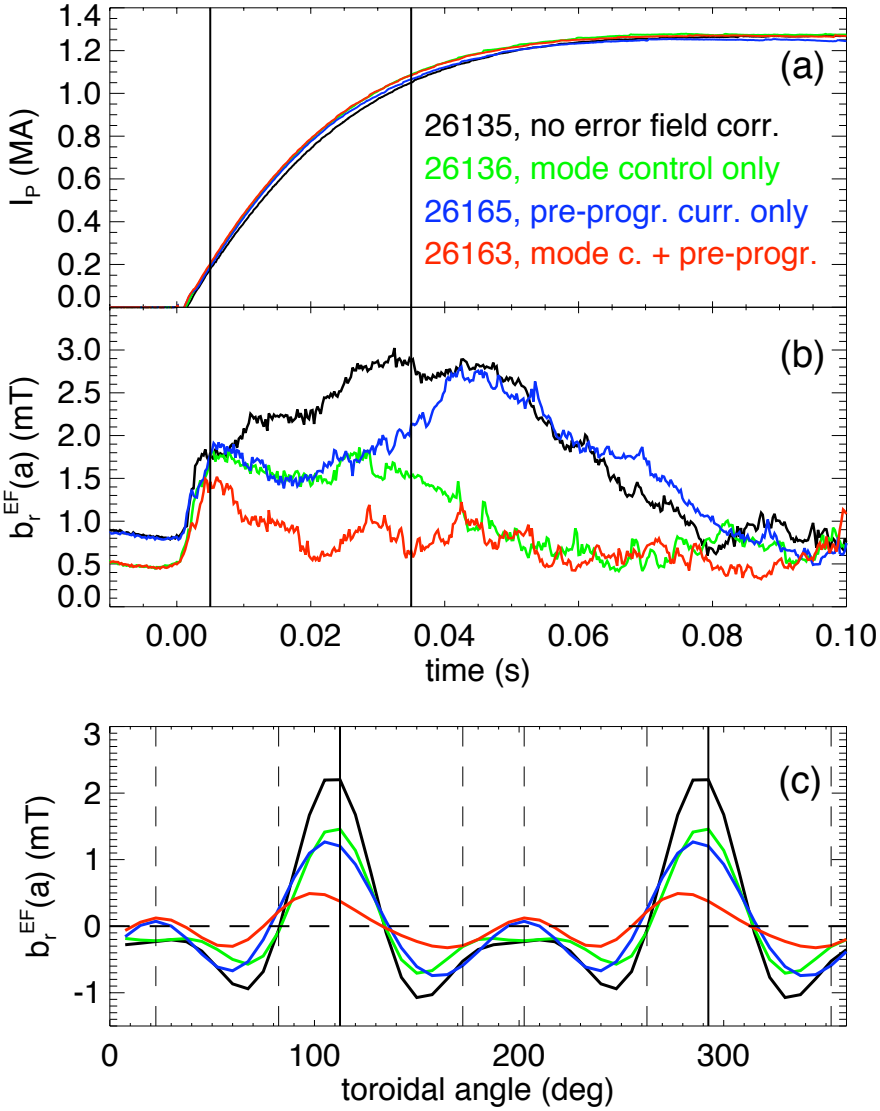

Figure 4.9: (a) Plasma current, (b) total error field amplitude as defined in Equation (4.3), and (c) the same quantity averaged in the interval $[0.005, 0.035]s$ as a function of the toroidal angle and at the fixed poloidal angle $\theta = 90°$. Four similar discharges with different error field correction settings are compared: no error field correction (black), only mode control on the main error field harmonics (green), only pre-programmed currents (blue), and the combination of these two correction approaches (red). The vertical lines in panel (c) indicate the poloidal gaps and portholes positions as in the previous figures.

feedback alone is not fast enough to correct the error field in the first tens of ms, due to the rather long resistive diffusion time of the wall, which amounts to about $0.05s$ for these low-n error field harmonics. In blue a discharge is shown with only the decoupler pre-programmed currents applied from -0.005 to $0.03s$. The red waveform represents the case where the combination of feedback and the decoupler is used. Note that in this case the error field is reduced to very low values during the whole current ramp. A residual error field of about $1mT$ remains, which may be due to approximations of the decoupler and/or to other error field sources not yet identified.

The radial magnetic field from the main error field harmonics b_r^{EF} is shown for the four cases described above in Figure 4.9(c) as a function of the toroidal angle at poloidal angle $\theta = 90°$ and time-averaged in the interval $[0.005, 0.035]s$. This analysis confirms that the combination of pre-programmed currents and feedback effectively reduces the radial magnetic field associated with the error field at all angles.

4.4.1. Main effects of error field correction on the plasma

Reducing the error fields during the current ramp-up phase of the plasma discharge has an effect on how tearing modes lock to the wall. As introduced in Section 4.1, in this phase of the discharge, these modes tend to be phase-locked and produce a toroidally-localized deformation of the plasma column [100, 101, 102]. The phase-locking is reinforced by toroidally-localized error fields, as in the plasma experiment presented in Figure 4.2, in which the plasma-wall interaction localized near a poloidal gap is responsible for the uncontrolled increase of the plasma density.

Without error field correction, the $m = 1$ deformation of the plasma boundary and presumably also the associated plasma-wall interaction happen preferentially near one of the two poloidal gaps. This is shown in Figure 4.10, which reports the probability distribution function of the toroidal angle where the tearing modes are phase-locked during the current ramp-up phase, both with (in red) and without (in black) error field correction. This analysis has been carried out for a set of discharges with plasma current in the range $I_p \in [0.6 - 1.7]MA$ and reversal parameter $F \in [-0.045, -0.025]$.

With error field correction, the tearing modes are no more phase-locked at a preferred toroidal angle, which is beneficial for the machine operation, since the plasma-wall interaction is spread around the torus, avoiding strong thermal load in localized regions of the wall and the consequent release of particles from the graphite tiles. The error field correction approach developed in this work may have positive effects on the discharge performance, even more in the high-current plasmas planned for the near future in RFX-mod, which has recently reached the design value of $2MA$.

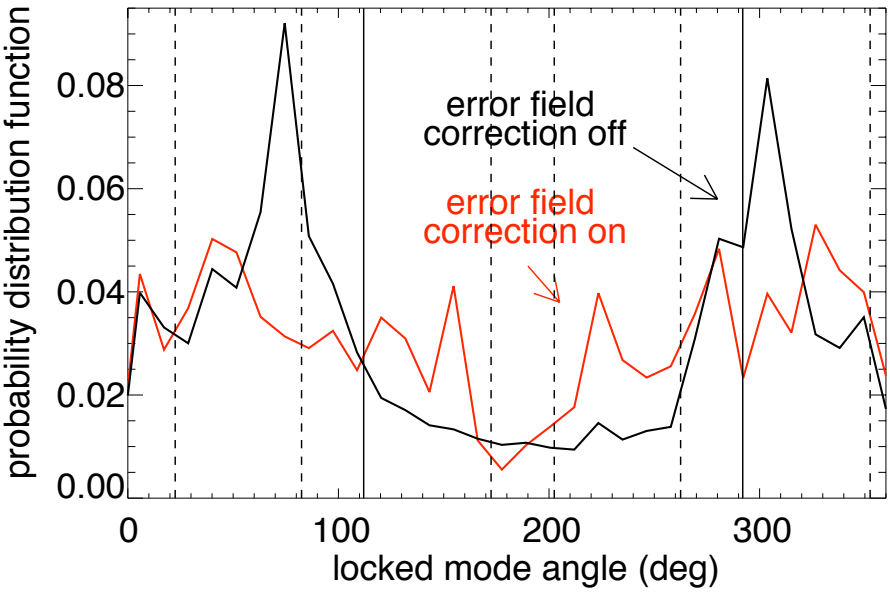

Figure 4.10: Distributions of the toroidal angle where the $m = 1, n < -7$ tearing modes are phase-locked during the current ramp-up phase in the interval $[0.005, 0.035]s$ for two sets of discharges, 192 without (black) and 65 with error field correction (red). The vertical continuous lines indicate the two poloidal gaps. The vertical dashed lines indicate the toroidal angle of some large portholes.

4.4.2. Plasma response to the main error field harmonics

As mentioned in Section 4.2, the main error field harmonics fall within the spectrum of unstable or marginally stable RWMs in RFX-mod. Hence the error field may be amplified by the plasma response, as observed in the Extrap-T2R RFP [92]. In this case, an error field of about $2G$ is induced by machine asymmetries, such as the return leg of the iron core and the two opposite poloidal gaps, and is amplified by the plasma through a RFA effect.

A phenomenon similar to the one observed in Extrap-T2R RFP happens in RFX-mod. The radial magnetic field at the resonant radius of the main error field harmonics has been calculated by solving the Newcomb's equation with edge boundary conditions taken from the experiment, as explained for example in [71]. This quantity represents the response of the plasma to the external perturbation, in this case from a marginally stable RWM.

An example of this analysis is reported in Figure 4.11. The radial magnetic field eigenfunction of the $(1, -2)$ harmonic is shown in Figure 4.11(a) as a function of radius and time. As soon as the $(1, -2)$ amplitude of the error field harmonic decreases, which happens at $t \approx 0.06s$ in this case, the response of the plasma is

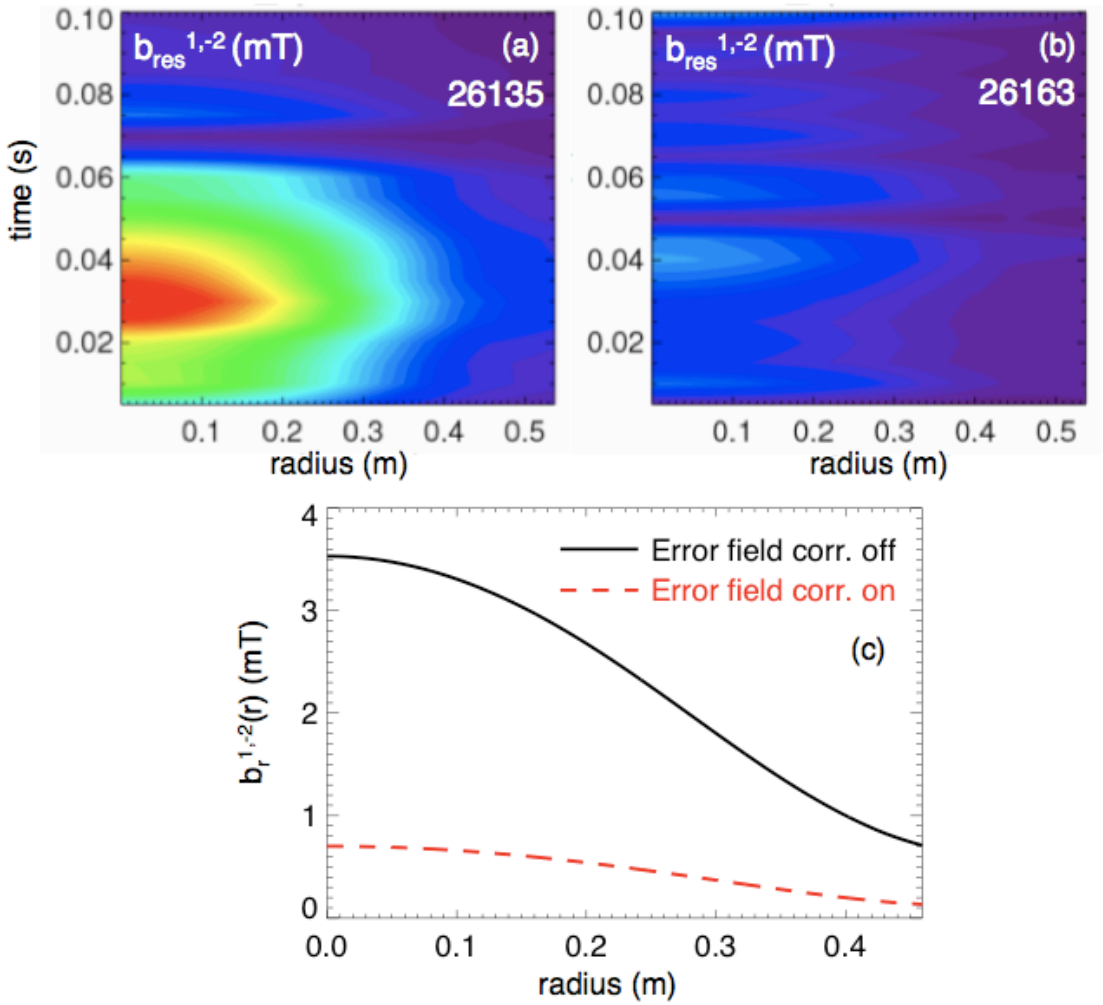

Figure 4.11: Contour plot of the perturbed radial magnetic field at the resonant radius of the $(1, -2)$ error field harmonic (a) without and (b) with error field correction. (c) Radial eigenfunction of the $(1, -2)$ error field harmonic with (black continuous line) and without (red dashed line) error field correction. The analyzed plasma experiments are the same as in the Figure 4.9.

strongly reduced. When pre-programmed coil currents and multi-mode feedback are applied to correct the error fields, the response of the plasma in the first $0.06s$ is much lower than the case without error field correction, as shown in Figure 4.11(b).

The plasma response effect is also illustrated in Figure 4.11(c), which reports the radial magnetic field eigenfunction of the $(1, -2)$ harmonic at $t = 0.03ms$, both with and without error field correction. Note that the plasma response is significantly reduced with error field correction (dashed red line), but it does not

completely vanish. Similar results are found also for the other error field harmonics.

Based on this Thesis work, it may be argued that an error field correction scheme acting directly on the plasma response, similar to what usually done for example in DIII-D and described in Chapter 7, should reduce to even lower values the radial magnetic field amplitude throughout the plasma. For these reasons, modifications of the RFX-mod feedback algorithm have been proposed for the 2011 experimental campaign, as will be discussed in Chapter 8. The main modification consists in using, as feedback variable, the plasma response, calculated subtracting from the radial magnetic field measurements the external field produced by the active coils, instead of the total edge radial magnetic field measured by the sensor loops.

CHAPTER 5

Optimization of the helical RFX-mod equilibrium

In this Chapter, experiments on RFX-mod helical equilibria, which have been controlled by applying helical boundary conditions at the edge with magnetic feedback will be presented. In particular, how the control of these equilibria has been optimized will be discussed. The optimization concerns the identification of the optimal feedback parameters in the mode controller, the amplitude and phase of the applied helical magnetic field at the plasma edge. The effect of these quantities on the mode dynamics has been studied by modifying the RFXlocking code. In particular, the possibility to apply helical boundary conditions has been added in this code. The mode dynamics of the $(1, -7)$ *mode with this new helical magnetic boundary has been investigated and a model-based approach, similar to the one described in Chapter 3, has been adopted here to find the gain set, which allows to produce the requested* $(1, -7)$ *edge radial magnetic field with the lowest possible coil current. The main findings of this model-based optimization will be discussed.*

5.1 3D shaping to control helical RFX-mod equilibria

As described in Chapter 1, in high-plasma current RFX-mod scenarios, a spontaneous transition to a $(1, -7)$ helical equilibrium and with an electron internal transport barrier is observed as the plasma current is raised above $1MA$ [40]. This new helical equilibrium is not stationary occasionally, but it is perturbed by spontaneous relaxation events, during which a broad spectrum of $m = 1$ secondary modes are excited [31]. Even though the duration of the helical equilibrium is observed to steadily increase with the plasma current, as shown in Figure 1.14(a) in Chapter 1, obtaining a truly stationary helical equilibrium would be desirable for reliable operation in this new regime.

In RFX-mod, during the 2010 experimental campaign, experiments have shown that such equilibria can be controlled by applying helical boundary conditions at the edge with magnetic feedback. This has been done by imposing a finite reference value for the radial magnetic field amplitude and phase of the $(1, -7)$ mode. In this way, the helical equilibrium could be sustained and controlled, avoiding most of the relaxation events mentioned above [44].

During this Thesis work, helical equilibria obtained by imposing helical boundary conditions through magnetic feedback have been optimized. The optimization concerns the identification of the best amplitude and phase of the external $(1, -7)$ magnetic field and of the feedback gains in the mode controller that allow to obtain almost stationary states with low coil current. In particular, the optimization procedure adopted is similar to the model-based approach described in Chapter 3, since the mode dynamics with this new helical boundary condition at the edge has been simulated by modifying the RFXlocking code adding the possibility to apply external magnetic field perturbations.

Several simulations have been performed by varying, one by one, the parameters above mentioned. The aim is to identify the gain set that allows to produce the requested $(1, -7)$ edge radial magnetic field with the lowest possible coil current. Moreover, the choice of the external magnetic field amplitude has be optimized in order to reduce as much as possible the plasma-wall interaction, which, as aspected, can increase in these experiments. The main outcomes of this work will be described in the following Sections together with the effects on the plasma performance in these helical equilibria.

5.2 An example of a helical equilibrium controlled by magnetic feedback

As mentioned in the previous Section, 3D external magnetic field perturbations applied through magnetic feedback system have been used in RFX-mod to control the self-organized helical equilibrium. An example of these experiments is shown in Figure 5.1 for a $1.5MA$ plasma current discharge. The helical boundary con-

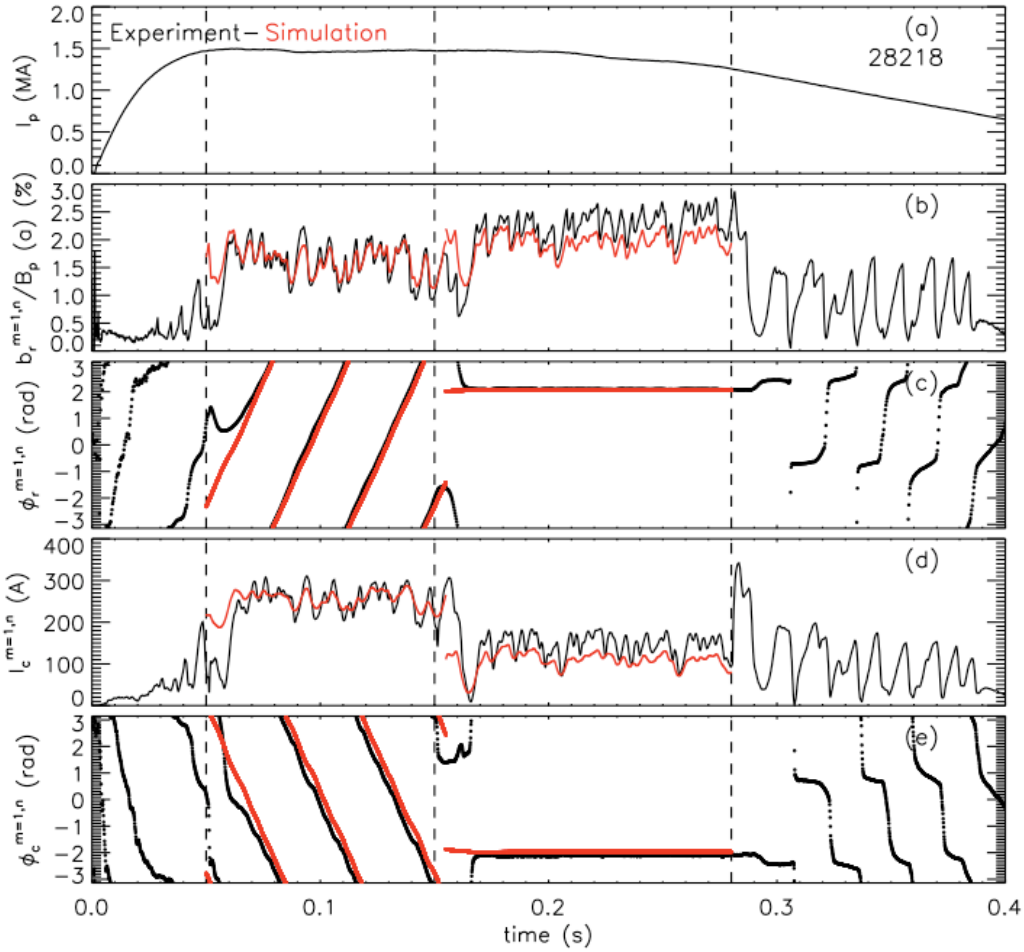

Figure 5.1: (a) Plasma current, (b) $b_r/B_p(a)$ edge amplitude and (c) phase of the $(1,-7)$ harmonic and (d) coil current amplitude and (e) phase of the same harmonic for the 28218 plasma experiment. The red trace corresponds to a simulation of the mode dynamics with magnetic feedback described in the text. A finite $(1,-7)$ b_r is externally applied with the active coils in the time interval $0.05-0.28s$, rotating at $33Hz$ in the interval $0.05-0.15s$ and static in the interval $0.15-0.28s$.

ditions are applied in the time interval $0.05-0.28s$, as indicated with vertical dashed lines. The $(1,-7)$ harmonic is rotated at a frequency of $33Hz$ in the time interval $0.05-0.15s$ and is maintained static in the time interval $0.15-0.28s$. The reference amplitude normalized to the poloidal magnetic field in this case amounts to $A_{ref}/B_p(a) = 0.95\%$, while the chosen rotation frequency $\omega_{ref} = d\phi_{ref}/dt$ is $\omega_{ref} = 33Hz$, where ϕ_{ref} is the phase reference.

The main result of this experiment is that the helical magnetic equilibrium becomes almost stationary as the helical boundary conditions are applied. Hence, the relaxation events that usually perturb this equilibrium are strongly reduced

in amplitude, but they reappear as soon as the helical boundary conditions are turned off starting from $t = 0.28s$. This is highlighted in Figures 5.1(b) and (c), where the normalized edge radial magnetic field amplitude and phase of the $(1, -7)$ mode are respectively shown as a function of time.

The reason of this significant change in the dynamics of the helical state is still under debate. Recently, a necessary condition for a helical Ohmic RFP equilibrium to exist has been derived analytically in the frame of resistive MHD using perturbation theory [103, 104]. This condition has been shown to be more easily satisfied if the radial magnetic field of the $(1, -7)$ harmonic does not vanish in a region near the edge, which may explain why imposing a helical boundary condition makes the helical equilibrium almost stationary in these experiments.

The experiment described above shows in particular that it is possible to maintain in time even a static helical equilibrium. This is not a trivial result, since being able to sustain a static helical equilibrium will be very important for possible future divertor operation, as recently proposed in [105]. Moreover, operating with a static helical equilibrium has the advantage that less $(1, -7)$ coil current is needed to produce a certain radial magnetic field at the plasma edge, as shown in 5.1(d), since the externally produced $b_r^{1,-7}$ is not shielded by the wall in this case. During the static phase, the $(1, -7)$ coil current amplitude is reduced by about 50% with respect to the rotating phase.

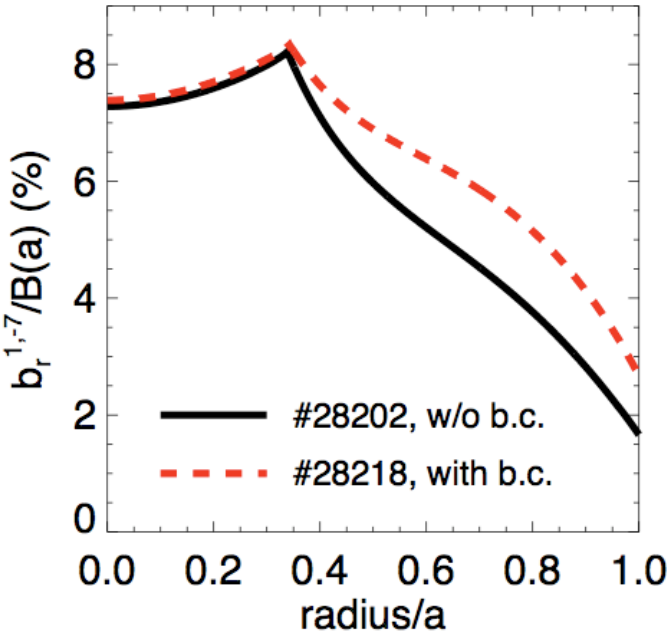

Figure 5.2: Radial magnetic field eigenfunctions of the $(1, -7)$ mode without (black continuous line; discharge 28202 at $t = 0.186s$) and with (red dashed line; discharge 28218 at $t = 0.186s$) finite helical boundary conditions applied.

Another advantage is that the magnetic field errors produced by the eddy-currents induced in the 3D wall structures when the mode rotates completely disappear in the static case. A description of such error fields and of the techniques developed to correct them in these experiments will be the subject of Chapter 6 [43].

The effect of imposing helical boundary conditions on the $(1, -7)$ mode radial profile of the radial magnetic field has been investigated by comparing a case without and one with helical boundary conditions applied. The main result of this analysis is shown in Figure 5.2. The radial magnetic field eigenfunction has been reconstructed by solving the Newcomb's equation, with external magnetic measurements in input [71]. The $(1, -7)$ radial field is about 8% of the total field in the core and decreases to $1-2\%$ at the edge. With the helical boundary conditions applied, the edge radial field increases at most to 3%, confirming that even in these cases the RFP configuration remains almost axisymmetric at the edge. The helical boundary conditions affect the radial eigenfunction up to $r/a \approx 0.4$, but the overall shape of the eigenfunction does not change significantly.

5.3 $(1, -7)$ mode dynamics with external 3D magnetic fields

As described in Chapters 2 and 3, the variable that the RFX-mod mode control algorithm normally tries to reduce is the edge radial magnetic field amplitude of each (m, n) harmonic and the feedback law is described by Equation (2.1). To model with the RFXlocking code the experiments investigated in this Chapter, the feedback variable has to be modified by setting a non-zero reference value for the $(1, -7)$ helicity, i.e. $e(t) = b_r(t) - b_r^*(t)$, where $b_r^*(t)$ is the external edge radial magnetic field set in the mode controller as reference. Note that the $b_r^*(t)$ can be written as $b_r^*(t) = A_{ref}(t)e^{i\phi_{ref}(t)}$, where, as mentioned before, $A_{ref}(t)$ and $\phi_{ref}(t)$ are the reference amplitude and phase, respectively. With this modification, the feedback law becomes:

$$I_c^{m,n}(t) = K_p^{m,n} e(t) + K_i^{m,n} \int_0^t dt' e(t') + K_d^{m,n} \frac{d}{dt} e(t). \tag{5.1}$$

The plasma experiment represented in Figure 5.1 has been simulated once implemented in the code the feedback law in Equation (5.1) and the results are plotted in red, showing a satisfactory agreement with all the experimental time traces. Given its good match with the experiment, the modified RFXlocking code has been used to investigate the $(1, -7)$ mode dynamics by varying the feedback gains, the amplitude and phase references. Such scans can be performed in the experiment, but they would require a large number of discharges. To save experimental time, it is preferable to simulate the mode dynamics with the RFXlocking code and to identify offline the best control parameters.

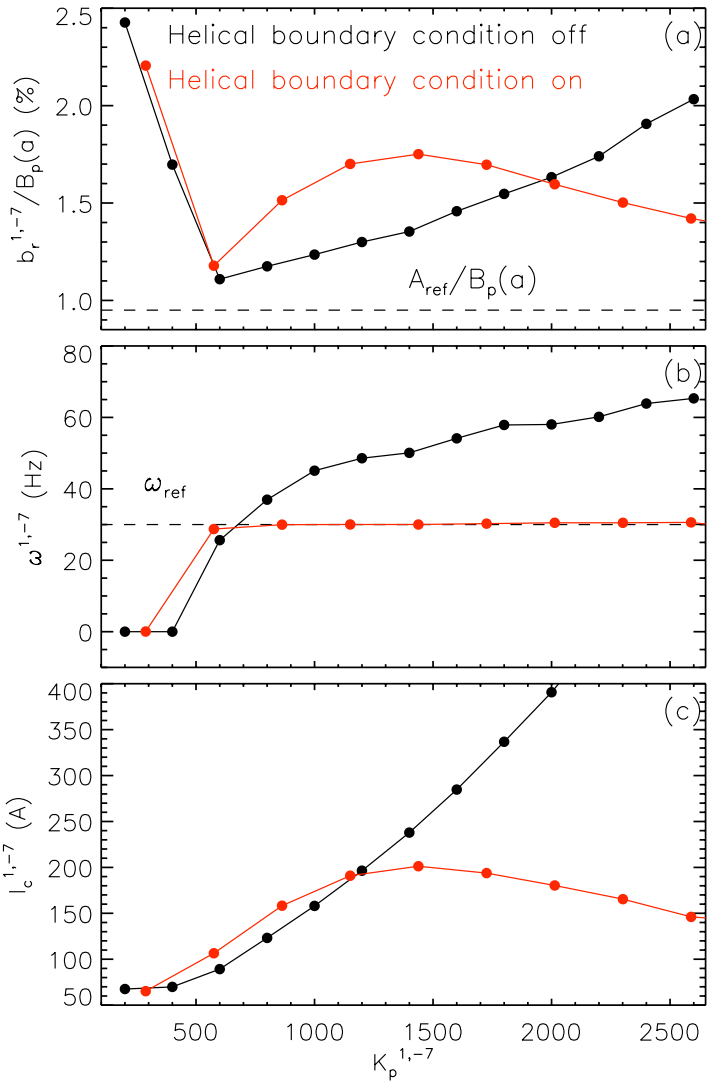

Figure 5.3: (a) Simulated $(1, -7)$ normalized edge radial magnetic field amplitude, (b) mode rotation frequency, and (c) coil current amplitude as a function of the proportional gain. The black and red curves correspond to the trends of the above quantities without and with helical boundary condition, respectively. For the red curve an amplitude of $A_{ref}/B_p(a) = 0.95\%$ and a frequency of $\omega_{ref} = d\phi_{ref}/dt = 33Hz$ have been used.

At first, the $(1, -7)$ mode dynamics has been simulated by varying the proportional gain and the results are compared with a case without helical boundary conditions. In the case examined in Figure 5.1, the applied helical boundary condition has an amplitude of $A_{ref}/B_p(a) = 0.95\%$ and rotates at $33Hz$, as indicated by the horizontal grey dashed lines. The $(1, -7)$ normalized edge radial magnetic

field amplitude, mode rotation frequency and coil current amplitude plotted in the Figure 5.3 have been calculated as averages in the time interval $\Delta t = [50, 120]ms$.

When the applied proportional gain is in the range $K_p \in [100, 600]$, the trends of the $(1, -7)$ radial magnetic field amplitude and coil current amplitude with (in red) and without (in black) helical boundary conditions are very similar. For higher proportional gains, in the case with helical boundary conditions, both the radial field and the coil current amplitude increase and reach a local maximum near $K_p = 1400$, then decrease. Instead, without helical boundary condition these variables slowly increase as the value of K_p is raised. Without helical boundary condition, above a K_p threshold, which is around 400, the $(1, -7)$ mode starts to rotate and the rotation frequency increases with the increase of the proportional gain. With helical boundary condition instead the mode starts to rotate even with low K_p values, around 200, and for K_p higher than 600 the $(1, -7)$ mode rotation frequency is fixed as imposed by the reference frequency.

5.3.1. Amplitude and frequency scans

The impact on the $(1, -7)$ mode dynamics of a finite edge radial magnetic field at the plasma edge imposed through magnetic feedback has been analyzed by applying $(1, -7)$ magnetic field perturbations that rotate at a fixed frequency and at various $A_{ref}/B_p(a)$ values. Since the typical $(1, -7)$ mode rotation frequency in the experiment is about $30Hz$, as shown by the statistical analysis reported in Figure 2.6, this value has been set as the chosen frequency. He gas has been used in these experiments, the plasma current was of the order of $1.2MA$, the reversal parameter in the range $F \in [-0.4, -0.34]$, and the electron density normalized to the Greenwald density $n/n_G \in [0.05, 0.09]$.

For these ensemble of discharges, the $(1, -7)$ normalized edge radial magnetic field amplitude, mode rotation frequency, and coil current amplitude have been calculated and the results are shown in Figure 5.4, on the left, as a function of $A_{ref}/B_p(a)$. The points represent flat-top averaged estimates, while the error bars represent the temporal variation of the above quantities associated with the small relaxation events and correspond to the 25^{th} and the 75^{th} percentiles of the data.

As aspected, the $(1, -7)$ edge radial magnetic field amplitude increases by increasing the reference amplitude, and consequently the request of $(1, -7)$ coil current, as shown in Figures 5.4(a) and (c) on the left. Figure 5.4(b) suggests that by increasing the reference amplitude it is easier to maintain into rotation a mode at a desired frequency.

These evidences are confirmed by the predictions of the RFXlocking code, represented with a red curve in Figure 5.4 on the left. This curve has been obtained by simulating the $(1, -7)$ mode dynamics varying $A_{ref}/B_p(a)$ and at fixed frequency $\omega_{ref} = 30Hz$ and proportional gain $K_p = 800$, which is the gain set in the mode controller in these experiments. The good agreement between the experimental

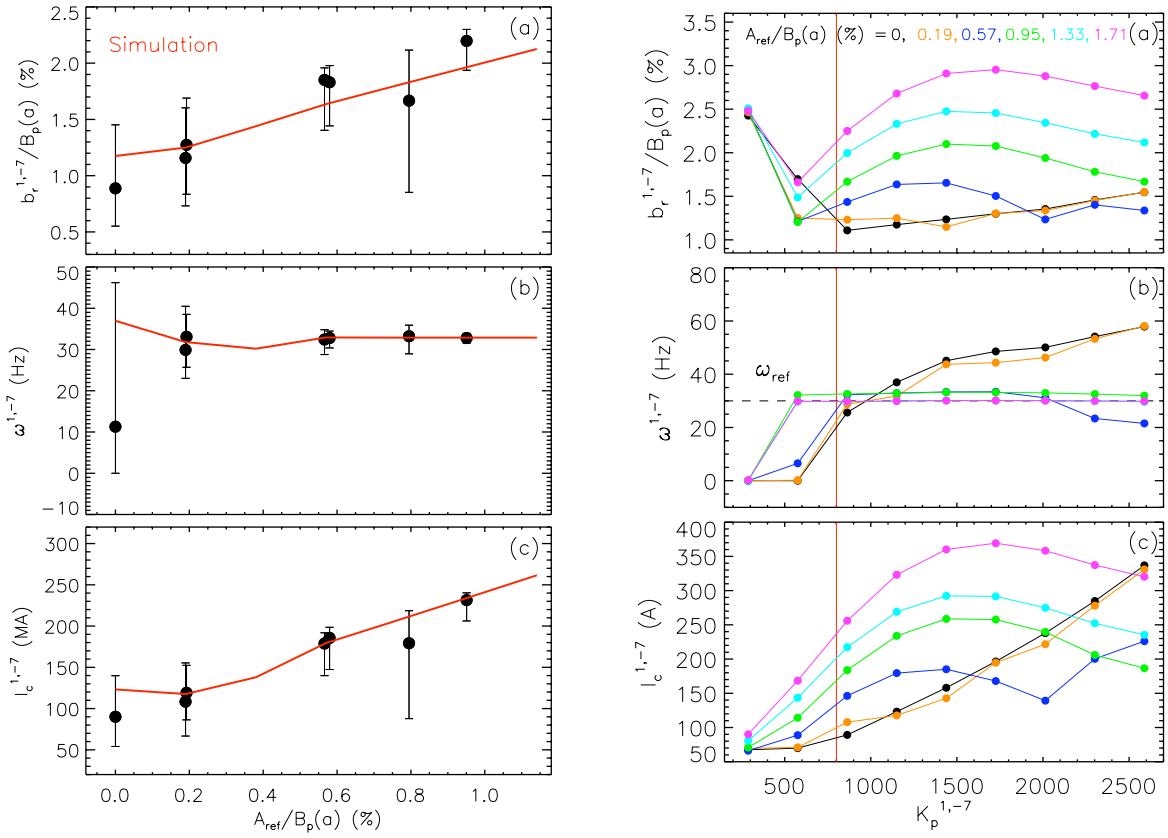

Figure 5.4: On the left: (a) $(1, -7)$ normalized edge radial magnetic field amplitude, (b) mode rotation frequency, and (c) coil current amplitude as a function of the reference amplitude. The points represent flatt-top averaged variables, while the error bars indicate the 25^{th} and the 75^{th} percentiles of the data. The red line corresponds to the trend obtained by the simulations plotted on the right figure, at a fixed $K_p = 800$. On the right: simulated (a) $(1, -7)$ normalized edge radial magnetic field amplitude, (b) mode rotation frequency, and (c) coil current amplitude as a function of the proportional gain. The grey dotted line in panel (b) indicates the chosen rotation frequency. The vertical red line indicates the proportional gain used in the experiments described in the text.

results and the simulated trend reveals that the modified RFXlocking is a reliable tool to predict the feedback dynamics when external 3D magnetic fields are imposed through feedback to sustain the helical equilibrium.

The right plots in Figure 5.4 represent the $(1, -7)$ normalized edge radial magnetic field amplitude, mode rotation frequency, and coil current amplitude as a function of the proportional gain, for various values of $A_{ref}/B_p(a)$. The model suggests that for low values of $A_{ref}/B_p(a)$, below about 0.2%, the $(1, -7)$ mode

does not rotate at the desired rotation frequency and its mode dynamics, shown in orange, is more similar to the case without helical boundary conditions applied, plotted in black in the same figure.

When the reference amplitude is increased above 0.95% the $(1, -7)$ mode is maintained into rotation at the chosen frequency. Simulations with reference amplitudes higher than 1.7%, not shown in the figure, predict that the request of coil current is too high, above the maximum coil current of $320A$, even with low proportional gains. These cases are forbidden because of coil current saturations in the power supllies. Based on these analyses, $A_{ref}/B_p(a) = 0.95\%$ has been selected as the optimal value for the experiment, since it is the lowest reference amplitude that can maintain the mode into rotation at the desired frequency.

The effect on the mode dynamics of applying helical boundary conditions rotating with different frequencies has been investigated by simulating the mode dynamics by varying ω_{ref} in the range $\omega_{ref} = [0, 60]Hz$, maintaining fixed the reference amplitude equal to 0.95%, as suggested by the analysis of the reference amplitude scan described above. The main outcomes of the frequency scan, in terms of the $(1, -7)$ normalized edge radial magnetic field amplitude, mode rotation frequency, and coil current amplitude, are shown in Figure 5.5 as a function of the proportional gain.

Note that decreasing the value of the chosen frequency, lower $(1, -7)$ coil current is needed since the externally produced $(1, -7)$ edge radial field can penetrate the wall being less shielded. By comparing the cases with $\omega_{ref} = 30Hz$ and $\omega_{ref} = 0Hz$, the RFXlocking code suggests a decrease of the $(1, -7)$ coil current amplitude of about 50%, value that is compatible with the experimental results shown in Figure 5.1(e), where a helical boundary condition rotating near $30Hz$ has been applied in the first time window $0.05 - 0.150s$, and a static helical boundary condition in the second one, $0.15 - 0.28s$. These results, especially in the case of slowly rotating or static helical boundary conditions, are important for possible future RFP experiments that may operate with a helical divertor to control the plasma-wall interaction as proposed recently in [105].

5.3.2. Model-based optimization of the gains on the $(1, -7)$ harmonic and comparison with the experiment

The control of the RFX-mod helical equilibrium has been done also identifying a set of proportional and derivative gains that allows to produce the requested $(1, -7)$ b_r at the edge with the least possible coil current. To this aim, several simulations have been performed by varying the proportional and derivative gains, using an approach similar to the one described in Chapter 3 for the optimization of tearing mode control. Based on the analysis reported in the previous Section and on the statistics of the mode rotation frequency in Figure 2.6, the applied helical boundary condition considered here has an reference amplitude $A_{ref}/B_p(a) = 0.95\%$ and a

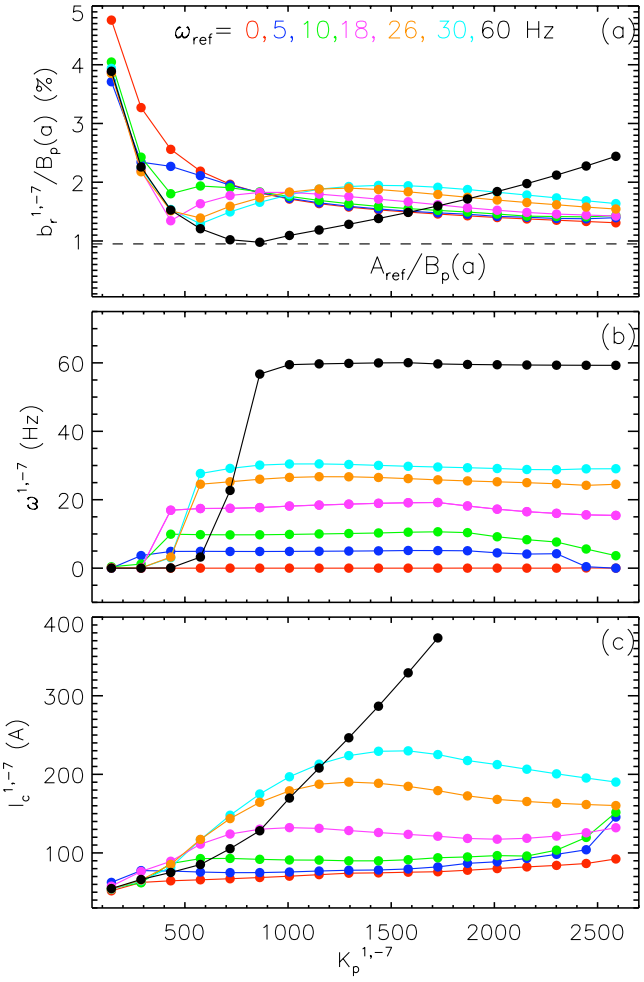

Figure 5.5: (a) $(1, -7)$ normalized edge radial magnetic field amplitude, (b) mode rotation frequency, and (c) coil current amplitude as a function of the proportional gain for different values of ω_{ref}. The amplitude of the finite edge radial magnetic field is fixed at $A_{ref}/B_p(a) = 0.95\%$, as indicated in panel (a) by the dashed grey line.

reference frequency $\omega_{ref} = 30Hz$.

As discussed in Section 5.3 for a purely proportional gain, the mode dynamics with helical boundary conditions applied becomes not trivial. Adding a derivative gain does not change significantly the mode dynamics, but lower normalized $(1, -7)$ edge radial magnetic field and coil current values can be obtained, as shown in Figure 5.6. The curve with $K_d = 0$ is shown in black, $K_d = 1$ in red, $K_d = 1.5$ in blue, and $K_d = 2$ in green. A partial gain scan has been also done in the experiment. The results from four discharges similar to the one shown in Figure 5.1, but with varying proportional and derivative gains, are plotted in Figure 5.6:

the black circles represent cases with a purely proportional gain, the red diamond a case with both proportional and derivative gains.

These experimental results confirm the trends predicted by the model: by adding a derivative gain a reduction of the edge radial field, and consequently of the requested coil current, is obtained. Based on this analysis, a purely proportional gain near the predicted radial field minimum $K_p = 600$ has been finally chosen. Near the minimum in fact a derivative gain does not make a great difference in terms of coil current reduction, but it may to some extent amplify the noise in the sensor signals.

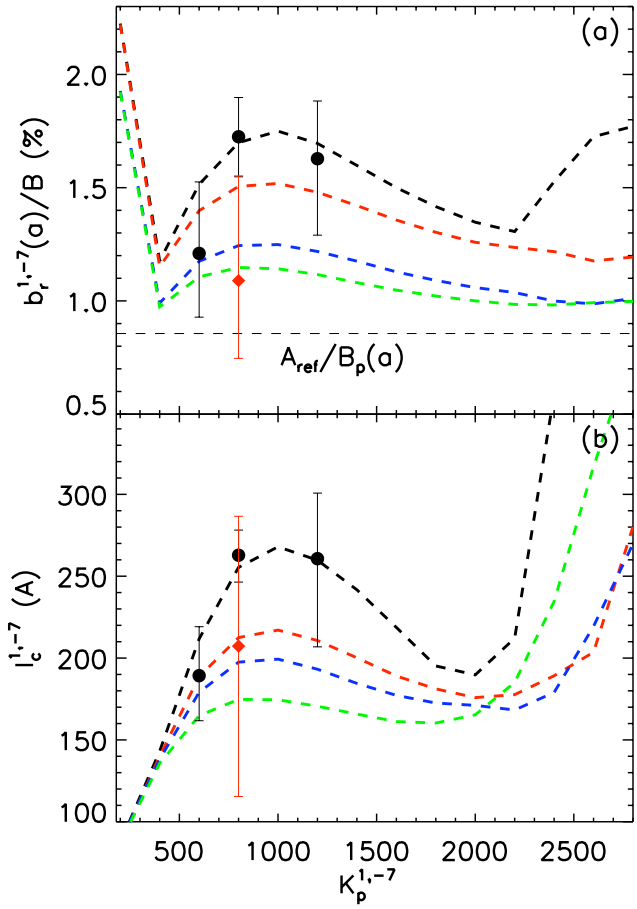

Figure 5.6: (a) $b_r/B_p(a)$ and (b) $(1,-7)$ coil current amplitude as a function of the proportional gain and at different values of the derivative gain: $K_d = 0$ (black), 1 (red), 1.5 (blue), and 2(green). The dashed lines correspond to simulations made with the model described in the text and the symbols to flat-top averages of four similar RFX-mod discharges with varying proportional and derivative gains. The same color coding applies. The grey dashed line in panel (a) represents the reference amplitude set in the controller.

5.4 Effect of helical boundary conditions on plasma performance

The optimal feedback parameters identified as described in the previous Section have been used during an experimental campaign, which aimed at studying the effect of external 3D magnetic fields, used to control the helical equilibrium, on the overall plasma performance. This has been evaluated by analyzing a series of similar discharges with increasing values of $A_{ref}/B_p(a)$.

The main results are summarized in Figure 5.7. Note that in this case the estimates are plotted as a function of the normalized edge radial magnetic field amplitude of the $(1,-7)$ mode instead of $A_{ref}/B_p(a)$. The analyses have been carried out for two groups of discharges with different plasma current and working gas: a group of He discharges with $I_p \approx 1.2MA$, indicated with open circles, and a second group of H discharges with $I_p \approx 1.5MA$, indicated with full circles.

Figure 5.7(a) shows that the helical-state persistence, defined as the ratio between the total helical state duration and the flat-top duration, increases continuously as the the $(1,-7)$ radial field is increased, reaching values of about 100%, which confirms more statistically that an almost stationary helical equilibrium can be robustly obtained with external control.

Since the energy and particle confinement can be affected by magnetic field stochasticity induced by the secondary modes and by the $m = 0, n = 1, 2, 3, ...$ modes resonant at the reversal surface, the flat-top averaged amplitudes of $m = 1$ secondary modes and of $m = 0$ modes, defined as

$$b_t^{sec}/B_p(a) = \sqrt{\sum_{m=1,n=-16}^{-8} (b_t^{1,n})^2}/B_p(a), \tag{5.2}$$

$$b_t^{m=0}/B_p(a) = \sqrt{\sum_{m=0,n=1}^{3} (b_t^{0,n})^2}/B_p(a), \tag{5.3}$$

have been calculated. The $m = 1$ secondary mode amplitude slightly decreases or remains almost constant, as reported in Figure 5.7(b), while the $m = 0$ mode amplitude decreases by about 50% as the reference amplitude is doubled, as shown in Figure 5.7(c). These results are rather promising, even though they are not fully understood at the moment. It may be speculated that the stability of these modes is affected either by the modified helical magnetic equilibrium or by the different flow profile, as indicated by first flow measurements recently published in [44, 106].

As an effect of the secondary mode reduction, when the helical boundary conditions are applied, the overall flux surface robustness would be expected to improve. Nevertheless, a slight reduction of the energy confinement time of about 15% is observed, as shown in Figure 5.7(d), while the ratio between the kinetic and magnetic pressure, commonly expressed by the parameter $\beta_\theta = 2\mu_0 p/B_\theta^2(a)$, stays almost

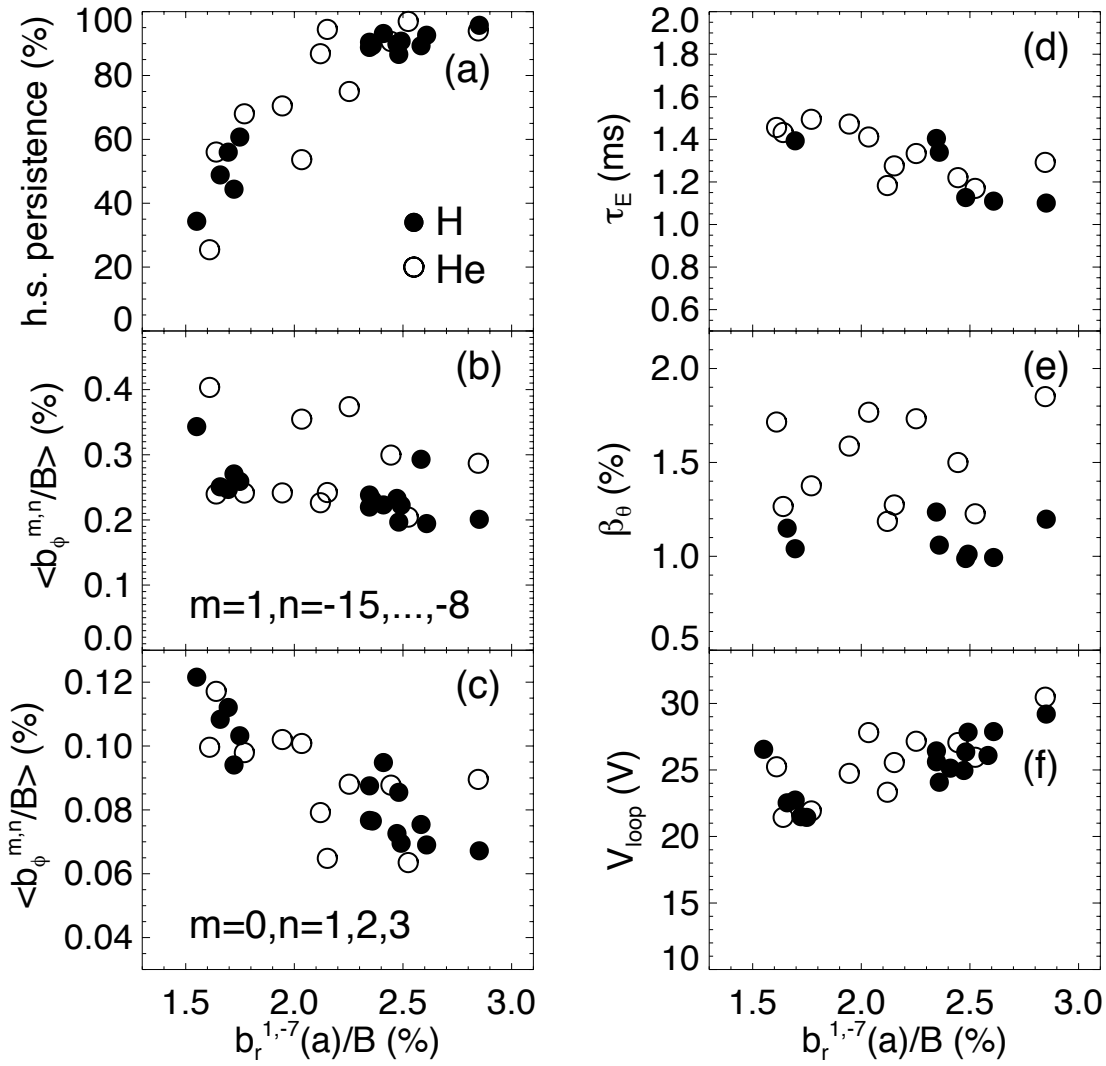

Figure 5.7: (a) Helical state persistence, (b) normalized toroidal magnetic field amplitude of the secondary modes, (c) normalized toroidal magnetic field amplitude of the $m = 0, n = 1, 2, 3$ modes, (d) energy confinement time, (e) poloidal β, and (f) loop voltage for discharges with different values of the $(1, -7)$ normalized edge radial magnetic field amplitude. The values are flat-top averages and full and open circles refer to H and He discharges, respectively.

constant as reported in Figure 5.7(e). In fact the loop voltage necessary to sustain the same plasma current, which is shown in Figure 5.7(f), increases by about 50%. This is probably due to an increased plasma-wall interaction associated with the increase of the edge radial magnetic field amplitude. This limitation could be solved in the future by controlling the wall recycling with a divertor, as proposed recently in [105].

Role of the integral gain to produce static helical boundary conditions

The results described in the previous section have shown that it is possible to sustain a $(1, -7)$ helical equilibrium up to 100% of the flat-top phase, when helical boundary conditions are applied through magnetic feedback, and a reduction of $m = 1$ secondary mode and the $m = 0$ mode amplitudes has been obtained. However, in these experiments the plasma performance does not improve due to the increase of the plasma-wall interaction. The RFXlocking code suggests that it is possible to reduce the $(1, -7)$ radial magnetic field at the plasma edge and thus the plasma-wall interaction if static helical boundary conditions are applied through magnetic feedback and a PI controller is used, as will be discussed in the following.

The $(1, -7)$ mode dynamics has been simulated with the RFXlocking code when a static helical boundary condition with a reference amplitude equal to $A_{rif}/B_p(a) = 0.45\%$ is applied. Since the integral gain is effective in compensating slowly growing or static perturbations, it may be useful in these experiments. For this reason, the role of the integral gain on the $(1, -7)$ mode dynamics has been investigated. Various K_i scans have been performed and the best results in terms of lowest coil current amplitude has been obtained with a K_i equal to 2500.

The main results in terms of the $(1, -7)$ normalized edge radial magnetic field amplitude, mode rotation frequency, and coil current amplitude as a function of the proportional gain are shown in Figure 5.8. The case without helical boundary conditions applied is plotted in black, while the one with is shown in red for a purely proportional gain, in green for a proportional gain and a fixed integral gain, $K_i = 2500$.

As expected, when helical boundary conditions are applied through magnetic feedback, the increase of the plasma-wall interaction is due to the fact that the $(1, -7)$ edge radial magnetic field amplitude increases with respect to the case without helical boundary conditions, as shown in Figure 5.8(a) comparing the black and the red curves. Nonetheless, when static helical boundary conditions and both proportional and the integral gains are applied, the $(1, -7)$ normalized radial magnetic field amplitude is significantly reduced with respect to the case of a purely proportional gain. The values of $b_r/B_p(a)$ so obtained are similar to the case without helical boundary condition, as shown by comparing the green and the black curves in Figure 5.8(a).

When PI gains are applied in the mode controller, the $(1, -7)$ mode is maintained static for proportional gains lower than a threshold value, of about $K_p = 1000$, above which the $(1, -7)$ mode starts rotating.

In summary, by applying static helical boundary conditions and PI gains in the $(1, -7)$ mode controller the RFXlocking code suggests that it is possible to obtain a $(1, -7)$ radial magnetic field amplitude at the plasma edge comparable

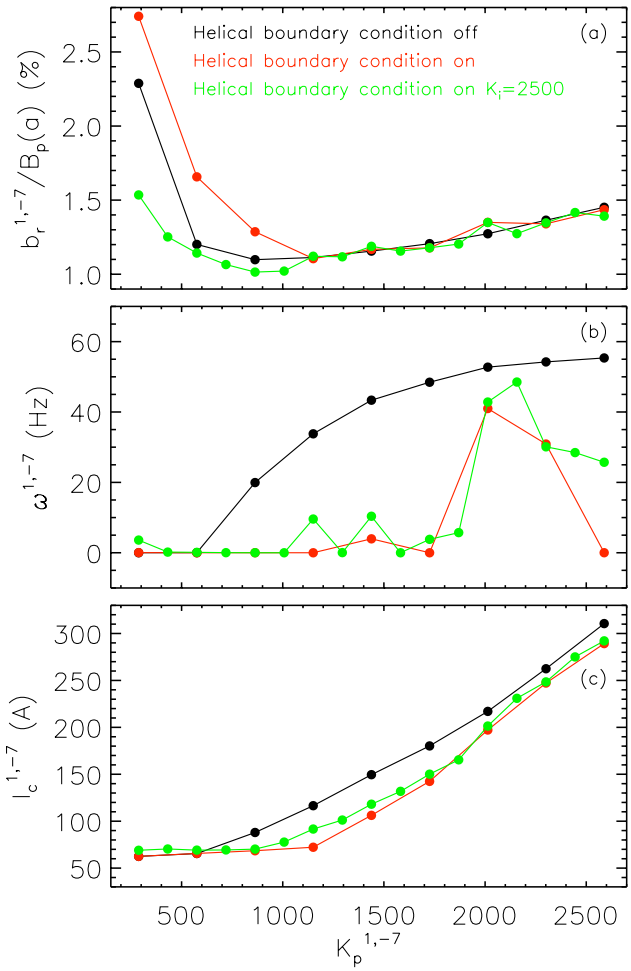

Figure 5.8: (a) $(1,-7)$ normalized edge radial magnetic field amplitude, (b) mode rotation frequency, and (c) coil current amplitude as a function of the proportional gain. The traces correspond to simulations without (black) and with (red and green) static helical boundary conditions. For the latter simulations, a normalized reference amplitude of $A_{ref}/B_p(a) = 0.45\%$ has been applied, and they differ for the applied gain: the red curve corresponds to the case of a purely proportional gain, while the green one to proportional gain and at fixed integral gain ($K_i = 2500$).

with the case without helical boundary conditions. Moreover, a lower coil current is requested for the $(1,-7)$ control in this case, as shown in Figure 5.8(c). The application of both proportional and integral gains has not yet been tested in the experiment, but it has been proposed for the 2011 RFX-mod experimental campaign to test the feasibility of this technique.

CHAPTER 6

Error field correction in helical RFX-mod equilibria

In this Chapter, the dynamic response of the RFX-mod wall to the external magnetic field used to control the $(1, -7)$ *equilibrium is investigated. External 3D magnetic fields at the plasma edge have been imposed through magnetic feedback with encouraging results to sustain the helical equilibria, as described in Chapter 5. Dry shots have revealed that, when doing magnetic feedback in these experiments, spurious magnetic fields are produced, due to the presence of the wall 3D structures, and in particular of the toroidal gap. A dynamic decoupling algorithm similar to the one used to correct the error fields in the current ramp-up phase of the plasma discharge, as described in Chapter 4, has been applied. It allows for the production of a pure radial magnetic field harmonic inside the wall, reducing the harmonic distortion due to the 3D wall structures. Moreover, other magnetic field errors have been detected and have been associated with the presence of the poloidal gaps in the wall structure.*

6.1 Error fields affect the control of helical equilibria

As described in the previous Chapter, helical equilibria with $(1, -7)$ helicity can be sustained by imposing helical boundary conditions, both static and rotating, through magnetic feedback. However, the presence of 3D wall structures tends to perturb the helical symmetry, with the deleterious effect of exciting secondary instabilities, that degrade the good confinement typical of these regimes. In this Chapter, the identification of the error fields associated with the 3D wall structure and their impact on the plasma performance will be presented, together with the control strategies developed to correct them [43].

To isolate the effect of the 3D wall structures on the penetration of the $(1, -7)$ radial magnetic field through the wall, vacuum experiments with $(1, -7)$ coil current perturbations rotating at different frequencies have been performed. One of these tests is shown in Figure 6.1 and corresponds to a vacuum discharge with a $(1, -7)$ coil current perturbation rotating at $20Hz$. The $(1, -7)$ coil current distribution in the 192 active coils, similar to the one used to sustain and control the helical equilibria, is shown in Figure 6.1(b) at a fixed time instant as a function of the poloidal and toroidal angles.

The radial magnetic field produced in vacuum by this current pattern and measured by the 48×4 radial field sensors is shown in Figure 6.1(c). The radial magnetic field pattern is not purely $(1, -7)$, as would be desired, but it is locally perturbed near the toroidal gap at $\theta = 180°$. This perturbation is produced by the particular eddy-current pattern induced near the toroidal gap by the temporal variation of the external $(1, -7)$ magnetic field, and its shape changes as a function of frequency. The net effect is that B_r penetrates faster at this gap.

The main Fourier harmonics that sum up to form this poloidally-localized deformation have been identified and correspond to $m = 0, 1, 2$ and $n = 7$ toroidal mode number. Dynamic decoupling techniques have been applied to compensate these error field harmonics. A description of the technique and of its application in the experiment will be presented in the following.

6.2 Error field correction strategy and its application

As described in the previous Section, when time-varying external magnetic fields are applied, the presence of the toroidal gap in the RFX-mod wall structure introduces error field harmonics. This occurs also when magnetic feedback is used to control the RFX-mod helical equilibrium. In this case, an approach similar to the one used for the error field correction in the current ramp-up phase and presented in Chapter 4 has been adopted here.

When only the $n = 7$ harmonic is considered the dynamic response of the wall can be described, in a way similar to the one described in Section 4.3, by a matrix of complex transfer functions between the $n = 7$ poloidal harmonics of

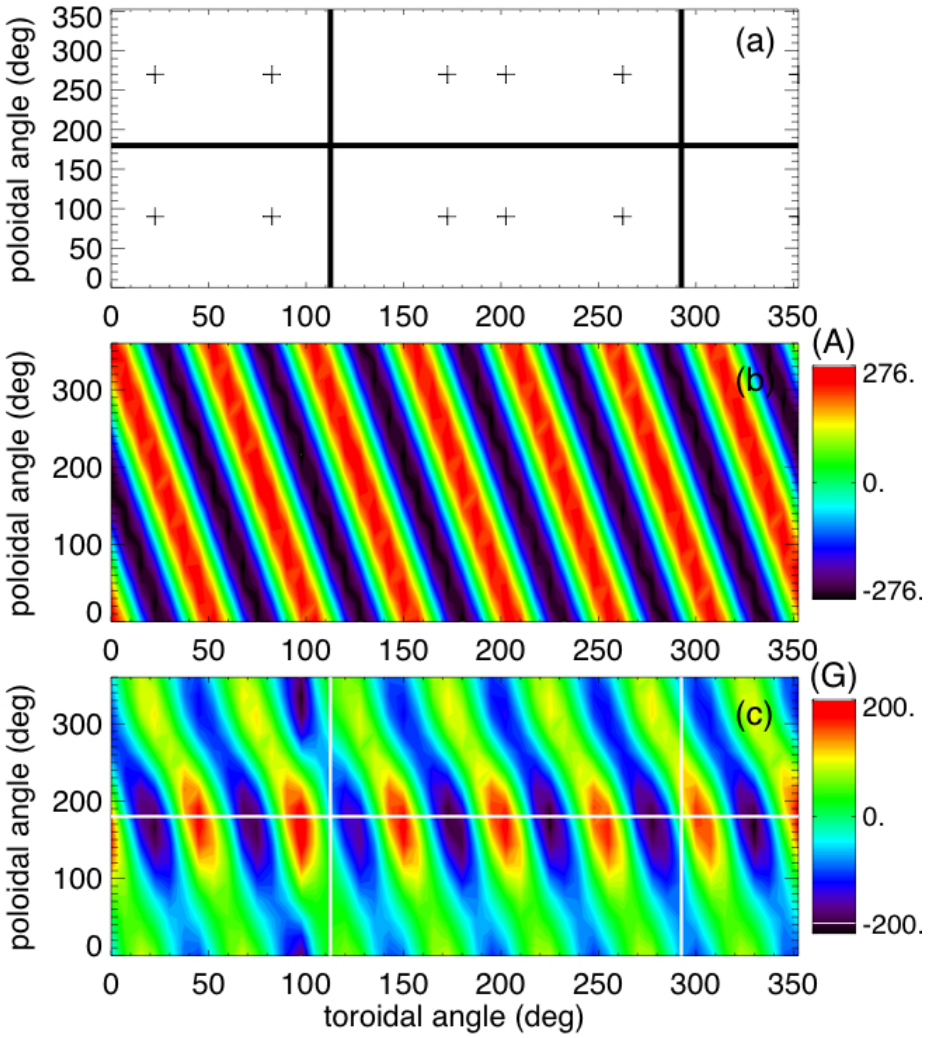

Figure 6.1: (a) Positions of the two poloidal gaps (vertical continuous lines), of the toroidal gap (horizontal continuous line), and of some larger portholes (crosses) in RFX-mod. (b) Feedback coil currents and (c) radial magnetic field as a function of the poloidal and toroidal angles as measured at fixed time in a vacuum experiment with a $(1, -7)$ perturbation on the coil currents rotating at $20Hz$. This vacuum field experiment corresponds to the 27085 discharge.

the coil currents and the same B_r harmonics, as a function of frequency. These transfer functions have been identified in vacuum discharges by feeding the active coils with $I_c^{1,-7}$ harmonic at different frequencies and measuring the induced $n = 7$ radial magnetic field. The same procedure has been carried out for the other m coil current components, i.e. $I_c^{0,7}, I_c^{1,7}, I_c^{2,7}$.

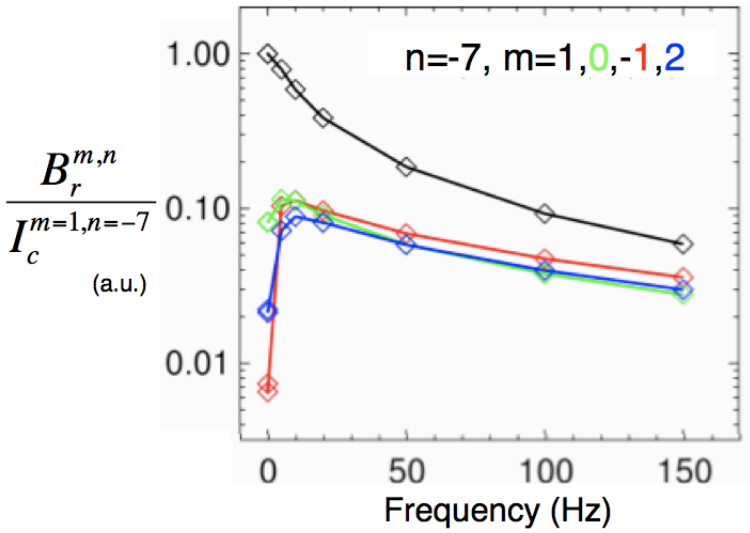

Figure 6.2: Transfer functions between the $(1,-7)$ harmonic of coil current and the same B_r harmonic (in black), and between the $(1,-7)$ harmonic of coil current and the error field harmonics induced by the wall toroidal gap.

An example of transfer function between the $n = -7$ poloidal harmonic of the coil current and the same n B_r harmonic is shown in black in Figure 6.2. The square symbols represent the measured transfer functions obtained by Fourier analyzing the coil current and the radial magnetic field measurements of the $(1,-7)$ harmonic, while the solid curve is the fit of the experimental data. The other e.m. coupling coefficients, plotted in Figure 6.2, correspond to the transfer functions between the $(1,-7)$ harmonic of coil current and the spurious error field harmonics induced by the wall toroidal gap. As aspected, the amplitude of the coupling coefficients is higher for the black trace that corresponds to the $b_r^{1,-7}$-$I_c^{1,-7}$ transfer function.

As mentioned above, a purely $(1,-7)$ rotating coil current represented in the following by the vector $[I_c^{1,-7},0,0,0]^T$ produces inside the wall a series of harmonics with $|n| = 7$ and different poloidal mode numbers, i.e. $[b_r^{1,-7},b_r^{0,7},b_r^{1,7},b_r^{2,7}]^T$, due to the presence of the toroidal gap in the RFX-mod wall structure. The dynamic response of the wall in this case can be described by the following matrix equation:

$$\begin{bmatrix} M_{1,-7}^{1,-7}(j\omega) & M_{0,7}^{1,-7}(j\omega) & M_{1,7}^{1,-7}(j\omega) & M_{2,7}^{1,-7}(j\omega) \\ M_{1,-7}^{0,7}(j\omega) & M_{0,7}^{0,7}(j\omega) & M_{1,7}^{0,7}(j\omega) & M_{2,7}^{0,7}(j\omega) \\ M_{1,-7}^{1,7}(j\omega) & M_{0,7}^{1,7}(j\omega) & M_{1,7}^{1,7}(j\omega) & M_{2,7}^{1,7}(j\omega) \\ M_{1,-7}^{2,7}(j\omega) & M_{0,7}^{2,7}v & M_{1,7}^{2,7}(j\omega) & M_{2,7}^{2,-7}(j\omega) \end{bmatrix} \cdot \begin{bmatrix} I_c^{1,-7} \\ 0 \\ 0 \\ 0 \end{bmatrix} = \begin{bmatrix} b_r^{1,-7} \\ b_r^{0,7} \\ b_r^{1,7} \\ b_r^{2,7} \end{bmatrix}, \tag{6.1}$$

where $\mathbf{M}(j\omega)$ is the matrix that represents the wall frequency response to the applied perturbation. As proposed in [98], the couplings introduced by the toroidal gap can be compensated by inverting the matrix $\mathbf{M}(j\omega)$ using a singular value

decomposition method. In this case the Equation (6.1) becomes:

$$\begin{bmatrix} I_c^{1,-7} \\ I_c^{0,7} \\ I_c^{1,7} \\ I_c^{2,7} \end{bmatrix} = \overleftrightarrow{\mathbf{M}}^{-1} \cdot \begin{bmatrix} b_r^{1,-7} \\ 0 \\ 0 \\ 0 \end{bmatrix}, \tag{6.2}$$

where $\overleftrightarrow{\mathbf{M}}^{-1}(j\omega)$ is the pseudo-inverse of the $\mathbf{M}(j\omega)$ matrix. This method, named modal dynamic decoupler, allows for the computation of the current spatial pattern needed to produce a pure $(1,-7)$ B_r inside the wall. This approach is quite similar to the one described in Chapter 4. For error field correction in the current ramp-up phase of the plasma discharge, once identified the time-behavior of the error fields, this has been used as input to the dynamic decoupler to calculate the current pattern in the 192 active coils necessary to correct the error fields. In the case examined here, the modal dynamic decoupler calculates the four coil current harmonics needed to produce a pure $(1,-7)$ radial magnetic field pattern at the plasma edge.

6.2.1. Vacuum field test of the modal dynamic decoupler

Before implementing such a scheme in real-time, tests using pre-programmed currents calculated offline with the modal dynamic decoupler were done in vacuum discharges. The decoupler currents were computed for the case reported in Figure 6.1 at a fixed frequency of $20Hz$.

A $(1,-7)$ coil current with constant amplitude and rotating at $20Hz$ was programmed for the whole discharge, as shown in black in Figure 6.3(a). Starting from $0.2s$ the decoupler currents are turned on. The pre-programmed currents computed with the dynamic decoupler to suppress the error field harmonics are plotted in Figure 6.3(a). As shown in Figure 6.3(b) after a time interval of about $0.02s$, necessary for the penetration of the radial magnetic field inside the wall, the mode decoupler reduces the error field harmonics to very low values, while the $(1,-7)$ harmonic is not affected.

6.2.2. Other error field sources

By analyzing the vacuum field experiment described in Figure 6.1, other error fields with smaller amplitude can be detected. These are associated with the two poloidal gaps and to the large portholes in the RFX-mod wall. In Figure 6.4 the radial magnetic field perturbation associated with harmonics with $|n| \neq 7$ is shown as a function of toroidal angle and time for two poloidal angles, $\theta = 180°$ and $270°$, respectively at the toroidal gap in Figure 6.4(a) and in correspondence of the portholes in Figure 6.4(c).

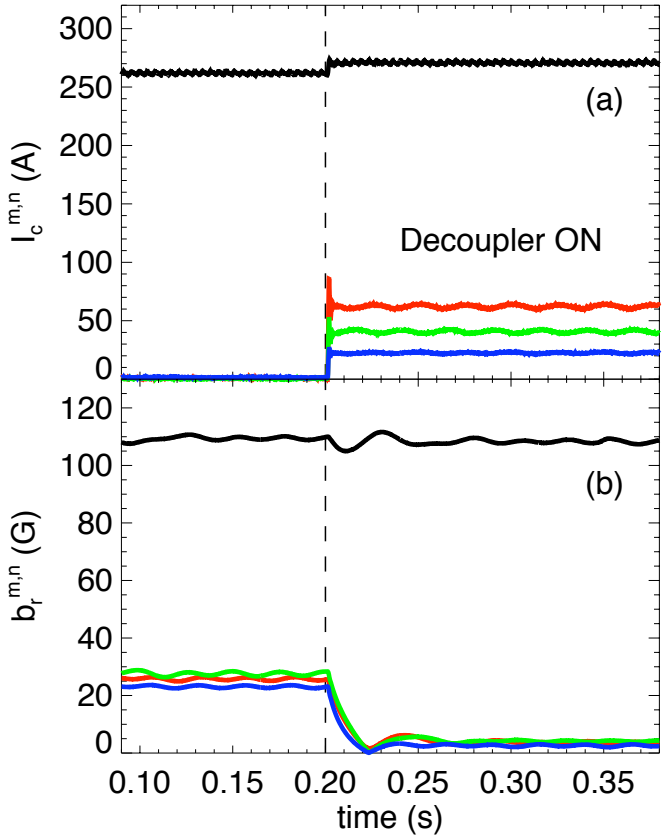

Figure 6.3: (a) Coil current and (b) radial magnetic field amplitudes of the $(1,-7)$ (black), $(0,-7)$ (red), $(1,-7)$ (green), and $(2,7)$ (blue) harmonics as a function of time in a vacuum discharge with a $(1,-7)$ coil current perturbation rotating at $20Hz$ up to $0.2s$. The dynamic decoupler is turned on from $0.2s$. The experiment analyzed is the same as in Figure 6.1.

In this case the dynamic decoupler described in the Chapter 4, which inverts the transfer function matrix among all the 192 active coils and the 192 radial field sensors, has been used. The current pattern on the 192 active coils has been computed by the dynamic decoupler and has been applied in a pre-programmed way starting from $t = 0.2s$.

To estimate the effect of the dynamic decoupler, a time averaged b_r has been calculated in the interval without the decoupler, $t = 0.1 - 0.2s$, and with the decoupler $t = 0.25 - 0.35s$. The results of the analysis are shown in Figures 6.4(b) and (d), respectively in black and in red. If we focus the attention at $\theta = 180°$, i.e. at the toroidal gap of the wall, not only the large perturbation localized at the poloidal gap at $\phi = 112.5°$ is strongly reduced by the decoupler, but also smaller error fields at other toroidal angles.

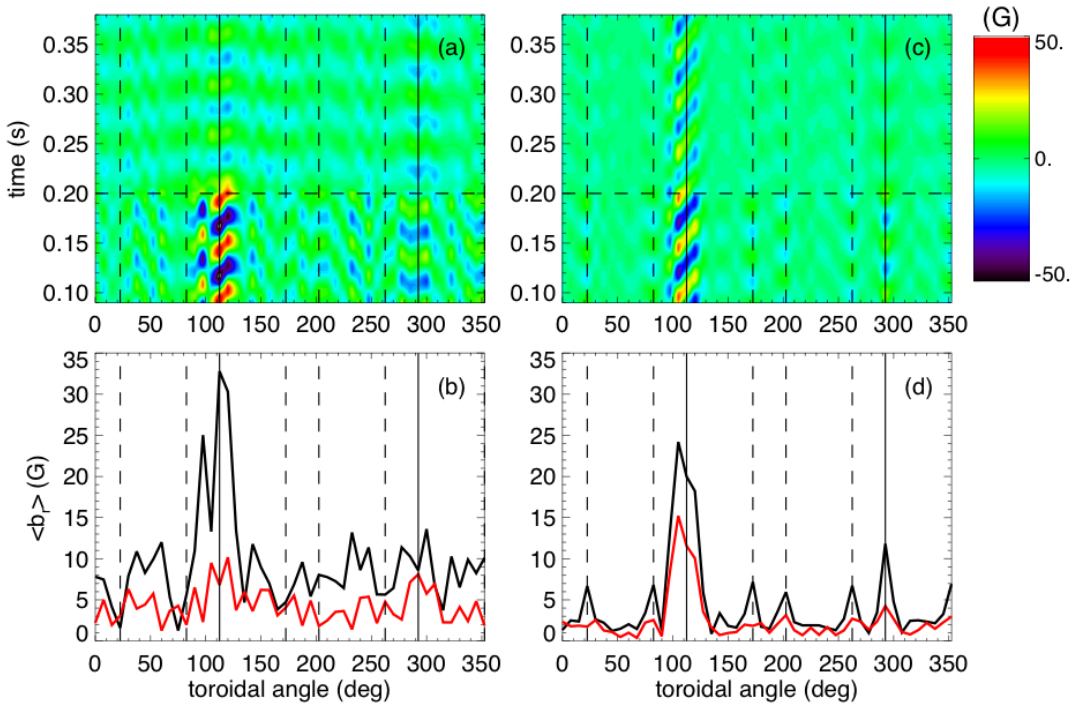

Figure 6.4: Contour plot of the radial magnetic field as a function of toroidal angle and time at (a) $\theta = 180°$ and (c) $\theta = 270°$ for the same vacuum discharge of Figure 6.1 with the dynamic decoupler turned on from $0.2s$. (b) and (d) Time average of $|b_r|$ as function of the toroidal angle in periods without ($t = 0.1 - 0.2s$, black line) and with ($t = 0.25 - 0.35s$, red line) the dynamic decoupler at (b) $\theta = 180°$ and (d) $\theta = 270°$.

Far from special features of the wall in the poloidal direction, for example at $\theta = 270°$, the dynamic decoupler reduces the error fields localized near each porthole, as shown in Figure 6.4(d). Note that a residual error field is still uncorrected at $\phi = 112.5°$. This is probably due to approximations in the decoupler or errors in the transfer function identification.

The decoupling schemes above described reveal to be a powerful tool to compensate for the 3D wall dynamic response and thus to produce the desired B_r distribution at the plasma surface. This is of great importance for the experiments on helical equilibria induced by applying helical boundary conditions through magnetic feedback, since error fields induced by 3D effects can spoil the good confinement properties of these states. For the next RFX-mod campaign, dedicated experiments will be performed in order to investigate these effects and the role of the plasma in amplifying or shielding $3D$ error fields.

A sufficiently large number of sensors and actuators are mandatory to realize this type of dynamic decoupling. Recent experiments in DIII-D have shown the importance of multi-mode control in very high-β regimes [107]. Decoupling may

be important in these cases, where magnetic feedback should target a certain harmonic without producing other error fields with different helicities, which may excite marginally stable modes. The relevance of a frequency-dependent scheme for the compensation of magnetic sensors from spurious $n = 1$ fields in DIII-D experiments will be presented in the next Chapter [45, 66].

6.3 Error field effects in high-plasma current discharges

As discussed in the previous Section, the analysis of vacuum field experiments reveals that by applying a $(1, -7)$ external radial magnetic field through magnetic feedback, a large error field with a radial magnetic field amplitude of about $25-35G$ is induced near the poloidal gap at $\phi = 112.5°$, as shown in Figure 6.4. This error field can have a detrimental effect on the plasma performance, since it enhances the plasma-wall interaction and represents, especially at high-plasma current an operational limit, enhancing the heat load on localized areas of the wall.

The possible effects of this error field on plasma performance have been investigated by analyzing high-plasma current experiments with plasma current in the range $I_p = [1, 2]MA$, reversed parameter $F \in [-0.035, -0.015]$, and electron density normalized to the Greenwald density $n/n_g \in [0.06, 0.22]$.

A statistical analysis of the toroidal position where tearing modes are phase-locked during the flat-top phase has been performed and the outcome is reported in Figure 6.5(a). The distribution function has a maximum near $\phi = 112.5°$. Based on the analysis described in Section 6.2, it may be argued that an error field grows at this poloidal gap possibly induced by time-varying external magnetic field used to control the dominant $(1, -7)$ mode.

As aspected, this position also coincides with the region of maximum plasma-wall interaction. This has been inferred from the investigation of the local wall temperature increase along the torus, $\Delta T(\phi, \theta)$, detected by a system of thermocouple sensors placed outside the vessel [108].

Since the plasma heat must diffuse from the interaction region on the graphite wall to the thermocouples, the $\Delta T(\phi, \theta)$ pattern is computed from the difference of the signals measured $1min$ before the plasma discharge and $12min$ later. To quantify the total increase of the wall temperature along the torus, named $\Delta T^{tot}(\phi, \theta)$, the data of each thermocouple which are higher than the 50% of the maximum temperature jump along the toroidal and poloidal directions have been collected. The wall temperature data have thus been summed, for each toroidal and poloidal position, and for each discharge of the database mentioned before. The result of this analysis is reported in Figure 6.5(b).

The main plasma power dissipation at the wall is concentrated at the poloidal position $\theta = 67.5°$. This may be due to the Shafranov shift, which moves the plasma column in the outboard side of the machine with respect to the geometrical axis. The $\Delta T^{tot}(\phi, \theta)$ signal at this poloidal angle and along the toroidal direction

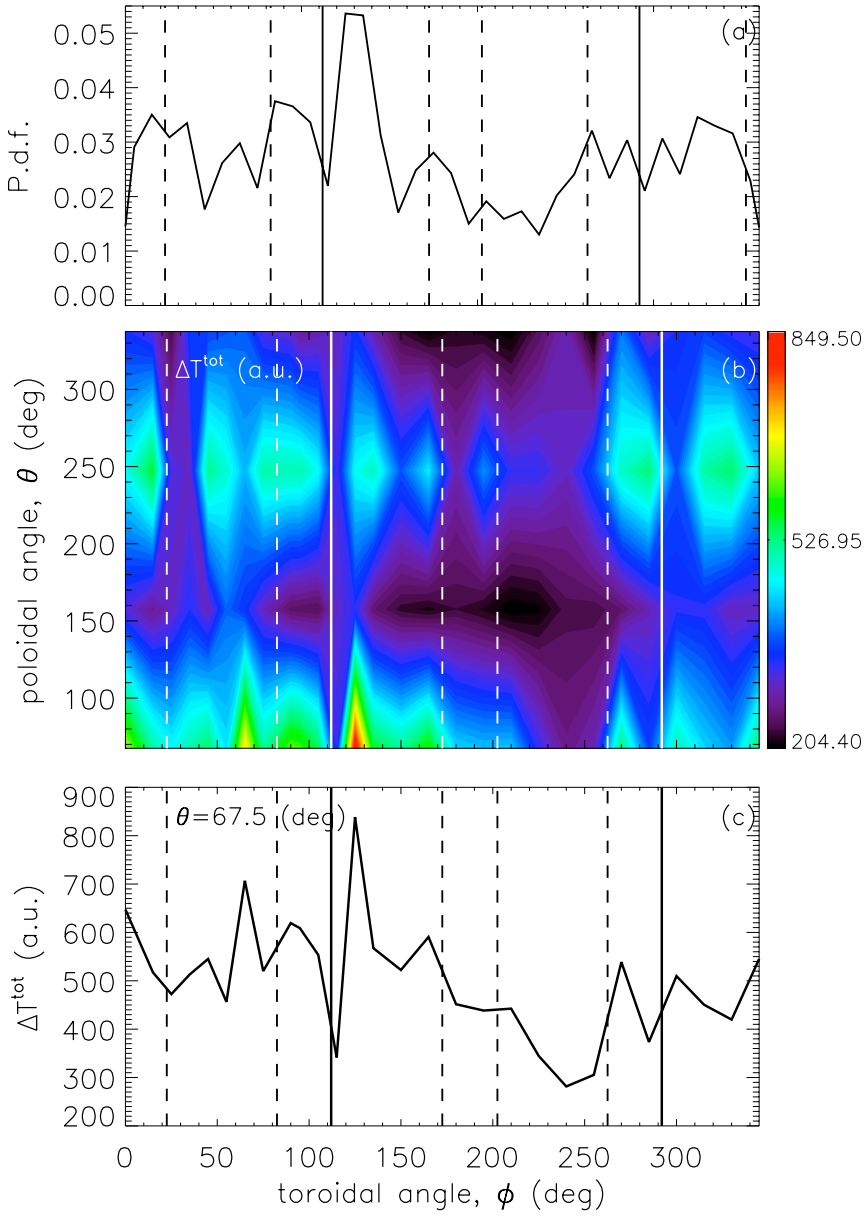

Figure 6.5: (a) Distributions of the toroidal position where tearing modes are phase-locked during the flat-top phase. (b) Contour plot of the total wall temperature increase along the torus. (c) Distribution of the total wall temperature increase as a function of the toroidal angle and at fixed poloidal position $\theta = 67.5°$. The vertical continuous lines indicate the two poloidal gaps, the vertical dashed lines indicate the toroidal angle of some large portholes.

is shown in Figure 6.5(c). The toroidal region with the largest increase of the wall temperature, and thus strong plasma-wall interaction, corresponds to the position where tearing modes usually phase-locked, as shown in Figure 6.5(a).

The analyses of high-plasma current experiments reveal that uncorrected source of error fields, such as the error field localized at the poloidal gap at $\phi = 112.5°$ and induced by external time-varying 3D magnetic fields, can enhance the plasma-wall interaction and their negative effects are expected to became relevant as the plasma current is raised. In fact, since the thermal loads deposited on the wall increase with the plasma current, plasma-wall interaction not spread along the torus but localized in some regions is a severe limit in achieving sustained plasmas with good properties. A promising solution to overcome these limitations in the next experimental campaign may be to correct the error field described above using the dynamic decoupler scheme presented in this Chapter.

CHAPTER 7

Improved dynamic response of magnetic feedback in DIII-D with AC compensation

The work presented in this Chapter has been done thanks to a collaboration with the DIII-D team at General Atomics, San Diego, USA. It will be shown that the dynamic response of the 3D wall structures to any time-varying magnetic field, such as that produced by the active coils, needs in some cases to be accounted for when doing magnetic feedback control. The results described here are analogous and have been to some extent stimulated by the work done at RFX-mod, and presented in Chapters 4 and 6. In the feedback scheme normally used in DIII-D, external magnetic fields produced, for instance, by currents in the active or axi-symmetric coils, are subtracted in real-time from the poloidal magnetic field signals used in the feedback loop. The couplings among the sensors and each external magnetic field source are measured in calibration shots at the beginning of each experimental campaign, but usually only the zero-frequency couplings are taken into account in the feedback algorithm. This approach is commonly called DC compensation. Nonetheless, it will be shown that the eddy-currents induced in the wall by the temporal variation of the external magnetic fields introduce frequency-dependent, or AC, contributions. An AC compensation scheme accounting for these effects has been implemented in the plasma control system and tested in real-time. Analyses have been carried out in dry-shots, but also in Ohmic and high-β plasmas, and have shown that, not taking into account these AC effects, unwanted error fields are introduced in the feedback control scheme. It will be shown that such effects may become particularly important at high-β, where uncorrected error fields are strongly amplified by the plasma.

7.1 Dynamic response of the wall to time-varying external magnetic fields

As described in Chapters 4 and 6 for the RFX-mod case, 3D wall structures modify the pattern of eddy-currents induced in the wall by external magnetic fields varying in time. Such effects introduce error fields that can reduce the plasma performance or in any case affect the feedback action. To correct these effects, an advanced magnetic feedback scheme named dynamic decoupler [91] has been developed and tested in RFX-mod with satisfactory results.

The frequency response of the wall to external magnetic fields has also been studied in the DIII-D tokamak, in the framework of a collaboration between the DIII-D and RFX-mod teams. This collaboration gave the opportunity to analyze the similarities and differences between the two feedback systems and to share a common language. In particular, this Thesis work investigated how the dynamic response of a 3D wall to external magnetic fields can be identified and used to optimize the magnetic feedback for RWM and error field control [45, 66]. In the DIII-D control algorithm, the external magnetic fields, such as those produced by the feedback and axisymmetric coils, are subtracted from the magnetic field signals. Nonetheless, up to now only their static component is accounted for. In this way, the response of the plasma can be calculated, which is the quantity the feedback reacts to. Note that in this approach the eddy-currents induced in the wall are neglected. In this Chapter, the relevance of frequency-dependent effects in the compensation of the magnetic sensors from spurious $n = 1$ fields due to the coupling with the feedback and axisymmetric coils will be discussed, along with its possible impact on Ohmic and high-β plasmas.

7.2 DC *vs* AC compensation of the sensor signals

As described in Chapter 2, the DIII-D tokamak is equipped with a system of active coils both external (so-called C-coils) and internal (I-coils) to the vacuum vessel, and has tested various feedback schemes for both dynamic error field correction and direct suppression of RWMs in Ohmic and high-β plasmas. In both types of plasmas, the targeted mode has toroidal mode number $n = 1$. For this reason, the poloidal magnetic field sensors used for feedback are pairs of sensors located 180° apart and hardware subtraction of opposite sensor signals allows for the elimination of even-n harmonics.

The $n = 1$ B_p sensors detect not only the $n = 1$ field produced by the plasma, but also spurious $n = 1$ contributions from other magnetic field sources external to the plasma, such as feedback coils, misaligned axi-symmetric coils, or contributions due to pick-up by non perfectly planar sensors. Usually these $n = 1$ fields are compensated for in real-time with a scheme that considers only the static couplings between the various coils (internal and external active coils, field-shaping, Ohmic,

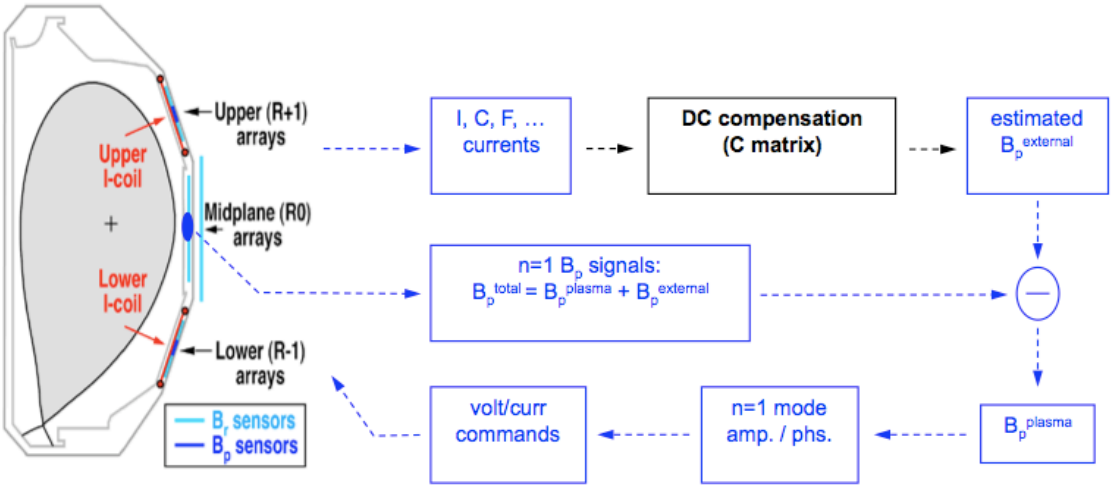

Figure 7.1: Scheme of the feedback control algorithm in the DIII-D tokamak.

and toroidal field coils) and the sensors. The static coupling coefficients, which are stored in the co-called C Matrix, are measured in dry calibration shots, at the beginning of each experimental campaign, by driving a stationary current in the various coils, which is the same as evaluating the corresponding transfer functions at $f = 0Hz$.

The so-called DC compensation algorithm is schematically represented in Figure 7.1 and allows for the computation of the plasma response, defined as $B_p^{plasma} = B_p^{total} - B_p^{ext,DC}$, where B_p^{total} is the measured poloidal magnetic field and $B_p^{ext,DC}$ is the static external magnetic field. By Fourier analyzing the plasma response signal, the $n = 1$ poloidal magnetic field amplitude and phase are calculated, which are then processed by the control algorithm. The resulting quantities are sent to the coil power amplifiers as current/voltage references, and the feedback control loop is thus closed.

In the DC compensation approach, the effects due to eddy-currents induced in the wall structures by time-dependent magnetic fields produced by the various coils are not taken into account, since the C-matrix considers only the static coupling coefficients between each actuator and sensor. As mentioned above, the coupling coefficients have been calculated by analyzing dry calibration shots, in which the various coils, one by one, are fed with a square pulse and the poloidal magnetic field in each sensor is measured.

In the calibration discharges, the active coil currents are also varied with sinusoidal waveforms at various frequencies. This allows to measure the transfer function between the various coils and the sensors as a function of frequency. Examples of the transfer functions between the feedback coils and the poloidal magnetic field sensor at $\phi = 67°$ are shown in Figure 7.2. The transfer functions have been identified by Fourier analyzing the feedback current and poloidal mag-

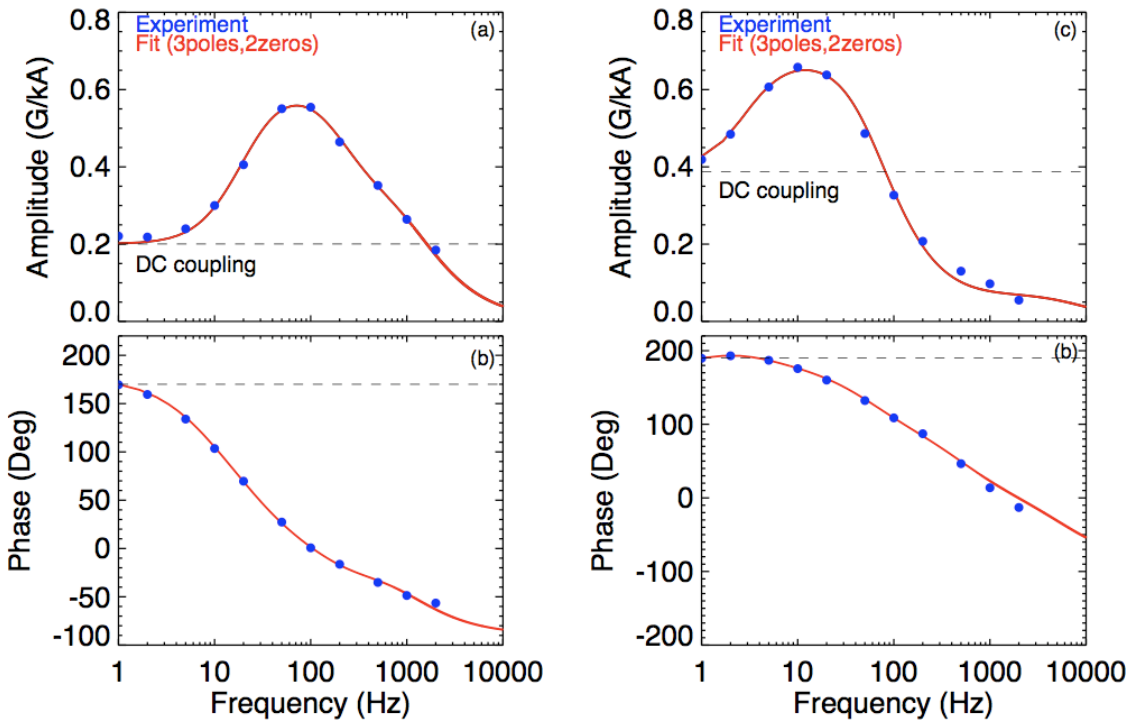

Figure 7.2: Measured transfer functions (squares) between (a)-(b) the poloidal magnetic field sensor at $\phi = 67°$ and the upper I-coil pair $\phi = 90°$ and (c)-(d) the same poloidal magnetic field sensor and the C-coil at $\phi = 79°$. The red curve represents the fit of the measured data.

netic field signals. The measured couplings are shown in the Figure with blue dots, while the red curve represents the fit of the measured frequency response data. Note the difference between the DC and AC values of the transfer function: for example, the amplitude of the couplings to the I-coil reveals a strong peak near 100Hz and a 180° phase shift at the same frequency, represented by a dashed line. Instead, the transfer function of the C-coil has a peak at 10 Hz and the phase-shift is about 30° with respect to the DC value.

In this Thesis work, the relevance of AC effects on RWM control and on error field correction is investigated. The spurious $n = 1$ contributions to the B_p signals are computed using the transfer functions between the different coils (feedback and field-shaping coils) and the poloidal magnetic field sensors. This scheme, which is similar to the one discussed in [78], is called AC compensation. Note that in the present case the AC compensation is limited to effects introduced by external magnetic field sources, but AC contributions from the plasma current may be also expected, in particular during the current ramp-up phase.

7.3 AC effects due to the field-shaping coils

Figure 7.3 represents an example of a calibration shot for the identification of the transfer function between the poloidal magnetic field sensor at $\phi = 67°$ and a field-shaping coil, called F7A. As shown in Figure 7.3(a), the current in the field-shaping coil is pulsed and the $n = 1$ B_p signal is reported, in blue, in the panel (b). The DC coupling coefficient, i.e. the value of the transfer function at $f = 0Hz$, can be simply computed from the B_p value reached during the stationary part of the F-coil waveform, while the AC couplings are computed using a Matlab fitting routine called PEM. Given as inputs the field-shaping coil current and the poloidal magnetic field signals as a function of time, the PEM estimates the model parameters using an iterative error minimization method [96]. The result is reported in Figures 7.3(c) and (d), and the transfer function identified has 2 poles and 1 zero.

To assess the relevance of AC effects, the $n = 1$ poloidal magnetic field signal

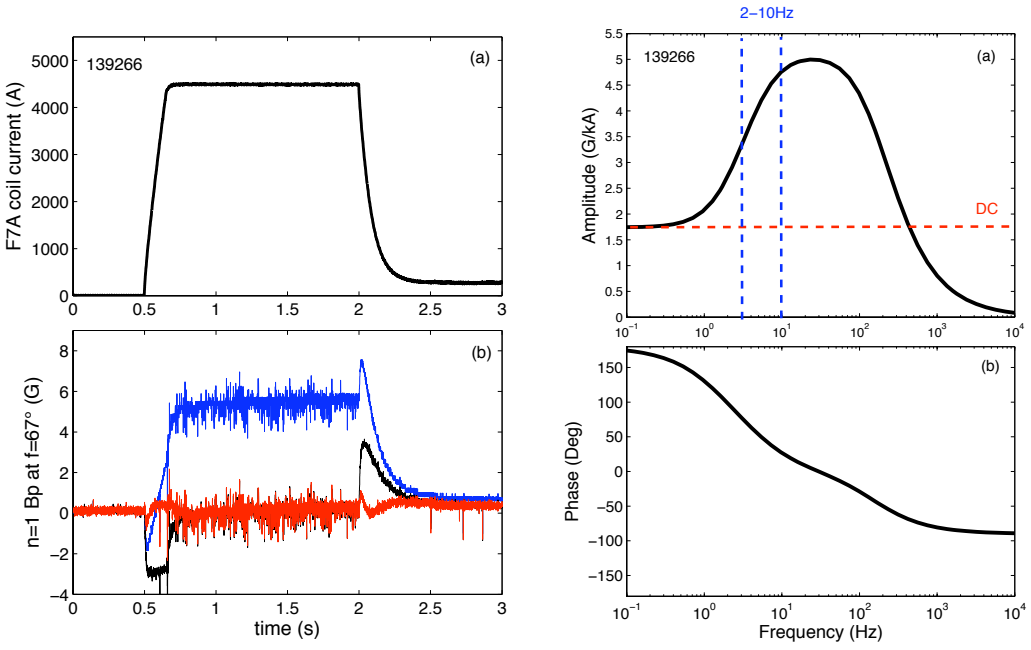

Figure 7.3: (a) Current in one of the DIII-D field shaping coils (coil F7A), in a vacuum discharge (139266), in which only this coil was turned on. (b) Poloidal magnetic field from the hardware difference of sensors 180° apart, to extract the $n = 1$ component, without any compensation of the spurious $n = 1$ field from the F7A coil (blue), with offline DC compensation (black), and with offline AC compensation (red). (c)-(d) Transfer function between the F7A coil and the magnetic B_p signal in the left figure.

at $\phi = 67°$ of the vacuum field experiment above described, has been DC and AC compensated offline and the two estimates are plotted in Figure 7.3(b) in black and in red, respectively. In the stationary phase the two approaches are equivalent, while, during the rising and decaying phase of the square pulse, the AC compensation performs significantly better. The F-coil current rises and decays in about $0.1 - 0.5s$, which correspond to frequencies in the range $2 - 10Hz$. These time scales are similar to the ones in which the F-coils vary, for example, during the plasma current ramp-up. At these frequencies, as indicated in Figures 7.3(c) and (d), the transfer function deviates significantly from its DC value, and the phase has a 180° shift with respect to the DC case. The difference between DC and

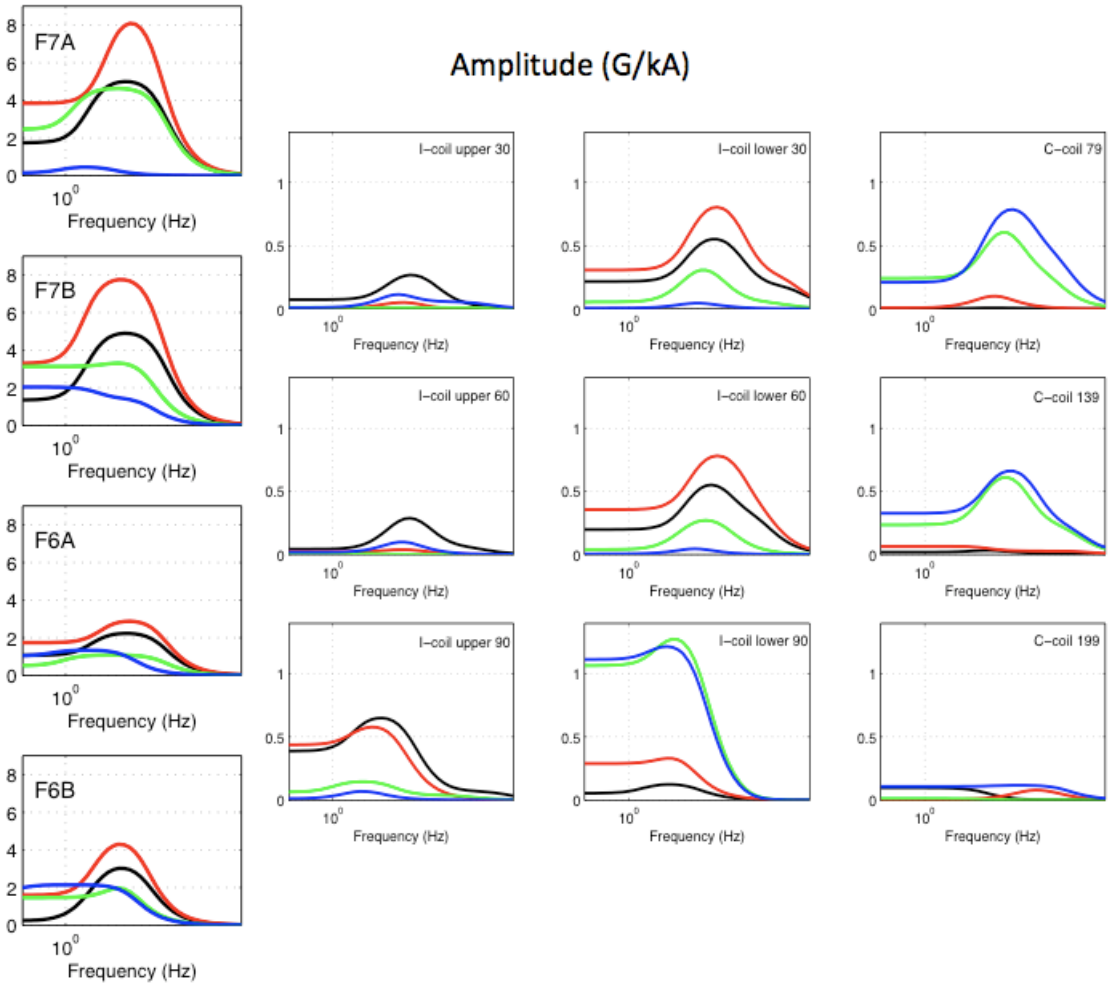

Figure 7.4: (a)-(b) Amplitude of the transfer functions between the poloidal magnetic field sensors at $\phi = 67°$ (black), $\phi = 97°$ (red), $\phi = 127°$ (green), $\phi = 157°$ (blue) and F-coils, upper I-coil set and lower I-coil set with respect to the midplane, and C-coils.

AC compensated signals amount to a few Gauss during transients, which can be significant especially at high-β, where small error fields may be strongly amplified through resonant field-amplification [60].

The vacuum field experiment above described is just an example of the analyses that have be carried out on all the calibration shots. In an analogous way, the transfer functions between each $n = 1$ B_p sensor and various coils have been identified. Figure 7.4 reports the amplitudes of the transfer functions between $n = 1$ B_p sensors and the field-shaping coils ($F7A, F7B, F6A, F6B$), the $n = 1$ B_p sensors and the I-coil upper and lower set with respect to the midplane, and $n = 1$ B_p sensors and the C-coils. As will be described in Section 7.5, the same transfer functions have been implemented in a digital filter to realize a frequency-dependent scheme for the real-time compensation of the magnetic signals.

7.4 AC effects in experiments for the control of current-driven RWMs in Ohmic plasmas

The relevance of AC effects for magnetic sensor compensation has been investigated also by analyzing a set of Ohmic plasma experiments, in which a fast plasma current ramp-up has been pre-programmed. In this way, current gradients form, which destabilize a class of RWMs, called current-driven RWMs. To study the effects of feedback control parameters on RWM physics and to test new feedback control strategies, as in this case, Ohmic plasmas are suitable due to their highly reproducible behavior.

One of these Ohmic plasma experiments is reported in Figure 7.5. The plasma current, as shown in Figure 7.5(a), is ramped and the edge safety factor decreases in time, crossing different $n = 1$ resonances. In this experiment, the DC compensation was used in real-time and the proportional gain applied in the feedback loop was too low to suppress the mode, which starts growing around $t = 0.45s$, as shown in Figure 7.5(c) by the rapid oscillation in the $n = 1$ poloidal magnetic field signal. At this time instant, the edge safety factor approaches the resonance $q_{95} = 4$.

The DC external magnetic fields induced by the various coils have been subtracted offline from the $n = 1$ poloidal magnetic field signals, as in the experiment, and the DC compensated signals calculated in this way are shown in black in Figure 7.6. For comparison, the poloidal magnetic field measurements have been compensated offline with the AC components. In particular, the AC compensated signals have been calculated in two ways: compensating the AC effects induced by the feedback coils only (in red) and by the feedback and the field-shaping coils (in green).

The DC and AC compensated signals show some significant differences at different time scales: the mode growth time scale and the F-coil current variation time scale. When the mode starts growing, an oscillation is visible in both the DC

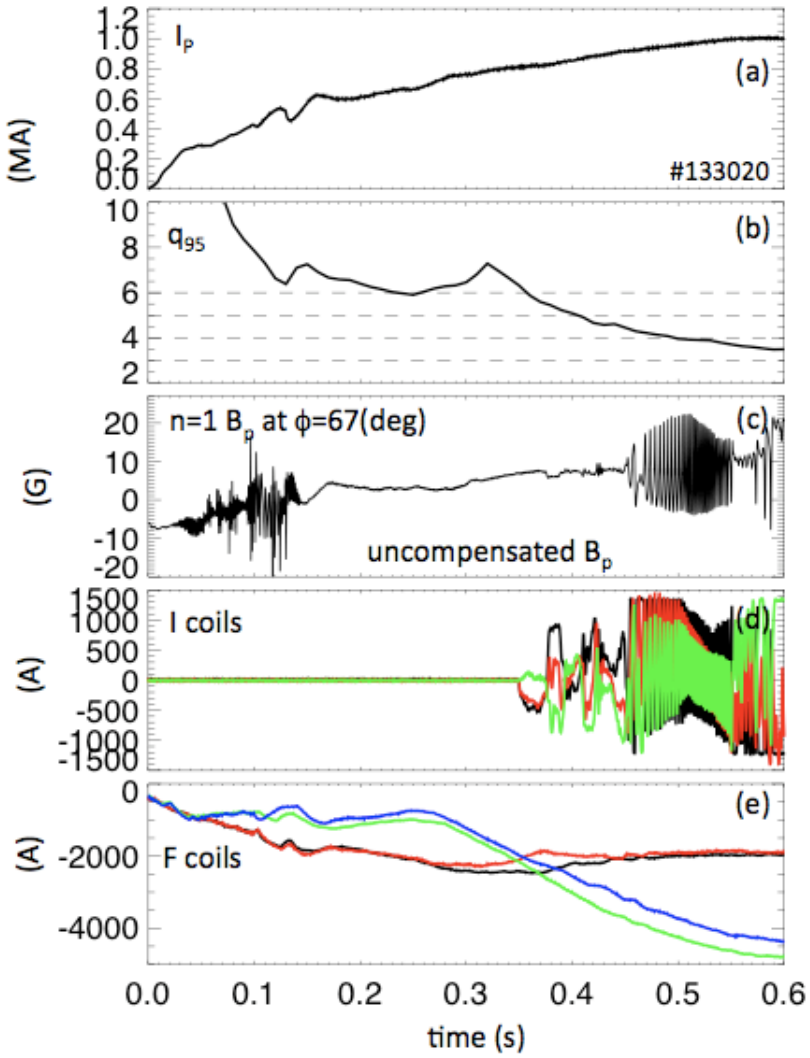

Figure 7.5: (a) Plasma current, (b) edge safety factor, (c) uncompensated $n = 1$ B_p signals at $\phi = 67°$, (d) I-coil currents, (e) F-coil currents of an Ohmic plasma experiment (133020) with an unstable current-driven RWM.

and AC compensated signals, but the two oscillations are almost out of phase, and the AC one is about two Gauss larger. This is due to the fact that, at frequencies typical of RWM growth and rotation, of about $f \approx 20 - 200Hz$, the I-coil-to-B_p sensor transfer function is very different from the DC value, as shown in Figures 7.2(a) and (b). In particular, the I-coil transfer function has a 180° phase shift in the above frequency range, which explains the out-of-phase oscillation in the DC and AC B_p compensated signals. Moreover, at a much slower time scale of about $200ms$, there is a significant difference between the two compensation approaches, which is introduced basically by the temporal variation of the F-coil currents. This discrepancy is not the same for all the poloidal field sensors, but it has a $n = 1$

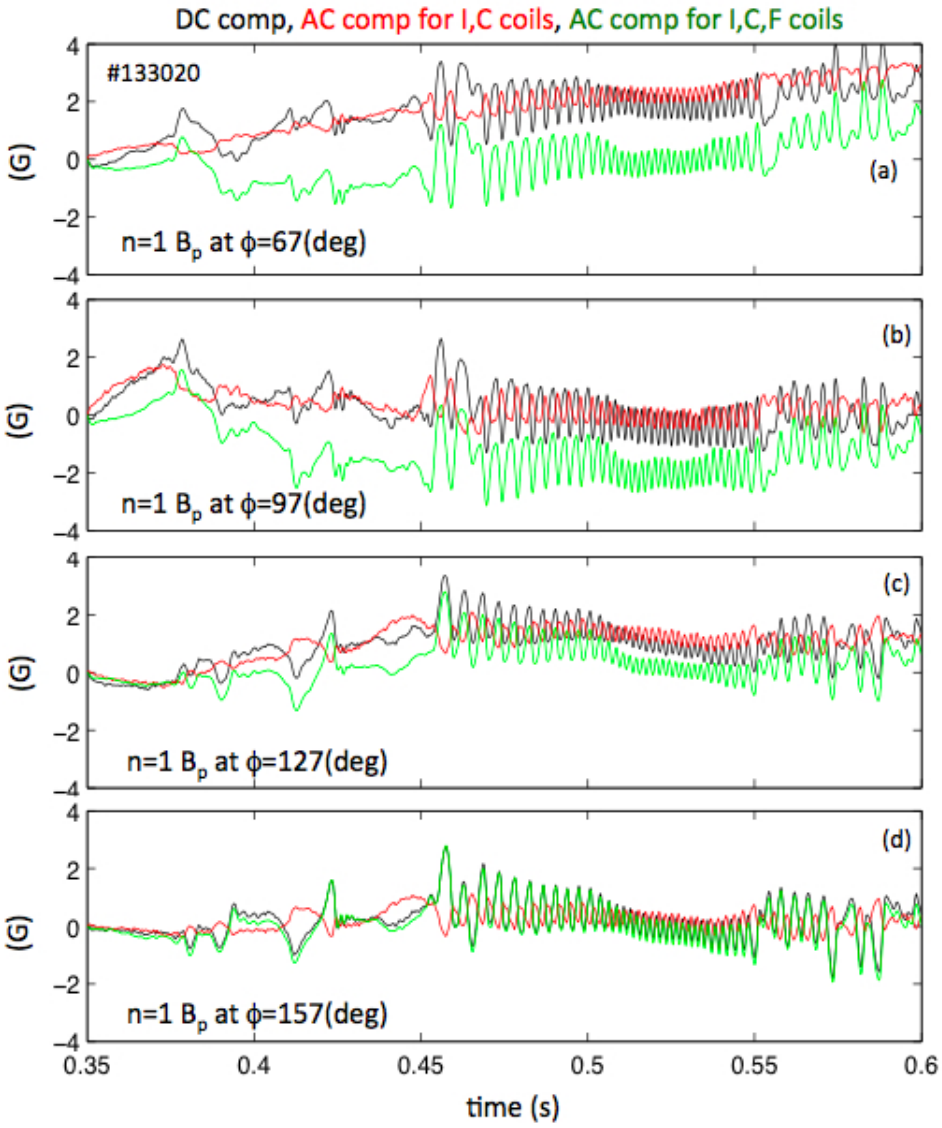

Figure 7.6: DC and AC compensation for the $n = 1$ poloidal magentic field signals at $\phi = 67°, 97°, 127°, 157°$. The DC compensated signals are show in black, AC compensated for the feedback coils in red, while AC compensated for feedback and field-shaping coils in green. The signals corresponds to an Ohmic plasma experiment (132020), which crosses the $q_{95} \approx 4$ at $t = 0.45s$.

toroidal dependence. It may be argued that, not compensating the AC effect, a $n = 1$ error field is introduced by the feedback system.

The $n = 1$ mode amplitude and phase have been computed from the offline compensated $n = 1$ poloidal magnetic field signals and the results are shown in Figure 7.7. As usual in DIII-D, the feedback signals are offset subtracted just before the feedback control is turned on, which happens here at t=0.35s, as shown

in the time traces of the I-coil currents in Figure 7.5(d). The offset subtraction is performed to neglect unknown couplings to axisymmetric fields, offsets in the signals, and other unknown error fields.

The difference among the DC and AC compensated n = 1 amplitudes, reported in Figure 7.7(b), amounts to about $2G$. Neglecting AC effects introduces an error in the $n = 1$ mode amplitude, especially when the mode starts growing at $t = 0.45s$, which may have a destabilizing effect on current-driven RWMs. As shown in Figure 7.7(c), the AC compensation does not affect significantly the $n = 1$ phase.

The analysis of this Ohmic plasma experiment suggests that, not including the AC effects in the feedback scheme may produce deleterious effects: a $n = 1$ error field, with a non-negligible amplitude, may be artificially introduced by the feedback coils themselves and a RWM mode may be actually further destabilized in its initial growing phase. If the gains are sufficiently large, the feedback may be able to compensate for this effect, even though at the expense of additional coil current. Compensating correctly may thus both save coil current and enlarge the range of stable gains.

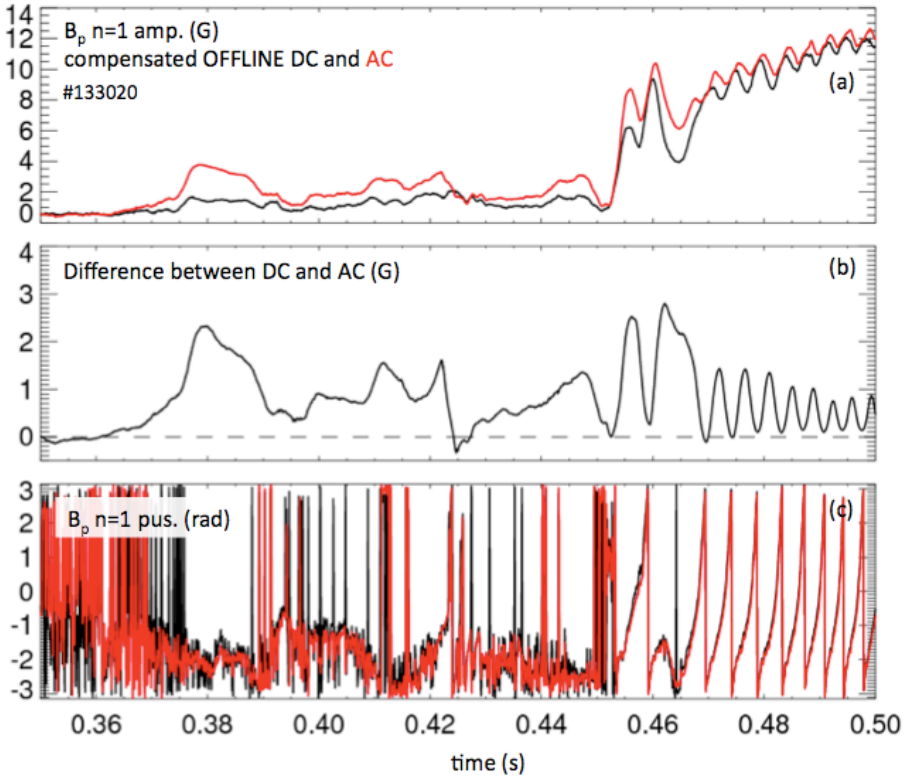

Figure 7.7: (a) B_p amplitude and (c) phase of the $n = 1$ mode after offline DC (black) and AC (red) compensation, and (b) difference among these DC and AC compensated $n = 1$ amplitudes for the same discharge plotted in Figure 7.5.

7.5 AC effects on dynamic error field correction

The analyses reported in the previous Sections show the importance of taking into account the frequency response of the wall in the sensor compensation algorithm. To assess its relevance when doing magnetic feedback control, an AC compensation scheme, which uses the transfer functions plotted in Figure 7.4, has been implemented in real-time as a discrete digital filter. The computation time increases with respect to the DC compensation, but it is still lower than the cycle-time of the DIII-D plasma control system of is $11\mu s$.

During the 2010 DIII-D experimental campaign, the AC compensation algorithm has been tested for the first time in real-time in Ohmic discharges. To compare the difference between the DC and AC compensation schemes, two very similar Ohmic discharges have been performed with the same plasma settings and feedback parameters, with AC and DC compensation respectively. Figure 7.8 represents these two experiments. Note that they are very similar, as shown by the time traces of the plasma current, the edge safety factor, the electron density and of the uncompensated $n = 1$ B_p signal at $\phi = 67°$, reported in Figure 7.8, and by the time trace of the field-shaping coil in Figure 7.9(a). The difference between the two experiments, as mentioned before, is only related to the compensation algorithm applied in the plasma control system: the #141242 shown in back uses the DC compensation, instead, the #141243 in red the AC compensation.

Even though the plasma current is ramped and the edge safety factor decreases in time crossing different $n = 1$ resonances, unfortunately in these discharges the targeted RWM was not strongly unstable, likely due to different discharge setting-up and wall conditions with respect to previous experiments [107, 109]. The two compensation schemes could thus only be compared with respect to dynamic error field correction, which is used, as described in Chapter 2, to compensate the error field components that resonate with the RWM and vary very slowly in time.

In these plasmas, it is expected that the AC effects are mainly introduced by the field-shaping coil currents, since the feedback coil currents vary on time scales not relevant for AC compensation, basically because there is no unstable RWM. As described in Section 7.3, for the F-coils the AC effects are important at relatively long time scales of $100 - 500ms$, which are also the typical F-coil variation time scales in these experiments, as shown in Figure 7.9(a). The external magnetic field produced at the $n = 1$ B_p sensor at $\phi = 67°$, as calculated by the feedback scheme, is shown in Figure 7.9(d), and the estimate is quite different for the two experiments due to the different compensation algorithm.

The $n = 1$ B_p signals have then compensated in real-time for the spurious $n = 1$ magnetic fields calculated with the two methods and an example of compensated $n = 1$ B_p signal at $\phi = 67°$ is shown in 7.9(e). Since the estimated external magnetic field, for each sensor position, differs in the two experiments, the compensated $n = 1$ poloidal magnetic field signal is different.

By Fourier analyzing the compensated $n = 1$ B_p signals, the $n = 1$ amplitude

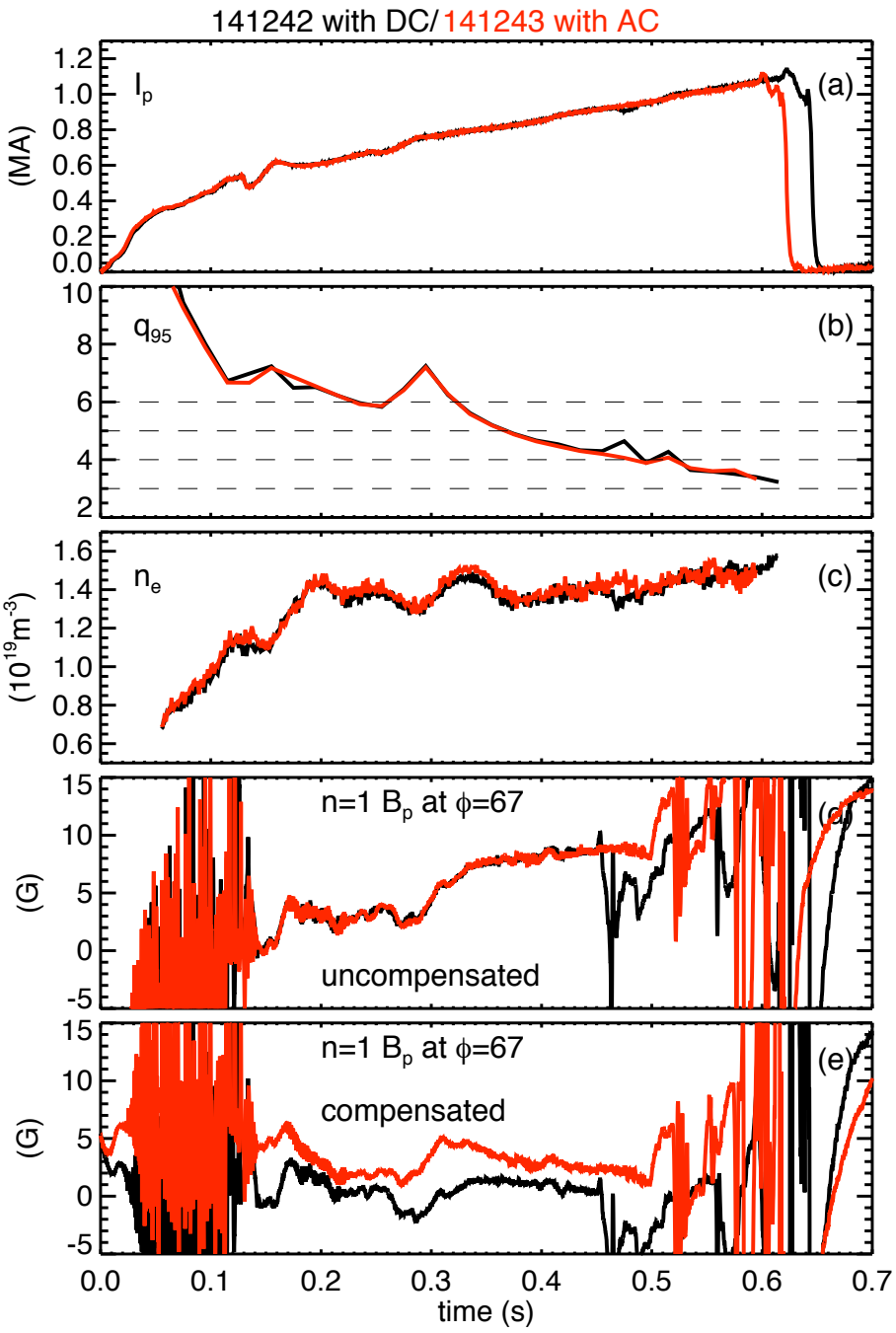

Figure 7.8: (a) Plasma current, (b) edge safety factor, (c) electron density, (d) uncompensated and (e) compensated $n = 1$ B_p signals at $\phi = 67°$ for two similar DIII-D Ohmic discharges with DC (black) (141242) and AC (red) (141243). The AC case included compensation of the spurious $n = 1$ field from the I, C, and F-coils.

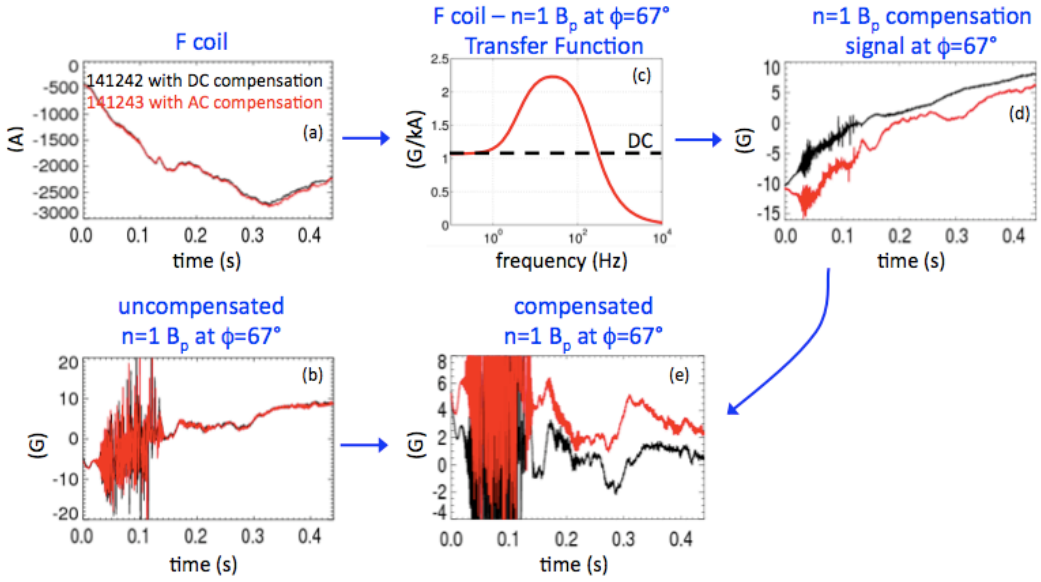

Figure 7.9: (a) F-coil current, (b) uncompensated $n = 1$ B_p signal at $\phi = 67°$, (c) transfer function between a F-coil and the $n = 1$ B_p signal at $\phi = 67°$, (d) external magnetic field produced by the field-shaping and the feedback coils, (e) compensated $n = 1$ B_p signal at $\phi = 67°$. The analyses have been carried out for the same experiments in Figure 7.8.

of the B_p field has been estimated and the result is shown in Figure 7.10(a). The DC and AC compensated $n = 1$ amplitudes are significantly different. Including the AC effects reduces the estimated $n = 1$ amplitude from the plasma and, as a result, the request of coil current decreases, as shown in 7.10(b). This is due to the different compensation algorithm, not to shot-to-shot variations in the uncompensated signals or in the coil currents, which are much lower. The main AC effects are associated here, as describe before, with the temporal dynamics of the F-coil currents, not with that of the C or I-coils, which do not vary significantly since no unstable modes are present. The B_p signals of the discharge with DC compensation have also been compensated offline with the AC algorithm. The result, displayed in blue in Figure 7.10(a), is very similar to the case with AC compensation in real-time, confirming that the differences observed are really due to the compensation algorithm.

These results suggest that AC effects may be important in these experiments. Not taking them into account may introduce unwanted error fields in the feedback loop. In these low-β plasmas, such error fields do not make a big difference, since they are not significantly amplified. This is probably the reason why the two discharges discussed above are not so different. Nonetheless, the AC effects could be more important at high-β, as it is suggested by the analysis presented in the following Section.

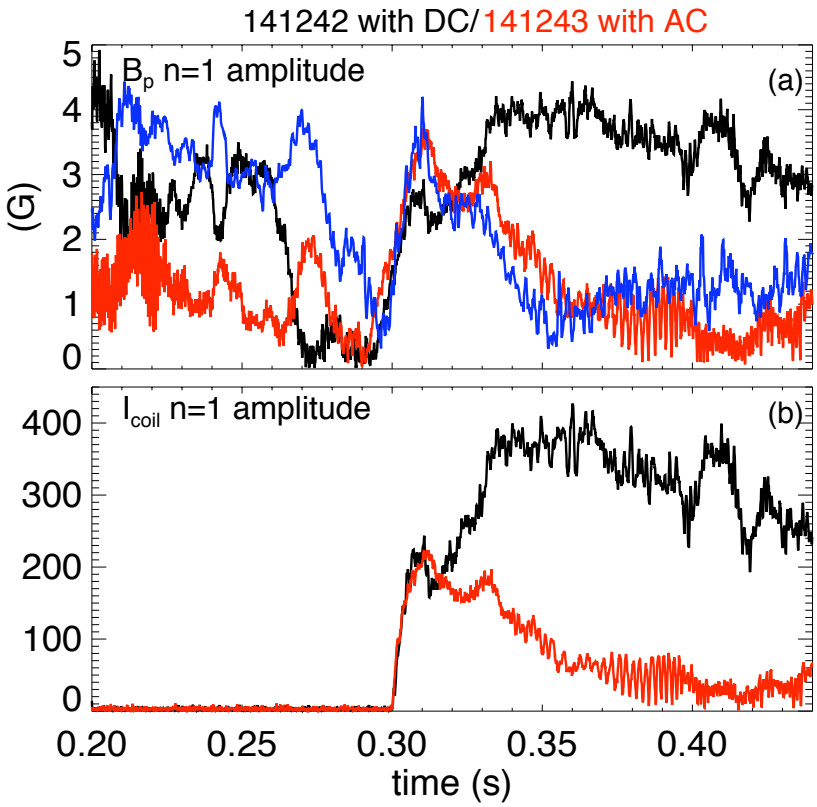

Figure 7.10: $n = 1$ mode amplitude of (a) the poloidal magnetic field and (b) the I-coil current for the two discharges plotted in Figure 7.12, with DC (black) and AC (red) compensation algorithm. The blue trace displays the result of doing AC compensation offline to the case with DC compensation done in real-time during the discharge. The poloidal field signals are offset subtracted just before feedback is turned on at $t = 0.3s$.

7.6 Possible relevance of AC effects in high-β plasmas

The possible relevance of AC compensation for magnetic feedback in high-β discharges has been evaluated by analyzing past experiments that used DC compensation, in which the high-β phase had been terminated by a RWM. In particular, a case where the β-collapse is triggered by a fishbone-driven RWM [56] has been analyzed.

In the discharge, reported in Figure 7.11, starting from $t \approx 1.78s$ a series of off-axis fishbones are rapidly rotating at frequency up to $3kHz$. Since this frequency range is higher than the sensor bandwidth, the magnetic field sensors do not detect the rapid perturbations due to the fishbone activity. Once the frequency of the magnetic field perturbation is reduced, to about $1kHz$ at $t = 1.85s$, the feedback becomes effective: the I-coils react and reduce significantly the amplitude of the

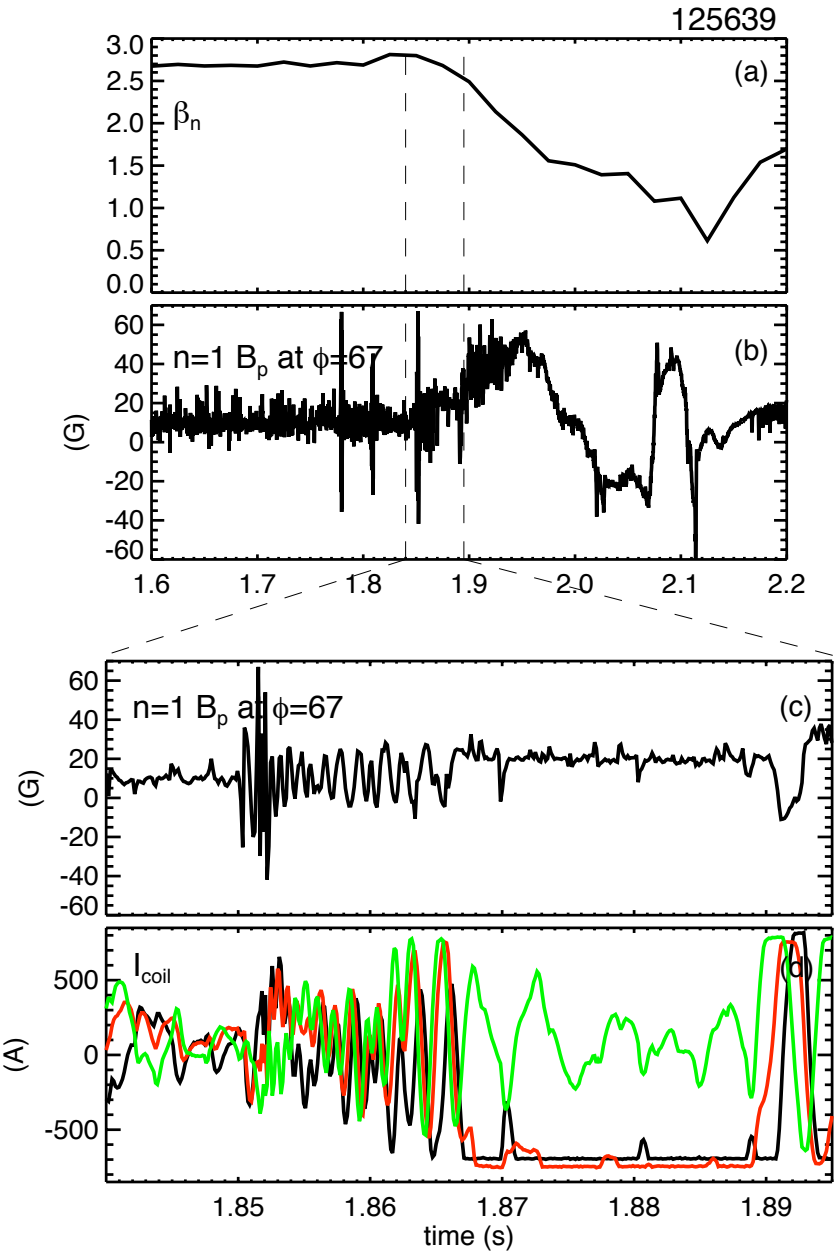

Figure 7.11: (a) Normalized beta, β_N proportional to $\sqrt{\beta_t \beta_p}$, (b) $n = 1$ poloidal magnetic field signal, and (c) zoom of the $n = 1$ poloidal magnetic field signal and of (d) the I-coil currents for a high-β discharge, in which the high-β phase is terminated by a fishbone-driven RWM.

fishbone-driven RWM. Nonetheless, a residual magnetic field oscillation remains, growing in time on a time scale much longer than that typical of an unstable RWM, as shown in Figure 7.11(c). The request of coil current slowly increases in time up to the point when the I-coil currents saturate, as shown in Figure 7.11(d), and

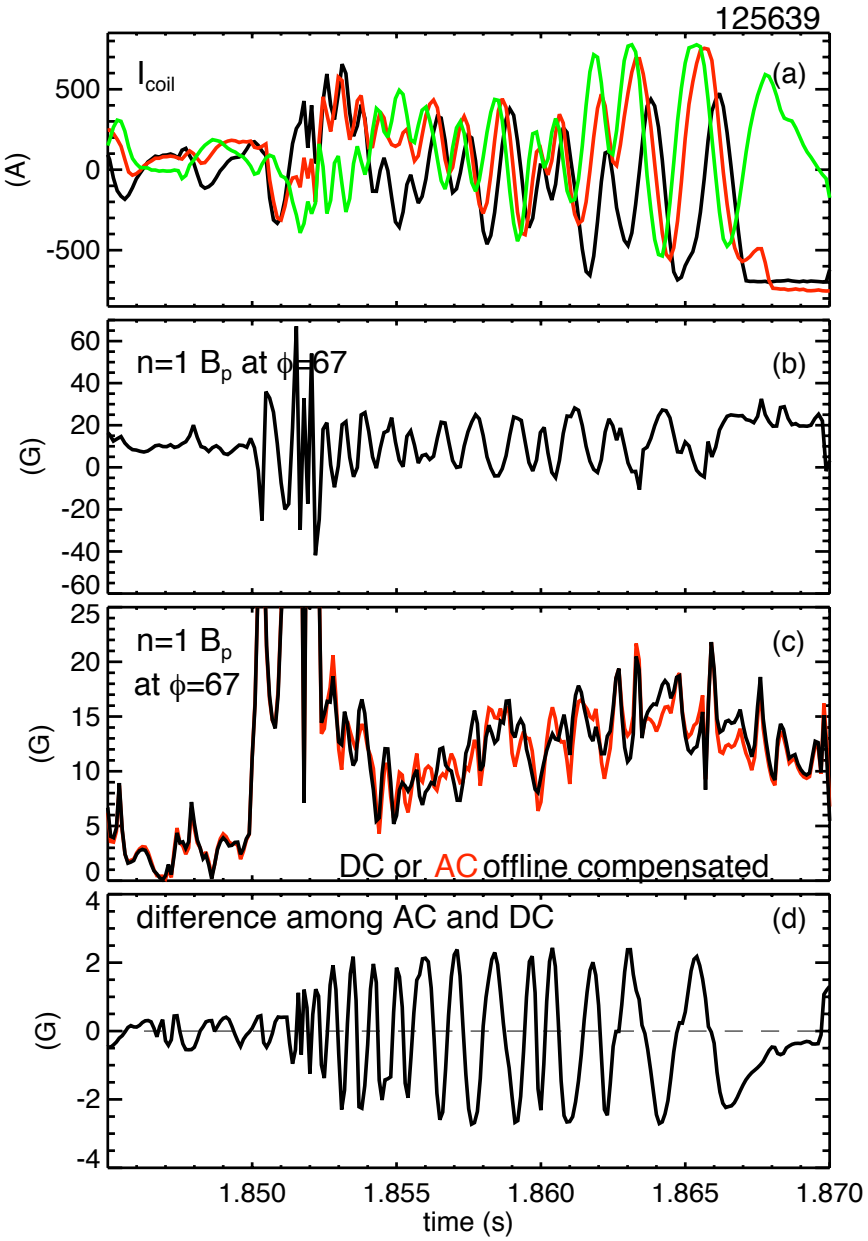

Figure 7.12: (a) I-coil currents, (b) $n = 1$ B_p signal at $\phi = 67°$, (c) B_p amplitude of the $n = 1$ mode after offline DC (black) and AC compensation (red), and (d) difference among these DC and AC compensated $n = 1$ amplitudes. The data refer to the same discharge in Figure 7.11.

the β-collapse occurs. AC effects may explain the origin of the residual oscillation eventually responsible for the β-collapse.

With a similar approach described in the previous section, the $n = 1$ B_p signals have been DC compensated, as in the experiment, and AC compensated offline.

The $n = 1$ poloidal magnetic field amplitude has then been computed and the results are shown in Figure 7.11(c) in black for the DC compensation and in red for the AC compensation. The difference between the $n = 1$ amplitudes computed in these two ways, which is shown in Figure 7.12(d), can be interpreted as an additional error field that the feedback system itself is producing. This difference amounts to about $4G$ Gauss, $10 - 20\%$ of the total signal, and oscillates, growing in time up to the β-collapse. Such an error field can be amplified strongly in these high-β plasmas and it may be the origin of the residual oscillation evidenced above.

Based on this analysis, it may be argued that an improved compensation of the sensor signals, which accounts also for the AC response of the wall, may be useful in conditions where the plasma is much less resilient to error fields such as at low-plasma rotation or high-β, where resonant-field-amplification phenomena can occur. For the coming 2011 experimental campaign, more extensive analyzes and experiments have been proposed to assess the relevance of AC effects for performance improvements, as will be described in Chapter 8.

CHAPTER 8

Conclusions and future work

This Chapter summarizes the original contributions and the main conclusions of this Thesis, and describes a series of experiments and analyses that could be done in the near future, both in RFX-mod and DIII-D, and have been stimulated by the results obtained in this work.

8.1 Conclusions

In this Thesis, various methods to optimize the magnetic feedback control in the RFP and the tokamak have been investigated, focusing the attention on two experiments, which are equipped with very flexible systems for the active control of MHD modes and error fields: the RFX-mod RFP and the DIII-D tokamak.

In particular, an optimization of the tearing mode and error field control has been carried out in RFX-mod to further improve the plasma performance at high-plasma current. Moreover, experiments where helical equilibria are controlled by imposing helical boundary conditions through magnetic feedback have been analyzed. Instead, in DIII-D the relevance of the wall-frequency response to any time-varying magnetic field has been investigated. A summary of the original contributions will be described in the following Sections.

8.1.1. Model-based optimization of tearing mode control in RFX-mod

Before this Thesis work, the mode control parameters in the RFX-mod controller had been identified with an empirical approach: a partial scan of proportional and derivative gains on selected tearing modes had been performed in the experiment. The criterium for choosing these gains was to decrease the non-axisymmetric $m = 1$ deformation of the LCFS due to tearing modes, in order to reduce the plasma-wall interaction. This was, in fact, the most severe limit for exploring high-plasma currents above $1MA$.

In this Thesis work, a model-based optimization of the mode feedback controller has been performed [42]. The optimization procedure consists in simulating the tearing mode dynamics with a non-linear torque-balance model named RFXlocking [84], scanning, for each mode, the proportional and derivative gains over a $2D$ grid. The aim has been to find a new set of gains that allows a reduction of the edge radial magnetic field due to tearing modes, maintaining at the same time these modes into rotation and avoiding coil current saturations.

The gain set predicted by the model has been tested in an experimental campaign and the results have been compared with the empirically-optimized ones. The main outcome of the model-based optimization is a reduction of the edge radial magnetic field with respect to the empirically-optimized case. Thanks in particular to an improved control of the secondary modes, the energy confinement time has a maximum in the proportional-derivative gain plane that corresponds to the lowest edge radial magnetic field, showing that the magnetic feedback control at the edge also has an effect on the plasma core, mitigating the magnetic field stochasticity.

Despite some stringent hypotheses, for example a uniform wall structure, the RFXlocking code is able to reproduce the non-linear dynamics of a spectrum of interacting tearing modes and it has been shown to provide a reliable way to tune

offline the gains of the RFX-mod controller. Developing multi-mode feedback schemes is expected to have a key role also for advanced tokamak operations, in which multiple low-n modes with $n = 1, 2, 3$ can appear sequentially as β increases [107].

8.1.2. Mode control and dynamic decoupling for error field correction in RFX-mod

In RFX-mod, the main error fields are induced in the ramp-up phase of the plasma current. In this phase, that lasts tens of milliseconds, the vertical magnetic field necessary to maintain the plasma in the correct position penetrates faster through the two poloidal gaps of the wall structure. This results in the formation of significant error fields, toroidally-localized at the position of the gaps, where the tearing modes tend to be phase-locked. The Fourier analysis shows that these error fields are mainly $m = 1$, low-n harmonics ($n = \pm 2, \pm 4, \pm 6$), which fall within the RWM spectrum.

Two different techniques have been applied to control these magnetic field errors [43]. The first one consists in applying the mode control on the error field harmonics. Several gains have been tested offline, using an e.m. model of the RFX-mod magnetic feedback system [95], leading to the conclusion that pure proportional gains are the most effective ones in reducing the error field amplitude. The second technique consists in controlling the error fields with pre-programmed coil currents computed with a dynamic decoupler described in [98].

Experiments show that multi-mode control and pre-programmed error field correction alone are not so effective in canceling the error fields. The best results are instead obtained when the two techniques are used simultaneously. The error field amplitude in this case is reduced to very low levels. Moreover, when both techniques are applied during the current ramp-up phase of the plasma discharge, the distribution function of the toroidal angle where the tearing modes are phase-locked is no more localized at the poloidal gaps, reducing the plasma-wall interaction phenomena otherwise localized there.

8.1.3. Optimization of helical equilibria controlled by magnetic feedback

In the 2010 RFX-mod experimental campaign, it has been shown that it is possible to control and sustain a $(1, -7)$ helical equilibrium with external 3D magnetic fields applied through magnetic feedback.
To optimize the magnetic feedback control of these states, the RFXlocking code has been modified by adding the possibility to apply helical boundary conditions with some chosen amplitude and phase, either rotating or static. The $(1, -7)$ mode dynamics has been simulated by varying the feedback parameters and the

amplitude and phase of the applied $3D$ magnetic field. Such scans can not be performed directly in RFX-mod, due to the large number of tests needed. In particular, this modified version of the RFXlocking code has been used to identify the feedback gains that allow to produce the requested edge radial magnetic field with the lowest possible coil current. In this case, a model-based approach similar to the one used for the mode controller optimization has been adopted, which consists in simulating the mode dynamics scanning several gain values and identifying the gain set, which fulfills the requirements above mentioned.

The $(1, -7)$ mode dynamics has been also simulated when static helical boundary conditions are applied through magnetic feedback. The RFXlocking code suggests, as aspected, that lower current in the active coils is needed to produce a certain radial field at the plasma edge. This is due to the fact that the externally produced magnetic field is not shielded by the wall. Static helical boundary conditions have been tested in the experiment, confirming this evidence, with encouraging results for possible future RFP experiments that may operate with a helical divertor to control the plasma-wall interaction [105].

The effects of the dynamic response of the wall to external magnetic fields used to control these helical equilibria has been investigated by analyzing vacuum field experiments with a rotating $(1, -7)$ coil current perturbation [45]. The analyses reveal that the 3D wall structures tend to perturb the helical symmetry, with the deleterious effect of exciting secondary instabilities that degrade the good confinement typical of helical equilibria. For instance, the presence of the toroidal gap in the RFX-mod wall induces error field harmonics with the same toroidal mode number of the external magnetic field, but with different poloidal mode numbers.

To suppress these error field harmonics, a mode decoupler has been used, which allows to compute the current spatial pattern needed to produce a pure $(1, -7)$ edge radial magnetic field inside the wall. Moreover, other error fields, which are induced by the presence of poloidal gaps in the wall structure, have been detected and a dynamic decoupler scheme, analogous to the one used to compensate the error fields in the current ramp-up phase of the plasma discharge, has been applied to correct them. Vacuum field pulses show that the amplitude of the error fields, both due to the toroidal and the poloidal gaps, are strongly reduced when these decoupling schemes are used, while more tests with plasma are planned for the next experimental campaign. Moreover, thanks to the encouraging results described above, the real-time implementation of the dynamic decoupler scheme in the feedback controller has been proposed. Work is ongoing on this point.

8.1.4. Improved magnetic feedback control with AC compensation in DIII-D

The effects of the dynamic response of the wall to time-varying magnetic fields have been investigated also in the DIII-D tokamak, in the framework of a collaboration between the DIII-D and RFX-mod teams [45].

In standard DIII-D operations, the poloidal magnetic field signals are compensated in real-time for external magnetic fields, such as those produced by field-shaping and feedback (I-C) coil currents, and error fields due to misaligned axi-symmetric coils. Normally, the coupling at zero frequency between each actuator and sensor is taken into account in the feedback logic, neglecting frequency-dependent, or AC effects induced by the eddy-currents in the wall. This scheme is called DC compensation. In this way, the plasma response can be calculated, which is the quantity the feedback reacts to.

The relevance of AC effects has been evaluated first by analyzing plasma experiments, which used the DC compensation in real-time. The analyses suggested that, if such effects are not taken into account in the feedback scheme, a spurious error field is produced by the feedback itself. This error field can further destabilize an unstable RWM in low-β experiments or it can be amplified significantly in high-β plasmas.

A feedback algorithm to compensate these AC effects has been implemented in the power control system and tested in real-time in Ohmic plasmas. Unfortunately no current driven RWM was destabilized in these experiments and thus the AC effects were introduced only by the field-shaping coils. The main outcome of these experiments is that a significantly different value of the $n = 1$ amplitude is obtained when the AC compensation is used with respect to the DC case. More extensive experiments are needed to asses the relevance of AC effects in Ohmic and in high-β plasmas for performance improvement. For these reason, dedicated experiments have been proposed for the 2011 DIII-D experimental campaign.

8.2 Future perspectives

In the following a series of new experiments in RFX-mod and DIII-D, which have been stimulated by the results obtained in this Thesis work, will be described.

8.2.1. Magnetic feedback control using the plasma response in RFX-mod

The best magnetic feedback performance in the DIII-D tokamak has been obtained with schemes that act on the resonant response of the plasma to external magnetic perturbations. This is quite different from what done in RFX-mod, where the quantity that it is zeroed is the total radial magnetic field, given by the sum of

both the plasma response and the magnetic field from external sources (error fields and feedback coils).

To assess the relevance of a feedback scheme that uses the plasma response for RFX-mod, and also to better compare feedback experiments in tokamaks and RFPs, for the next experimental campaign the real-time implementation of a feedback algorithm that acts on the response of the plasma has been proposed. This may be done in RFX-mod by slightly modifying the sideband correction scheme already used in the clean mode control algorithm [32, 68] and described here in Chapter 2. Such modification would simply consist in adding into the range of sidebands to be cleaned also the mode helicity itself.

This new scheme may be applied to tearing modes, but also to error fields. The main harmonics of the error fields in the current ramp-up phase of plasma discharge fall in fact within the unstable RWM spectrum, and thus they are resonantly amplified by these instabilities. Acting on the plasma response, in this case, may have a beneficial effect also on the error field correction, as already shown in tokamaks.

Regarding tearing mode control, the RFXlocking code has been modified to model the mode and feedback dynamics with such a scheme. Figure 8.1 compares the simulated $(1, -7)$ mode dynamics in terms of flat-top averaged normalized edge radial magnetic field amplitude, mode rotation frequency, and coil current amplitude, as a function of the proportional gain, when the edge radial field (in red) and the plasma response (in black) are used as feedback variables. The green curve refers to the latter case with also a derivative gain $K_d = 1$.

The simulations suggest that the $(1, -7)$ normalized edge radial field amplitude, when using the plasma response scheme, increases by about 30%, with respect to the edge radial field case, and consequently the request of coil current. This is highlighted in Figures 8.1(a) and (c). It is interesting to note that the plasma response scheme allows a lower K_p value above which the mode starts to rotate than the other examined case. The reason of this change on the mode dynamics is under discussion.

The increase of the radial field amplitude at the plasma edge and of the coil current amplitude of the $(1, -7)$ mode would not encourage the real-time implementation of the plasma response algorithm. However, a possible way to improve the control exists and consists in using both proportional and derivative gains in the mode controller. As shown by the green curve in Figure 8.1(a), the normalized magnetic field at the edge is significantly reduced, up to 40%, with respect to a purely proportional gain (red curve).

To assess the relevance of algorithms that uses the plasma response for tearing mode control, a possible experiment will consist in setting a proportional gain in the range $K_p = 400 - 500$ and $K_d = 1$ in the $(1, -7)$ mode controller, and compare the $(1, -7)$ mode dynamics for a similar plasma experiment, which uses the edge radial field as feedback variable and the standard $K_p = 800$ is applied in the

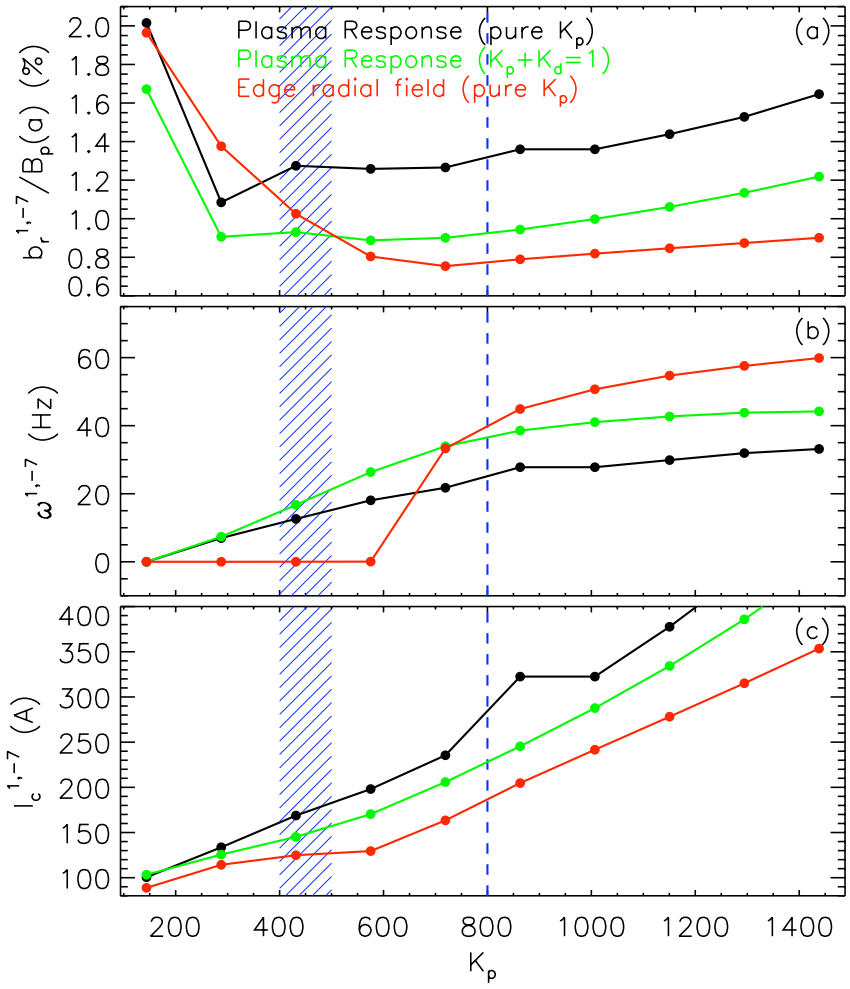

Figure 8.1: (a) Normalized edge radial magnetic field amplitude, (b) mode rotation frequency, (c) coil current amplitude of the $(1, -7)$ mode as a function of the proportional gain. The traces correspond to simulations performed with the RFXlocking code (red) and with the code that uses the plasma response as feedback variable with a purely proportional gain (in black) and with proportional and derivative gains (in green). The dashed blue line represents the K_p value normally used in RFX-mod experiments, while the dashed region corresponds to the range of gains to be applied in the future experiment described the text.

feedback controller. The $K_p = 400 - 500$ and $K_d = 1$ gains have been chosen since they allow a normalized radial magnetic field and mode rotation frequency similar to the ones obtained in standard feedback operation, but saving coil current. In fact, the coil current at $K_p = 800$ is $I_c^{1,-7} = 190A$, while in the proposed experiment is $150A$, with a reduction of about 20%.

8.2.2. Relevance of AC compensation for high-β DIII-D plasmas

Interesting results have been obtained testing in real-time the AC compensation algorithm in Ohmic plasma experiments. Since no current-driven RWM was unstable in these experiments, the importance of AC effects due to feedback coils has not been investigated yet. For this reason, it will be proposed for the next experimental campaign to test the AC compensation in Ohmic plasmas in presence of unstable RWMs.

It would be interesting also to assess the relevance of the AC compensation algorithm on high-β plasmas, since analyses suggest that an improved compensation of the sensor signals, which accounts also for the AC response of the wall, may be useful in conditions where the plasma is less resilient to error fields, such as at high-β and low-plasma rotation.

Another method suitable to study the feasibility of the AC compensation consists in inducing in these plasmas a pre-programmed $n = 1$ magnetic field perturbation produced by the C-coils rotating at frequencies relevant for the AC compensation, and try to compensate it with the I-coils. In this way, it is possible to compare the effects of DC and AC compensation in presence of a known and very reproducible magnetic field source. All these tests have been proposed for the 2011 DIII-D experimental campaign.

Bibliography

[1] Freidberg J.P. 2007 *Plasma Physics and Fusion Energy* Cambridge University press

[2] Goldston R.J. and Rutherford P.H. 1995 *Introduction to plasma physics* London IOP

[3] Miyamoto K. 1989 *Plasma physics for nuclear fusion* Cambridge Mass. MIT press

[4] Hogan W.K. *Inertial fusion state of the art - A collection of overview and technical papers from IFSA2003* 2004 Nuclear Fusion **44**

[5] Lawson J.D. 1957 Proc. Phys. Soc. B **70** 6

[6] Wesson J. 1997 *Tokamaks* Oxford UK Clarendon Press

[7] McGuire K.M. *et al.* 1995 Phys. Plasmas **2** 2176

[8] Ikeda K. *PROGRESS IN THE ITER PHYSICS BASIS* 2007 Nuclear Fusion **47**

[9] Campbell D.J. 2001 Phys. Plasmas **8** 2041

[10] Bickerton R.J. *et al.* 1971 Nature Phys. Sci. **229** 110

[11] Freidberg J.P. 1987 *Ideal Magnetohydrodynamics* New York Plenum Press

[12] G. Bateman 1978 *MHD instabilities* Cambridge Mass. MIT press

[13] Chu M.S. and Okabayashi M. 2010 Plasma Phys. Control. Fusion **52** 123001

[14] Zarnstorff M.C. *et al.* 1988 Phys. Rev. Lett. **60** 1306

[15] Pomphrey N. *et al.* 1992 Princeton Plasma Physics Laboratory Report PPPL-2854 Princeton Plasma Physics Laboratory Princeton NJ

[16] Turnbull A.D. *et al.* 1995 Phys. Rev. Lett. **74** 718

[17] Strait E.J. *et al.* 1995 Phys. Rev. Lett. **74** 2483

[18] Taylor T. *et al.* 1995 Phys. Plasmas **2** 2390

[19] Furth H.P. *et al.* 1963 Phys. Fluids **6** 459

[20] Bodin H.A.B. 1990 Nuclear Fusion **30** 1717

[21] Ortolani S. and Schnack D.D. 1993 *Magnetohydrodynamics of plasma relaxation* Singapore World Scientific

[22] Taylor J.B. 1974 Phys. Rev. Lett. **33** 19

[23] Sonato P. *et al.* 2003 Fusion Eng. Des. **66** 161

[24] Martin P. *et al.* 2009 51^{st} Annual Meeting of the APS Division of Plasma Physics Atlanta GA Bull. Amer. Phys. Soc. **54** 15

[25] Escande D.F. *et al.* 2000 Plasma Phys. Control. Fusion **42** B243-B253

[26] Nordlund P. *et al.* 1994 Phys. Plasmas **1** 4032

[27] Cappello S. *et al.* 1992 Phys. Fluids **B4** 611

[28] Sarff J.S. *et al.* 1997 Phys. Rev. Lett. **78** 62

[29] Martin P. *et al.* 1999 Plasma Phys. Control. Fusion **41** A247

[30] Martin P. *et al.* 2003 Nuclear Fusion **43** 1855

[31] Zuin M. *et al.* 2009 Plasma Phys. Control. Fusion **51** 035012

[32] Marrelli L. *et al.* 2007 Plasma Phys. Control. Fusion **49** B3509

[33] Piovesan P. *et al.* 2009 Nuclear Fusion **49** 085036

[34] Luxon J.L. 2002 Nuclear Fusion **42** 614

[35] Luxon J.L. *et al.* 2003 Nuclear Fusion **43** 1813

[36] Kikuchi M. *et al.* 1990 Nuclear Fusion **30** 343

[37] Gormezano C. *et al.* 2007 Nuclear Fusion **47** S285

[38] White R.B. *et al.* 1984 Phys. Fluids **27** 2455

[39] Gobbin M. *et al.* 2007 Phys. Plasmas **14** 072305

[40] Lorenzini R. *et al.* 2009 Nature Phys. **5** 570

[41] Escande D.F. *et al.* 2000 Phys. Rev. Lett. **85** 3169

[42] Piron L. *et al.* 2010 Nuclear Fusion **50** 115011

[43] Piron L. *et al. Dynamic decoupling and multi-mode magnetic feedback for error field correction in RFX-mod* submitted to Nuclear Fusion

[44] Piovesan P. *et al. Role of external 3D magnetic fields and flow in helical RFX-mod equilibria* submitted to Plasma Phys. Control. Fusion

[45] Piron L. *et al. Improved dynamic response of magnetic feedback in RFX-mod and DIII-D* submitted to Plasma Phys. Control. Fusion

[46] Taylor T.S. *et al.* 1995 Phys. Plasmas **2** 2890

[47] Garofalo A.M. *et al.* 2002 Phys. Plasmas **9** 1997

[48] Sabbagh S.A. *et al.* 2006 Nuclear Fusion **46** 635

[49] Takeji S. *et al.* 2002 Nuclear Fusion **42** 5

[50] Hender T.C. *et al.* 2004 Proc. 20^{th} Int. Conf. on Fusion Energy Vilamoura Portugal EX/P2-22

[51] Cates C. *et al.* 2000 Phys. Plasmas **7** 3133

[52] Garofalo A.M. *et al.* 2001 Nuclear Fusion **41** 1171

[53] Okabayashi M. *et al.* 2001 Phys. Plasmas **8** 2071

[54] Sabbagh S.A. *et al.* 2006 Phys. Rev. Lett. **97** 045004

[55] Strait E.J. *et al.* 2004 Phys. Plasmas **11** 2505

[56] Okabayashi M. *et al.* 2009 Nuclear Fusion **49** 125003

[57] A. Bondeson *et al.* 1994 Phys. Rev. Lett. **72** 2709

[58] Strait E.J. *et al.* 1999 Nuclear Fusion **39** 11

[59] Strait E.J. *et al.* 1995 Phys. Rev. Lett. **74** 2483

[60] Garofalo A.M. *et al.* 1999 Phys. Rev. Lett. **82** 3811

[61] La Haye R.J. *et al.* 2004 Nuclear Fusion **44** 1197

[62] Reimerdes H. *et al.* 2005 Nuclear Fusion **45** 368

[63] Strait E.J. *et al.* 2007 Phys. Plasmas **14** 056101

[64] Takechi M. *et al.* 2007 Phys. Rev. Lett. **98** 055002

[65] Liu Y. *et al.* 2005 Nuclear Fusion **45** 1131

[66] Piron L. *et al.* 2010 52^{st} Annual Meeting of the APS Division of Plasma Physics Chicago IL. UP9.00064

[67] Bishop C.M. *et al.* 1993 Plasma Phys. Control. Fusion **31** 1179

[68] Zanca P. *et al.* 2007 Nuclear Fusion **47** 1425

[69] Paccagnella R. *et al.* 2006 Phys. Rev. Lett. **97** 075001

[70] Brunsell P.H. *et al.* 2004 Phys. Rev. Lett. **93** 225001

[71] Zanca P. *et al.* 2004 Plasma Phys. Control. Fusion **46** 1115

[72] Alfier A. *et al.* 2008 Plasma Phys. Control. Fusion **50** 035013

[73] Innocente P. *et al.* 2009 Nuclear Fusion **49** 115022

[74] Carraro L. *et al.* 2006 33^{rd} EPS Conf. on Plasma Physics Rome Italy 2006 P5.083

[75] Greene P. *et al.* 1993 Phys. Fluids B **5** 550

[76] Evans T.E. *et al.* 2006 Nature Phys. **2** 419

[77] Garofalo A.M. *et al.* 2001 Nuclear Fusion **41** 1171

[78] Strait E.J. *et al.* 2003 Nuclear Fusion **43** 430

[79] Bondeson A. *et al.* 1994 Phys. Rev. Lett. **72** 2709

[80] Ward D.J. *et al.* 1995 Phys. Plasmas **2** 1570

[81] Bialek J. *et al.* 2001 Phys. Plasmas **8** 2170

[82] Okabayashi M. *et al.* 1988 Nuclear Fusion **38** 1607

[83] Strait E.J. *et al.* 2009 Nuclear Fusion **49** 104008

[84] Zanca P. 2009 Plasma Phys. Control. Fusion **51** 015006

[85] Gimblett C.G. 1986 Nuclear Fusion **51** 617

[86] Villone F. *et al.* 2008 Phys. Rev. Lett. **100** 255005

[87] Strumberger E. *et al.* 2008 Phys. Plasmas **15** 056110

[88] Bialek J. *et al.* 2001 Phys. Plasmas **8** 2170

[89] Albanese R. *et al.* 2008 IEEE Trans. Magn. **44** 1654

[90] Portone A. *et al.* 2008 Plasma Phys. Control. Fusion **50** 085004

[91] Soppelsa A. *et al.* 2009 Fusion Eng. Des. **84** 1784

[92] Gregoratto D. *et al.* 2005 Phys. Plasmas **12** 092510

[93] Garofalo A. *et al.* 2002 Phys. Rev. Lett. **89** 235001

[94] Menard J.E. *et al.* Nuclear Fusion **50** 045008

[95] Marchiori G. *et al.* 2007 Fusion Eng. Des. **82** 1015

[96] www.mathworks.com

[97] Soppelsa A. 2008 *Aspects of Electromagnetic Modelling for Multiple-Input-Multiple-Output Control of MHD Modes in RFX-mod* Ph.D. Thesis

[98] Soppelsa A. *et al.* 2008 Fusion Eng. Des. **83** 224

[99] Åström K. and Hägglund T. 1995 *PID controllers: theory design and tuning* Instrument Society of America

[100] Fitzpatrick R. 1999 Phys. Plasmas **6** 1168

[101] Yagi Y. *et al.* 1999 Phys. Plasmas **6** 3824

[102] Zanca P. *et al.* 2001 Phys. Plasmas **8** 516

[103] Escande D.F. *et al.* 2009 51^{st} Annual Meeting of the APS Division of Plasma Physics Atlanta Georgia. TP8.78

[104] Bonfiglio D. *et al. Necessary criterion for magnetic field reversal in the reversed-field-pinch* submitted to Nuclear Fusion

[105] Martines E. *et al.* 2010 Nuclear Fusion **50** 03501

[106] Bonomo D. *et al.* 2010 *Flow measurements and modeling in helical RFX-mod equilibria* submitted to Nuclear Fusion

[107] In Y. *et al.* 2008 Phys. Plasmas **15** 102506

[108] Zanca P. *et al.* 2007 Journal of Nuclear Materials **363-365** 733-737

[109] In Y. *et al.* 2010 Nuclear Fusion **50** 042001

Acknowledgements

It is a pleasure to thank the many people who made this Thesis possible.

It is difficult to overstate my gratitude to my Supervisor, Prof. Piero Martin, and to my Tutors Dr. Lionello Marrelli and Dr. Paolo Piovesan. They constantly gave me the important guidelines and precious suggestions for my research work. They quickly became for me the role model of a successful researcher in plasma field.

I thank Dr. Paolo Zanca for help with the RFXlocking code which was the starting point of my research and for his friendly support during all this time. I am thankful to Dr. Anton Soppelsa and Dr. Giuseppe Marchiori for interesting discussions on active control systems.

I am profoundly grateful to the Consorzio RFX, where most of this Thesis was made, and in particular to my Supervisor Prof. Piero Martin and my group-leader Lionello Marrelli, for having given me the possibility of working in a very stimulating group and of doing a part of my research work in collaboration with the DIII-D group.
It has been a very formative experience to visit the DIII-D experiment, where I found an extraordinary scientific and human environment. I thank the whole RWM group, and in particular Dr. Michio Okabayashi, Dr. Yongkyoon In, Dr. Holger Reimerdes, Dr. Ted Strait, Dr. Jeremy Hanson and Dr. Matt Lanctot.
I thank very much Ikuko and Teruo Tamano for the human support during my stay in San Diego, you made me feel at home.

I also would like to thank my lab mates Federica, Fulvio, Matteo, Michela and Marco for providing a stimulating and fun environment in which to learn and grow.

I wish to thank my long-term friends Anna, Stefania, Francesco M., Francesco Z., Marzi, Alessandro, Valeria, Jacopo, Leonardo, Elisa, and Cristiano for helping me get through the difficult times, and for all the emotional support, comraderie, entertainment, and caring they provided.

Acknowledgements

I am eternally grateful to Matteo for his constant love and strength throughout the years. Without him, and his ability to raise my spirits when I was most discouraged, I could never made it this far. Matteo, you were the wind beneath my wing.
I am also thankful for my sister, Chiara for Latex and computer support, Apu and Celeste for the carefree moments spent together.

Lastly, and most importantly, I wish to thank my parents, Luigina Morosin and Dino Piron, my uncle Adolfo for the moral support and my aunt Gemma and my uncle Piero for being my second family.

A Time for Everything
Qohèlet 3,1-8

There is an appointed time for everything.
And there is a time for every event under heaven.
A time to give birth, and a time to die;
A time to plant, and a time to uproot what is planted.
A time to kill, and a time to heal;
A time to tear down, and a time to build up.
A time to weep, and a time to laugh;
A time to mourn, and a time to dance.
A time to throw stones, and a time to gather stones;
A time to embrace and a time to shun embracing.
A time to search, and a time to give up as lost;
A time to keep, and a time to throw away.
A time to tear apart, and a time to sew together;
A time to be silent, and a time to speak.
A time to love, and a time to hate;
A time for war, and a time for peace.

And now it's time for me to finish my Ph.D Thesis, by the grace of God!

Lidia Piron